CRANFIELD UNIVERSITY

FANGMING HENG

EXPERIMENTAL AND NUMERICAL MODELING OF HIGH SPEED ICE IMPACT ONTO RIGID TARGET

SCHOOL OF AEROSPACE, TRANSPORT AND MANUFACTURING
Applied Mechanics

Master degree by research
Academic Year: 2014 - 2015

Supervisor: Dr. James Campbell
03/2015

CRANFIELD UNIVERSITY

SCHOOL OF AEROSPACE, TRANSPORT AND MANUFACTURING
Applied Mechanics

Master degree by research

Academic Year 2014 - 2015

FANGMING HENG

EXPERIMENTAL AND NUMERICAL MODELING OF HIGH SPEED ICE IMPACT ONTO RIGID TARGET

Supervisor: Dr. James Campbell
03/2015

ABSTRACT

The core goal of this research is to develop an ice impact modelling methodology for ice impact on aircraft structures. The main current limitation of ice impact analysis is the ice constitutive model, so this research is focussed on the assessment and improvement of current ice constitutive models. Centre on this aim three aspect works has been done. First, investigating the ice mechanical properties. Through literature review 8 properties of ice have been identified as crucial properties of ice when modelling ice or assessing the ice material model. Secondly, assessing the current material models theoretically and numerically and identify areas where improvements can be made to current ice constitutive models. Five existing ice material models are investigated through theoretical study. Two of them, MAT 13 and MAT 155, are available to use in the LS-Dyna and have been tested through modelling 3 different test problems. Through the investigation of the ice model, MAT 155 is proved to be the optimum ice material model as it reflects the most features (including the compaction feature, bilinear hardening, pressure based failure mode, strain rate dependence) of ice. Through the research of MAT 155, three modified methods of MAT 155 are proposed. Thirdly, developing an implementation of an ice constitutive model as a tool for future assessment of improvements to ice modelling. An LS-Dyna user defined material model (UMAT) based on MAT 155 has been built up and modified by adding the pressure dependence feature. Through the building up and verification of UMAT, two features of MAT 155 were found to perform differently than was described in Carney's article. The Drucker Prager-yield function was chosen to reflect the pressure dependence of the ice and the routine describing the Drucker-Prager yield function has been proved that it can work properly in the simulation. Based on the investigated ice material model, the pressure dependent feature is added into this user defined material model.

Keywords:

LS-Dyna, UMAT, pressure dependent yield criteria, MAT 155, ice model assessment.

ACKNOWLEDGEMENTS

The author would like first to warmly thank her supervisor, Dr. James Campbell, for his patience, his availability and his advice throughout the research. Then the author would like to thank Dr. Kevin Hughes for letting her have this chance to study in Canfield University.

The author would also like to thank all the PHD students in the Applied Mechanics Department, who give me a lot of support during my one year study. Special thanks go to Daniel Portelli and Lewis Kiely who helped me with the mathematics and Fortran programming of the constitutive model, and to Marina Seidl who helped me with the numerical modelling.

Finally, I would like to thank my parents who have constantly supported my studies.

TABLE OF CONTENTS

LIST OF FIGURES

LIST OF TABLES

1 INTRODUCTION

1.1 Background

Hail threat has always been considered as the greatest thunderstorm hazard to aircraft which can be dated back to as early as the 1950s [1]. However, before 1995, most of the research on the ice impact on the aircraft focused on the integrity of the aircraft structures after the impact and there were almost no experimental records on the ice itself during the impact or the records of distribution and track of the crashed ice particles after the impact [2].

Kim modelled the sphere ice impact test problem by using commercial software – DYNA 3D in 2000[3]. There are many reasons for the late start of ice impact numerical simulation, including insufficient computer power, the complicated property of ice which suffers an extreme deformation within the impact process. The only available commercial code ice material model to use was developed by Carney in 2006[4], but in his article Carney concluded that “No attempt has been made to include micromechanical or first principles models of combination of ice or its response after impact. More sophisticated models could and should be developed”.

With the increasing use of composite materials in aircraft the hail impact event has become more and more serious. EASA established a research project in 2008 and published a hail threat standardisation report in 2009[5] which was revised in 2010. This report set a foundation for the development of a hail threat standard through a review of the mass of meteorological and aviation information. As more and more attention is paid to the hail threat, there is a strong need for a more accurate constitutive model of ice under high speed impact conditions to determine the damage limit of the composite structures.

1.2 Aim and objectives

The core goal of this research is to develop an ice impact modelling methodology for ice impact on aircraft structures. The main current limitation of ice impact analysis is the ice constitutive model, so this project is focussed on the

assessment and improvement of current ice constitutive models. The objectives of the research are:

- To investigate the ice mechanical properties then assess the current material models theoretically and numerically.
- To identify areas where improvements can be made to current ice constitutive models.
- To develop an implementation of an ice constitutive model as a tool for future assessment of improvements to ice modelling.

1.3 Methodology

The foundation of this research is to understand the ice mechanical properties, to investigate the main features of the ice. Based on the main features of the ice the existing ice material models can be assessed. According to the assessment, the modification of the current ice material model can be conducted.

To investigate the improvement to the current ice constitutive model, the assessment of the existing material model which has been used in ice simulation was conducted through two approaches - theoretical investigation and simulated investigation.

In the theoretical investigation, five material models are investigated - MAT 10 [9], MAT 13 [9], Carney's model [4](MAT 155 [9]), Jeffery Abaqus model [15] and the Pernas-Sánchez model [8]. The assessment of these 5 material models is through comparing the features reflected by the model to the typical features of the real ice.

In the numerical investigation, two material models which are available to use in LS-Dyna and which have been used in ice impact simulation before are investigated by modelling three typical ice impact experiment problems. The evaluation criterion in this approach is the similarity between the numerical modelling result and the experiment test data. The first experiment problem is the pressure recording test conducted in Nanjing. It is chosen because previously most of the test data recorded in the ice impact experiment is the total impact force, but in this experiment the data recorded is the contact pressure. The

second test problem is the Kim sphere test [3] because it is widely used nowadays. Many academics such as Truchelut [6] used this model to validate the ice material model. The last one is the Pereira cylinder ice test [4;7] because this experiment allows for a different loading condition.

Based on the assessment of the current ice material model the modification of the ice material model is proposed. The basic theory is using the LS-Dyna UMAT routine to model Carney's ice model which is the only material model developed for ice in LS-Dyna, and then change the Von-Mises yield criteria to the pressure dependent yield criteria. Thus a modified ice material model has been developed as a basis for future research.

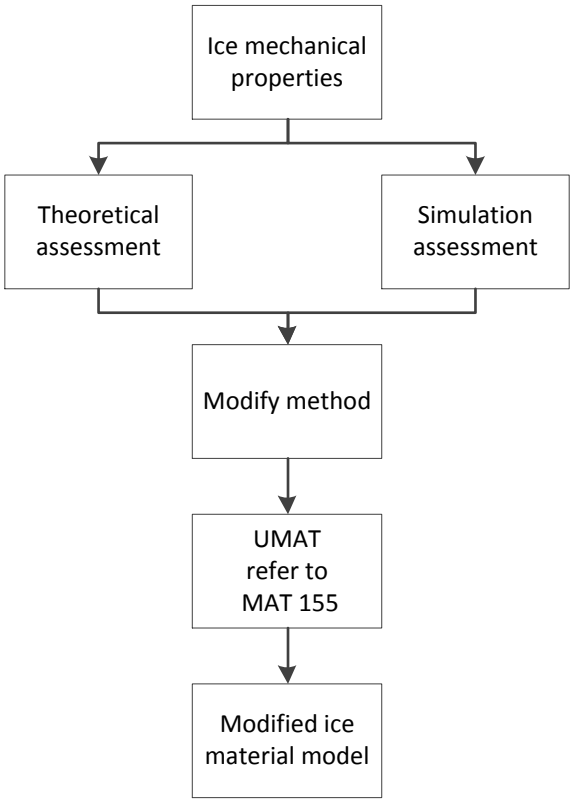

Figure 1-1 Research approach

2 Literature review

Only a very few efforts have been made to model ice numerically at high strain rates [3]. This is mainly because of that ice is not a commercial structural material, and aside from high velocity impact situations of interest to aerospace industry, is rarely subject to high strain rate impact conditions.

Currently, the main methods of researching high velocity ice impact are experimental research, numerical simulation research and constitutive model research.

The experimental research started relatively early. As early as the 1950s, Souter et al. [1] had already done some research work on discussing the influence of hailstones impacting on the aircraft. However, before 1995, most of the research on hailstones impacting the aircraft structures is just focused on the integrity of the aircraft structure after the impact but there were almost no experimental records on either the body of the hailstone itself during the impact or records of distribution and track of the smashed hailstone particles after the impact. In 1995, Render [2] used Pattemator and high-speed photography to conduct the experiment of high speed ice impacting on a plate. The probability statistics method was taken to research the physical characteristics of the ice impact. He discovered that the distribution of the fractures of the ice is greatly determined by the angle between the incidence of the ice and the target plate and is slightly influenced by the impacting speed and the target plate temperature. At some level, Render's research work indicated the future direction of research of the ice impacting on the aircraft's structure [2].

The simulation of the mechanical behaviour of the ice under high-speed impact started relatively recently [3]. Due to the complexity of the materials and the diversity of real situations, the experiment is very expensive and cannot be conducted or analysed in time. So the finite element analysis became the necessary method to approve the ability of anti-dropping foreign objective damage [4]. In 2000, Kim et al. [3] used a metallic material model to simulate an

ice impact experiment in DYNA3D. Recently, the simulation of ice started to be more diverse such as the simulation software of LS-Dyna, Abaqus and the simulation method started to be as more diverse in terms of development of FE method Arbitrary Lagrange-Euler method and SPH method.

The research on the constitutive model of ice under high strain rate condition is very scarce [8]. There is only one material model which is specifically developed for ice material available to use in LS-Dyna [9]. But to the establishment of the constitutive model of ice under high-speed impact is very important to explain the mechanical behaviour of ice under high-speed impact.

2.1 Review of the experimental method

According to the ice projectile structure, the ice impact experiments can be classified as layered ice projectile tests, multi-crystal ice projectile tests and single-crystal ice projectile tests. According to the experiments device, the ice impact experiments can be classified as split Hopkinson pressure bar (SHPB) tests, rigid target tests, and deformable target tests. Throughout all of the ice impacting experiments, using the gas cannon to accelerate the ice projectile is regarded as the most popular experimental method.

SHPB experiments use the SHPB device to test the mechanical characteristics of the ice itself, such as compression strength. Kim [10], Shazly et al. [11; 12] all used the SHPB device to investigate the effect of the strain rate on the compressive strength of ice.

The rigid target experiments are widely used to investigate the influence of the impact energy [3], the structure of ice projectile [7] and the shape of the ice projectile. High-speed photography is always used to observe the dynamic behaviours of the ice within the impact process, such as the expansion of the flaws and the complete process of the failure of the whole ice sample[13;14].

In 2000, Kim [3] conducted the rigid target experiments on the sphere ice projectile with different diameters - 25.4mm, 42.7mm, and 50.8mm. He also used 11000 FPS high-speed photography to observe the dynamic behaviour of ice during the impact process. He found that under 73.5m/s, the 42.7mm diameter

ice projectile started to produce local cracks at the moment of the ice projectile sample contacting the target plate and the cracks would spread along the directions away from the local failure. Comparison of the records of high-speed photography and the dynamic impact force it was found that the impact force would reach peak value in the early stage of the impact process.

In 2006 Pereira [7] conducted rigid target experiments with single-crystal ice projectile and multi-crystal ice projectile at the speed around 100-200m/s. it has been found that when the failure happens, the ability of affording the deviatoric stress of the ice drops dramatically or even disappears and at the same time, the ice tends to behave like fluid.

In 2013, Jeffery [15] conducted rigid target experiments and found that the experimental data has great scatter, which implies that ice has a very typical brittle feature whose strength has a very wide range [15]. He also found the peak force is mainly decided by the kinetic energy rather than the size of the ice projectile [15].

The deformable target experiments are usually used to observe the mechanical behaviours of the target under the high-speed ice impact [16-21]. The experiments aiming at finding the mechanical responses of the target are the necessary methods to research the resistance of the aircraft structures and materials after ice impact.

The deformable target experiments are mainly used to investigate the critical impact energy that cause the damage to the targets, the failure mode of the target and the response of the target during the impact process. In order to investigate the response of the composite panel under ice impact S. Heimbs[18] , Abe Askari [17] conducted deformable target experiments. In 2000, Kim[3] conducted deformable target experiments on two composite materials, AS4/8552 and AS4/977, and discovered that the initial failure mode of the laminated plate composite material is delamination as observing that when the impacting energy is slightly higher than the critical impact energy, the delamination would happen. He also found that the value of the critical impact energy is relevant to the thickness of the target plate and the size of the hailstone. In 2012, Jennife[22]

conducted deformable target experiments on Toray T800/3900-2. He also found that the value of the critical impact energy is proportional to the thickness of the plate.

2.2 Review of the numerical simulation method

Composite material has a mass application in modern aircraft, but some important indexes of the composite materials such as critical damage value, initial damage formation and development information are difficult to acquire by the methods other than numerical simulation. So it is necessary to build the ice material model precisely.

In 2000, Kim and Kedward [3] used MAT 13 to simulate the Kim sphere ice impact experiment. It is a non-iterative plasticity with simple plastic strain failure model. This material model was chosen because when the pressure reaches the failure pressure, the element loses its ability to carry tension and the deviatoric stress is set to zero which is similar to the failure behaviour of ice. But the most important feature of ice-strain rate dependence has not been considered. Figure 2-1 shows the comparison between the DYNA3D simulation results and test data. From the figure, it can be found that the time distribution of the force and the shape of the curve were almost the same, but the peak value of the force had a large difference.

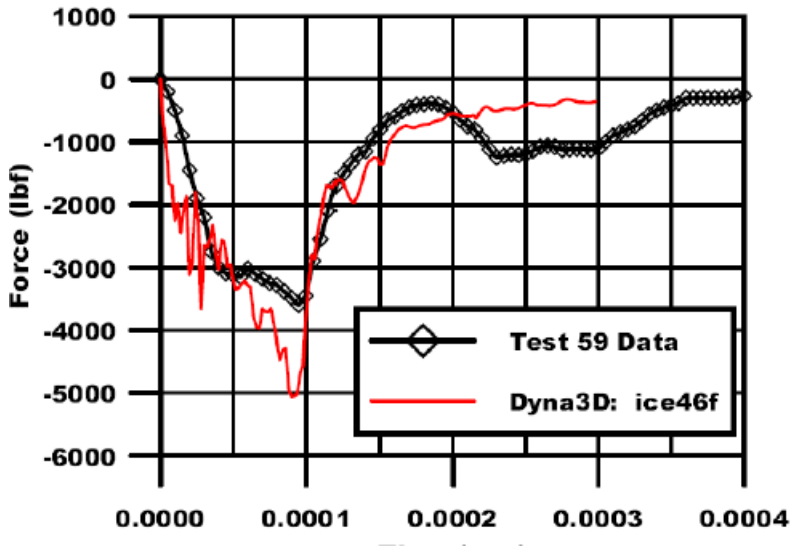

Figure 2-1 Kim MAT 13 numerical model result [3]

In 2004, Keune [24] optimized the model used by Kim and Kedward and used the same elastic-plastic materials with failure model in LS-DYNA. A relationship was developed which can allow the analyst to select the appropriate values depending on the size and the velocity of the projectile. The shapes and peak force are closer to the experiment data but there were some deviations on the time distribution.

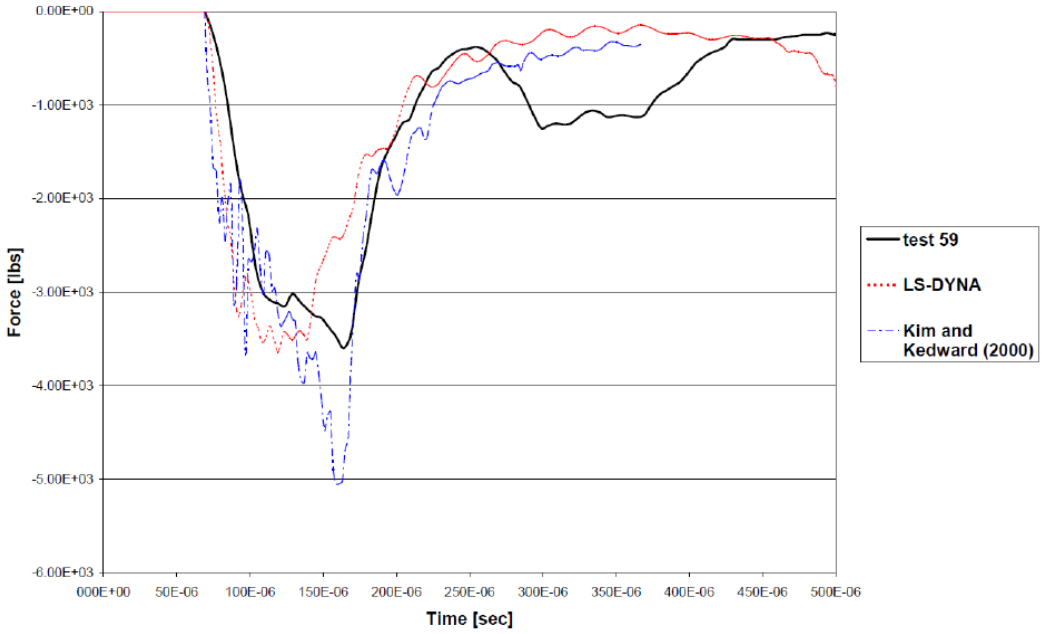

Figure 2-2 Keune LS-Dyna numerical model [24]

In 2006, Park [23] developed a similar ABAQUS model according to Keune's [24]. The same variable parameters, such as yield strength and failure tensile stress were used. The volume viscosity was added in to this ice model. The comparison between the simulation result and test data are shown in Figure 2-3. Similar to Kuene's model, his model also needs some manual parameter selection work to realize good uniformity characteristics and is suitable for a wider range of sizes and speed of the ice projectile.

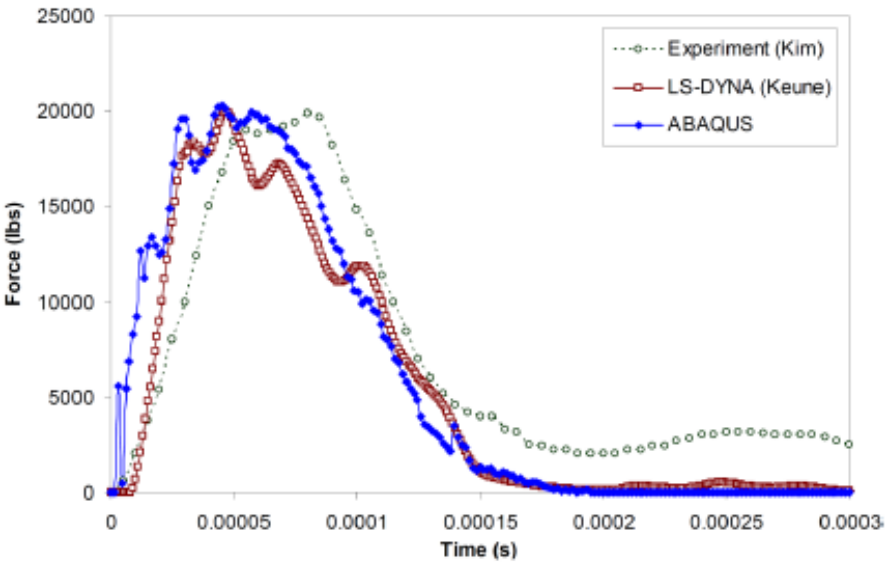

Figure 2-3 Park Abaqus numerical model result [23]

In the same year, Carney [4] developed the only ice material model available to use in LS-Dyna. In his model, three important features of ice were added – strain rate dependence; different performance in tension and compression and nonlinear bulk response. Figure 2-3 shows the similarity between the simulation results and test data. From the figure, the pulses of both initial forces matched well.

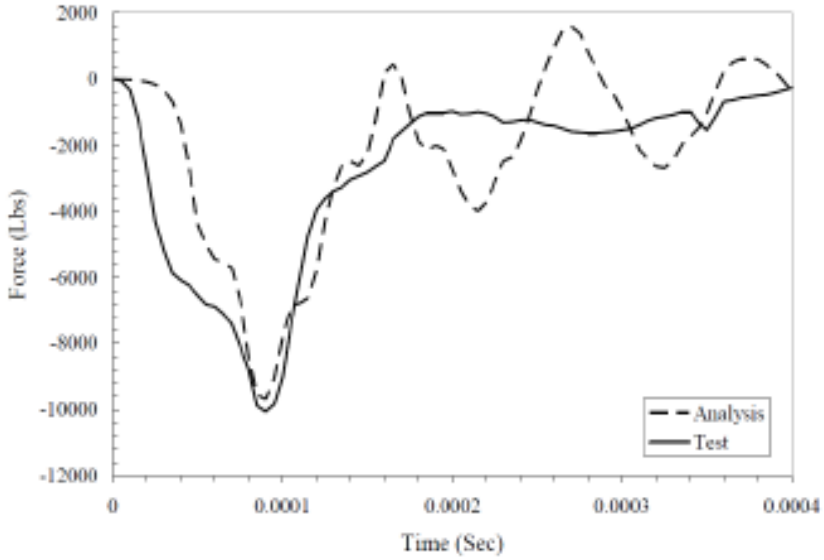

Figure 2-4 Carney MAT 155 LS-Dyna numerical model result [4]

Marco[25] using MAT 10 modelled a deformable target test in LS-Dyna and compared three different mesh method on hail models - FE, ALE and SPH. It was concluded that the FE method was only feasible in the early stages of the impact because after that the FE mesh would undergo large distortions. However, the ALE method provides an accurate description in the later stages of the impact in which the cracked hailstone behaves like fluid. SPH performed the best among these three methods, which behaves visually in a way closer to common experience.

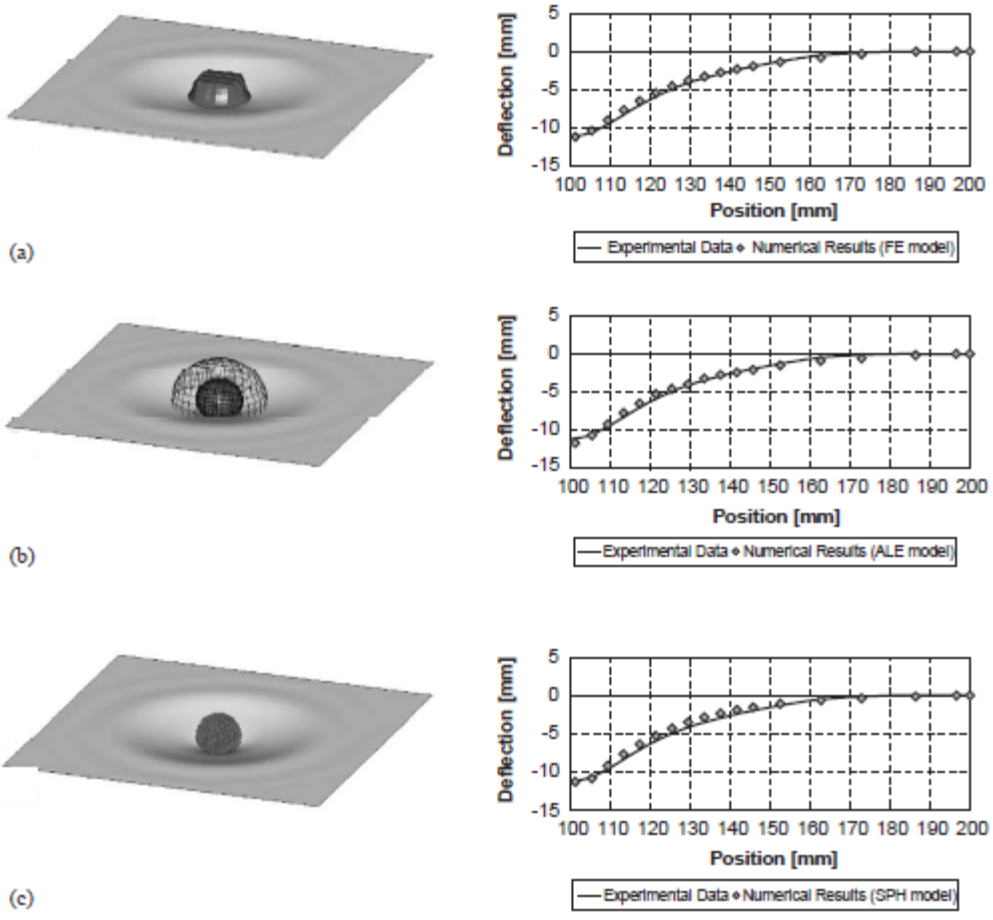

Figure 2-5 Marco MAT 10 LS-Dyna numerical model result [25]

The meshless method, including the SPH method, has an obvious advantage when there is a big gridding distortion or gridding movement. So the meshless method is an effective method to solve the high-speed ice impact event.[25]

2.3 Review of the constitutive model

Literature describing constitutive equations for the simulation of ice impact is likewise scarce [8]. MAT 13 is the simplest one [8] available in LS-Dyna, and has been used by Kim [3], Keune [24] and Park [23]. This material model is a metallic material model, but it can reflect part of the ice behaviour which can behave like a fluid which only can carry hydrostatic pressure after failure. MAT 10 is another metallic material model that also can reflect some of the ice properties, and has been tested by Marco [25]. The advantage of this material is that an Equation of State is contained in this material model which provided this material a non-linear relationship between the pressure and volume besides the same post-failure behaviour. The EOS is needed because under impact condition the pressure plays a very important role.

The first constitutive equation specifically developed for ice deforming at high strain rates was that of Carney et al.[4]. Additional to the post-failure behaviour and the EOS, the strain rate dependence and the different behaviour in tension and compression are also composed in Carney's model. But as a brittle material, the yield stress is also being influenced by the current pressure [8], this feature was not being composed by Carney's model. In 2012, another ice constitutive model was developed by J. Pernas-Sánchez [8] which was implemented in the commercial code LS-Dyna. In his material model, the pressure dependence feature was reflected by the Drucker-Prager yield function. Based on his description and his verification the different performance of ice under tension and compression also can be reflected by the yield equation. But the effective cohesion of the material in the Drucker-Prager yield function which ought to be equivalent to the current yield stress [26] was defined as a constant value related to the different yield stress in tension and compression.

2.4 Review of the simulating method

Three numerical methods can be used currently. They are Lagrangian FE method, ALE method and SPH method.

2.4.1 FE method

The Lagrangian FE method is a typical numerical method for continuum mechanics, especially for the impact events, and it is very efficient for solving nonlinear problem. But when facing large deformation problems which are very typical for fluid-like material this method will experience a large mesh distortion [25]. Through the test done by Marco [25], this method was found to be only suitable for the early stages of the impact, and when the ice projectile comes to the third stage, as discussed in Chapter 3.2, the material will undergo large distortions, at that time the accuracy of the simulation will become unacceptable, and it required more CPU time. So this simulation method has not been adopted in this research.

2.4.2 ALE method

In the ALE approach the model of ice projectile not only includes ice, but also needs to describe a small surrounding region, which can avoid the outflow of the ice material out of the Eulerian mesh. It was found that ALE model can only describe the fluid-like stage accurately [25]. So this kind of simulation method also has not been adopted in this research.

2.4.3 SPH method

The SPH method is a meshless Lagrangian method. A set of endowing mass particles replaced the traditional mesh. The connection between different particles was described by kernel function. The SPH model was proved to be the closest way to model the ice projectile behaviour by the comparison study from Marco [25]. So the SPH method was selected as the simulation method in this research.

2.5 Conclusion

Currently, the mechanical response problem of high-speed ice impact has not been explained very well, especially in the aspect of building the constitutive models; on the other hand the hail storm is an unavoidable accident to the aircraft,

and it is necessary to design hail-proof and high-efficiency aircraft structures. So there is much more work to be done in the future.

3 Ice impact mechanical properties

3.1 Ice mechanical properties

Ice properties are very dependent on several conditions, such as loading rate, temperature. This section only briefly summarizes the ice properties of interest to the current work, omitting some other effects, for instance, constrain condition, salinity, etc. Thus the ice discussed there is under high strain rate impact without constraint.

Brittle failure is the dominant failure mode of ice both in tension and compression. Under tension loading, ice generally exhibits little tensile ductility [27]. Under compression loading ice will exhibit ductile behaviour under lower rate of deformation, and exhibits brittle behaviour under higher deformation rates around $10^{-4}-10^{-3}\mathrm{s}^{-1}$[27; 28]. This trend is shown in Figure 3-1.

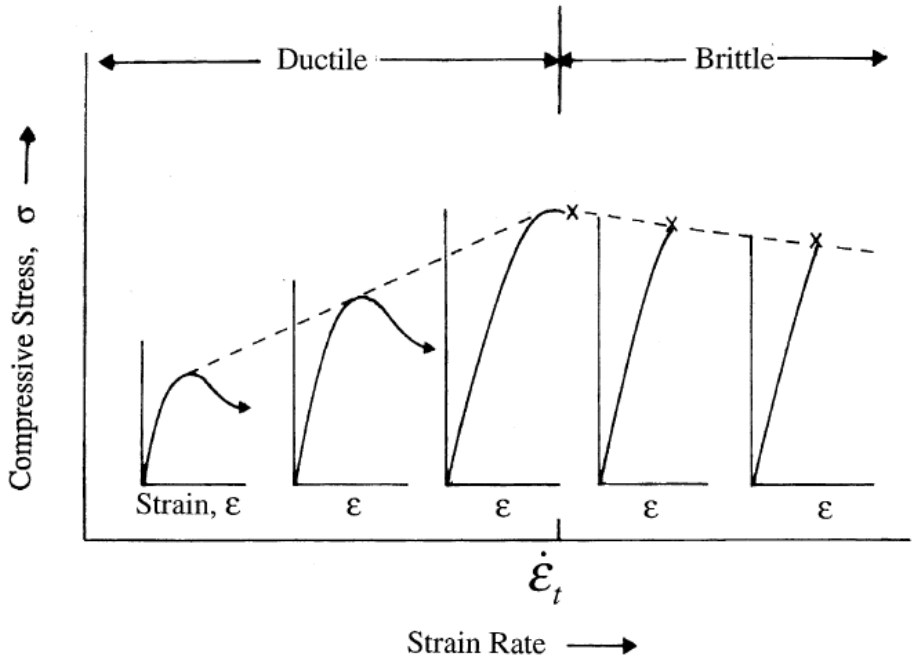

Figure 3-1 Strain rate sensitive phenomena [27]

The difference is not only reflected in the failure mode but also reflected in the factor influencing the yield strength [27].

The failure of ice is typically transgranular cleavage under tension loading. The tensile strength of ice is essentially independent of strain rate whereas it is greatly affected by the grain size. Like alumina and other ceramics, the tensile strength of ice increases with refining reduction in grain size, and exhibiting both Petch-type (Equation 3-1) and Orowan-type (Equation 3-2) relationships with grain size, but in an opposite way[27].

$$\sigma_t = \sigma_0 + k_t d^{-0.5} \ (for\ d\ >\ d_c) \qquad \textbf{Equation 3-1}$$

or

$$\sigma_t = K d^{-0.5} (for\ d\ <\ d_c) \qquad \textbf{Equation 3-2}$$

Where σ_0, k_t, K are material constants, while d_c as the critical grain size needs to be noticed. The tensile failure can be explained by either the nucleation or the propagation of cracks. When grain size d is larger than d_c, ice shows Petch behaviour and the stress to nucleate a crack is much greater than the stress to propagate it, consequently crack nucleation limits the strength. When grain size d is smaller than d_c, ice shows Orowan behaviour in which propagation governs the strength.

Compared with tensile behaviour, compressive behaviour is more complicated. Since the yield strength will be influenced by the strain rate under compressive loading, the strain rate needs to be taken into consideration. When the impact velocity is greater than 30m/s, the strain rate will be above $10^{-1}s^{-1}$ [4]. This is typical for hail impact on aerospace structures. So this chapter only focuses on a relatively higher strain rate condition. At this strain rate, the ice would perform like brittle material [27]

The yield stress under compression is a function of temperature, strain rate, grain size. It will decrease with increasing temperature, increasing strain rate and increasing grain size [27].

End constraint can influence the failure type of ice. When loaded uniaxial, the failure would occur after the inelastic strains $\lesssim 0.003$ via longitudinal splitting [27]. When loaded biaxially, they would be strengthened by increasing confining under

lower confinements condition; they would be weakened by increasing confining stress under higher confinements [27] and the failure would occur by cleavage in and then spalling out of the loading plane. When loaded triaxial, the failure would occur by shear faulting and inclined principal stress at about 45°, which is very different with other brittle material, due to the localized plasticity that leads to unstable in-plane crack propagation.

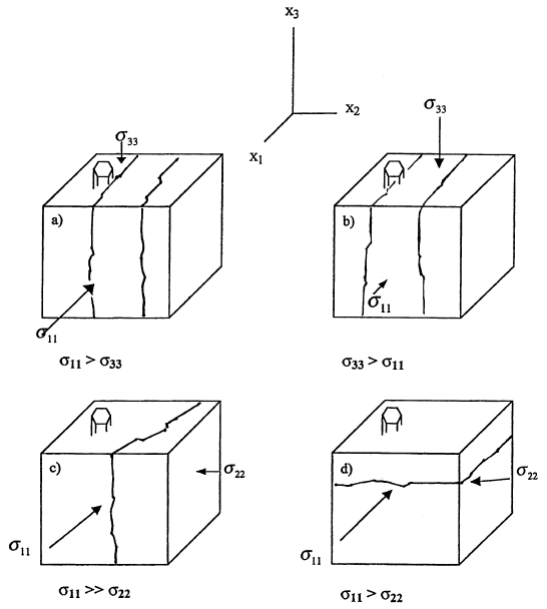

Figure 3-2 Biaxial loading failure mode [27]

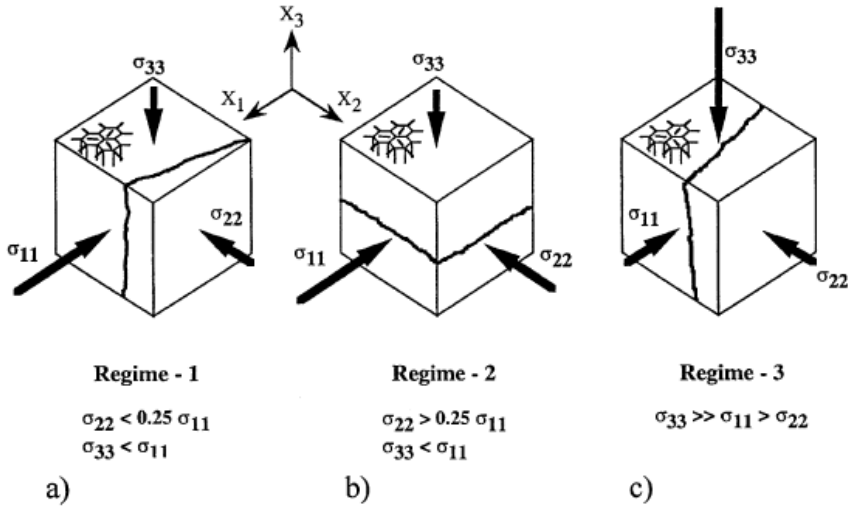

Figure 3-3 Three axial load failure mode [27]

The compressive strength depends on the hydrostatic component of the applied stress. In this case, the crack mechanics and frictional sliding would decide the brittle failure [27]. Coulomb's criterion is suggested as the appropriate failure criteria [27] when dealing with the ice impact issue which can be represented as Equation 3-3

$$|\tau| = S_0 + \mu\sigma \qquad \text{Equation 3-3}$$

In this equation$|\tau|$ is the shear stress acting across the future fault plane which is resisted by material cohesion, denoted S_0 and by friction, denoted by the production of the coefficient of internal friction, μ and the normal stress across the plane, σ. μ is related to the temperature [27] which gives an answer to the temperature dependence of the yield strength. The strain-rate softening phenomena can be explained by the friction coefficient which would decrease with increasing sliding velocity [29].

Failure of ice was captured by high-speed photography [28; 30], as is shown in Figure 3-4. It shows that the failure of ice is not a sudden failure, but a multistep process [31]. It is needed to be noticed that even the cracks generated in ice, the ice does not collapse until a kind of percolation threshold is reached, and the percolation threshold stress is regarded as the failure stress [28]. Cracks would first form once the applied stress reaches about 0.2 to 0.33 of the failure stress. The size of the cracks is similar to the grains and the cracks will nucleate on grain boundaries inclined by about 45° to the loading direction [28]. As the load rises, the cracks would grow in number density (number of cracks per unit volum) and distribute more or less uniformly throughout the matrix. As the localized tensile stresses increase, the wing cracks would appear out-of-plane extensions near the tips of the inclined parent cracks. Once the wing reaches a certain length the failure would happen. The formation and evolution of wing cracks would be influenced by the grain size, temperature and friction coefficient which depends on the strain rate.

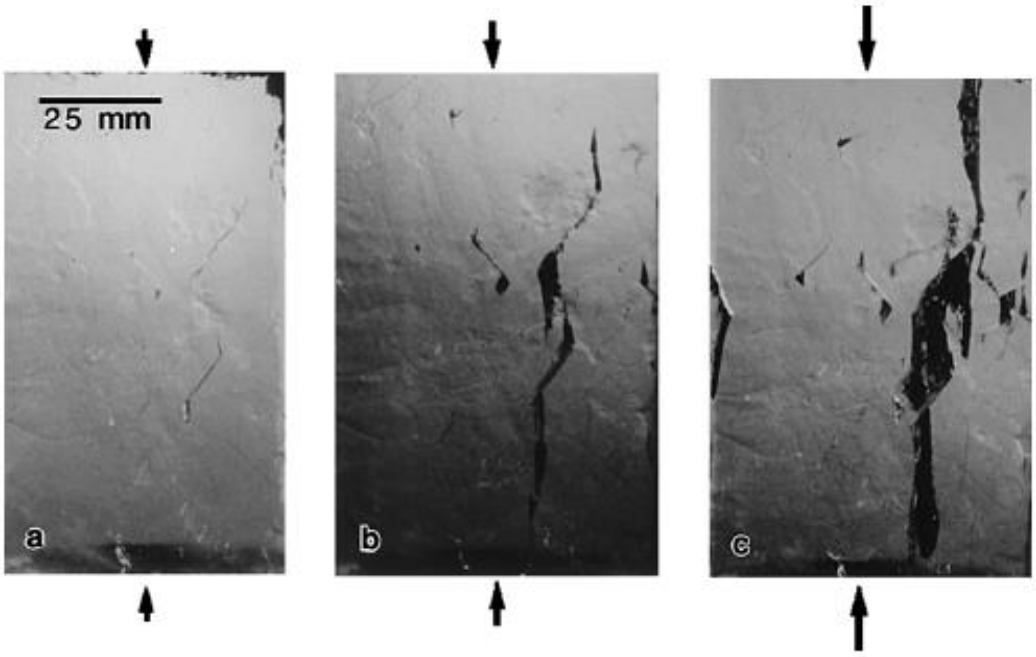

Figure 3-4 Crack propagations [28]

Compared with other brittle materials, the fracture toughness of ice is much smaller, and it does not depend significantly on temperature or loading conditions[32].

3.2 Ice impact mechanism

It has been found that the ice projectile would fail once it is in contact with the rigid target, but the failure is only localized to the contact point, while the geometry of the rest of the ice sphere kept very well with little change. But the failure would progress through the sphere as the ice projectile keep moving towards to the rigid target [27; 33] .

Figure 3-5 shows the macroscopic failure progress. The first stage of the impact can be regarded as crack formation. Once the ice projectile impacts onto the rigid target, cracks and local failure would happen immediately, and as the projectile keeps moving towards the target the cracks will grow in number density. An equal

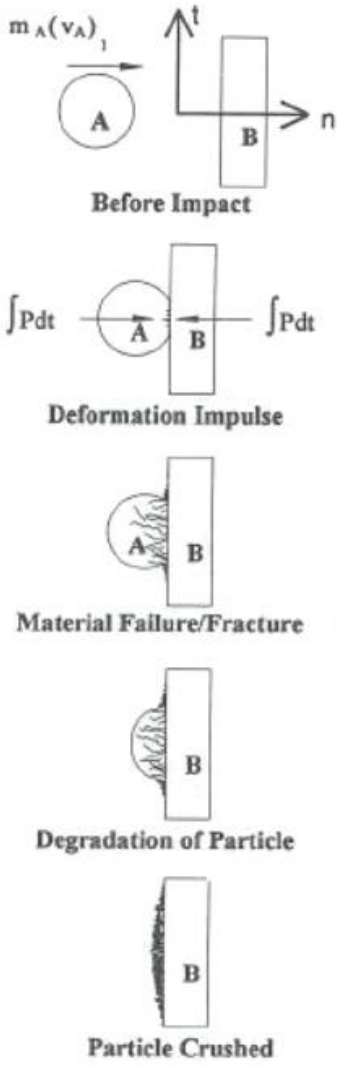

Figure 3-5 Ice impact process [33]

but opposite deformation impulse would be generated between the projectile and the target. The impulse would cause the local failure when the pressure reaches a certain threshold value [33].

The second period of the impact is cracks propagation. According the ice mechanism as mentioned in Chapter 3.1, without constraint the crack would grow longitudinally oriented along the opposite direction of impact to the end of the ice projectile. This expected phenomenon was observed in Tippmann's[14] test as shown in Figure 3-6 (c) (d). In this stage the rest of the ice projectile maintains its shape.

The third period is degradation, in which stage main cracks grow matured Figure 3-6 (e) (f) (g). As the projectile keep moving towards the target the rest of the projectile cannot keep its geometry, it begins degradation, and the projectile material flows from the contact point outwards to the rigid target edge.

The fourth period is the crushed period. In this stage the whole projectile is crushed.

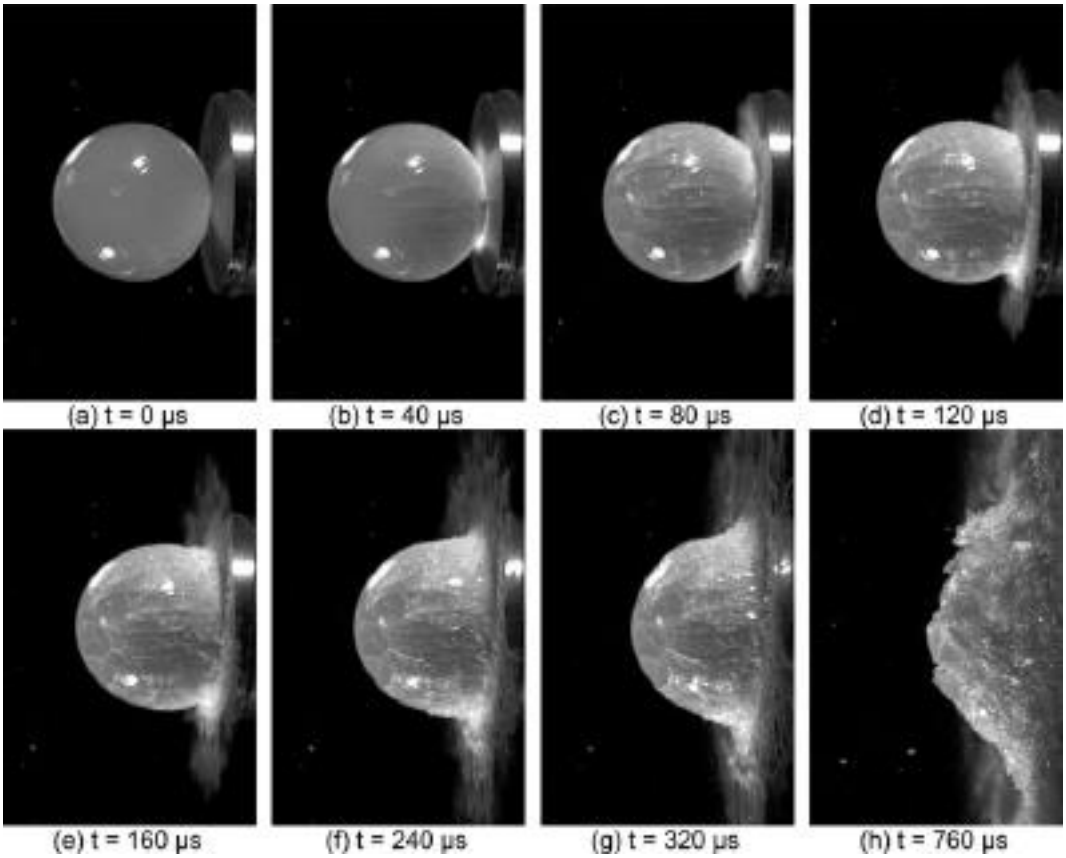

Figure 3-6 High speed photography of impact process [14]

3.3 Properties that need to be reflected in the material model

From the investigation of ice behaviour the following 8 important features of ice have been identified.

1. Different performance in tension and compression.
   Ice could be regarded as brittle material in tension. It is much more complicated under compression loading.
2. Strain rate sensitivity.
   The compressive yield stress is dependent on strain rate while the tensile strength can be regarded as a constant value.
3. Nonlinear response bulk response.
   The pressure cannot be simply described as the production of the bulk modulus and the volumetric strain.
4. Pressure dependence.

The compressive strength depends on the hydrostatic component of the applied stress. In this case, the crack mechanics and frictional sliding would decide the brittle failure.

5. Influence of loading condition.

   Without constraint under uniaxial loading the ice would fail via longitudinal splitting with the cracks forming when the stress reaches 0.2 to 0.3 of the failure stress.

6. Progressive failure of ice.

   The failure of the ice projectile happens immediately once the ice contacts the target, but the failure is only localized to the contact point, while the geometry of the rest of the ice sphere kept very well with little change.

7. Residual strength.

   As the ice breaks up, the crushed ice flows over each other and creates contact between grains that produces a residual strength after brittle failure. In other words, the ice particles behave like fluid, which can support a dynamic pressure loading.

8. Temperature dependence.

   As Coulomb's criterion is the appropriate one to define failure, the expression of this criterion is defined as the shear stress is a function of material cohesion and the product of the coefficient of internal friction and the normal stress across the plane. In these three parameters the coefficient of internal friction varies with the temperature, this feature leads to the temperature dependence.

4 TEST PROBLEMS

In this research, three different test problems have been selected to assess the current ice material model - Pressure recording test, Kim sphere ice test and Pereira cylinder ice test. These three test problems focus on different aspects of ice impact.

The pressure recording test is focusing on collecting a different type of test data. A new method to record test data was used in this test which records the contact pressure directly by using a pressure transducer. The Kim sphere test was selected because it is widely used nowadays. Many academics such as Truchelut [41] use this model to validate the ice material model. Thirdly the Pereira cylinder ice test was selected, because the shape of the projectile in this test is a cylinder which provides a different loading condition.

4.1 Pressure recording test

The pressure recording test was conducted by the author in NUAA prior to this research. The aim of this test is to collect the pressure history during the impact event. Pressure was measured by a pressure transducer (PPM-SY0302) as shown in Figure 4-1 installed on the centre of the rigid target as shown in Figure 4-2. This experiment is presented in detail in Appendix B.

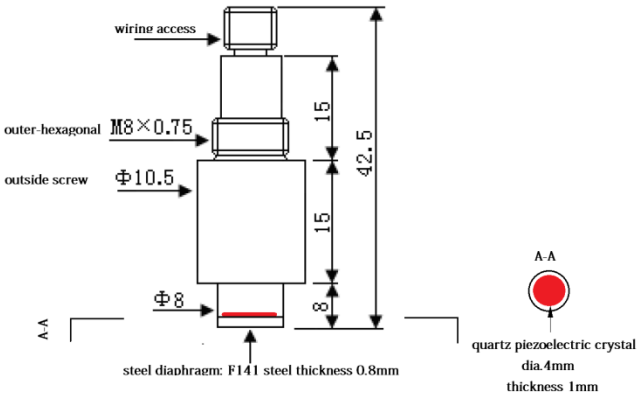

Figure 4-1 Pressure transducer

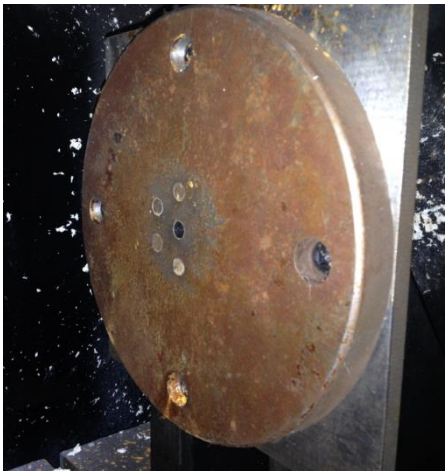

Figure 4-2 Rigid target

The properties of the target are clearly known. The diameter of the target is $20cm$, there are 5 transducers installed on the rigid target, one is located in the centre, the others are surrounding. The front face of the hole is 8.5 mm. the material of the target is medium carbon steel (No. 45). Thus the target can be built up in LS-DYNA in an accurate way. It needs to be noted that due to the ice projectile impacting onto the transducer directly, the pressure output in the numerical simulation needs to be the contact pressure.

The projectile used in this test is a transparent poly crystal ice sphere, which is frozen at -7°C from distilled water. The diameter of the sphere is 35mm and launched to a rigid target at a speed of 66m/s, 91m/s and 165m/s respectively.

4.2 Kim sphere ice test

The Kim sphere ice test [3] was chosen as an additional validation test problem because it is the most widely used test problem to simulate the ice impact event, and some other academics like Keune [24], Bee [42] have investigated ice by modelling Kim's test. In Kim's test the ice projectile was launched to a metallic target installed with a piezoelectric sensor, through which the dynamic force history during the impact can be recorded as shown in Figure 4-3.

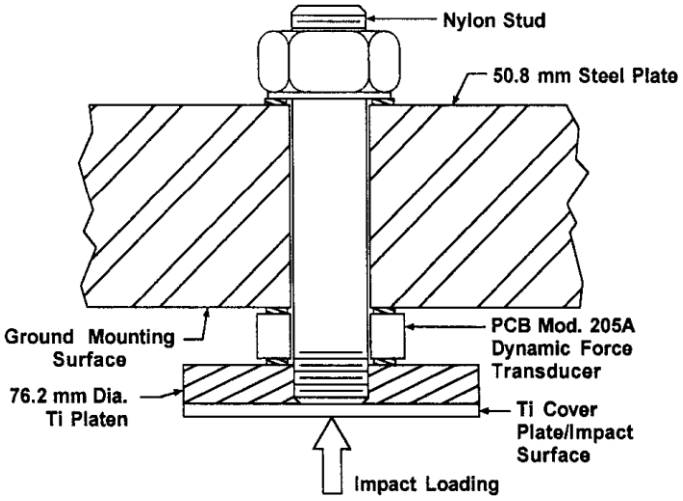

Figure 4-3 Load cell of Kim sphere test [3]

In this test the kinematic behaviour of the ice projectile was recorded by a high speed camera, through which Kim draws the conclusion that only a small portion of the sphere's volume has crushed by the time of peak force time [3]. This conclusion confirmed that during the impact the profile which is away from the target will keep its shape, and as the ice move towards the target, the failure would happen locally on the contact point.

Two types of spherical projectile were chosen in Kim's test – monolithic and flat-wise layered. It is needed to be noticed that the model of projectile in Kim's simulation is the monolithic ice projectile and the prediction of the impact force follows the trend of the impact force experimentally measured for monolithic ice projectile. The behaviour of the two types of ice projectile lie within the experimental scatter of each other. Thus the numerical model is an adequate representation for both ice projectile types within this range. The sizes of ice projectile tested were 25.4, 42.7 and 50.8 in diameter. The three different impact velocities were tested – 73.5m/s , 95.4m/s and 126m/s. Only the test data of the ice projectile with 42.7mm were shown comprehensively.

4.3 Pereira cylinder ice test

The projectile used in this test is an ice cylinder, which can be considered as a direct impact issue under a uniaxial loading. When the shape of the projectile is

different the loading condition is different. This test has been selected because with a different projectile shape the stress state is different. The test data was the force measured by force measurement transducer [7] which can be simplified as the load cell [4] shown in Figure 4-4.

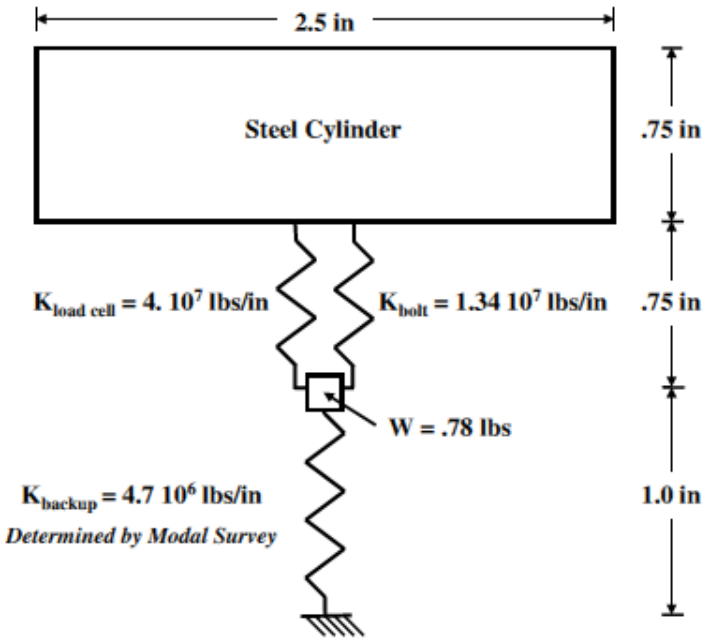

Figure 4-4 Load cell used in Carney's simulation [4]

This test was first used in the validation of Carney's ice model. Carney's material model was Implemented in LS-DYNA, and the material model's name is MAT 155 [9]. In the validation, Carney obtained a simulation result which is both quantitatively and qualitatively better than other ice models.

Three impact velocities were conducted in this experiment – 91.44 m/s, 152.4 m/s, 213.36 m/s. The projectiles tested in this experiment were made out of solid clear ice and lower density fabricated ice. Based on the crystalline form these projectiles were classified into three categories – single crystal, poly crystal and rejected poly-crystal due to imperfections. The ice cylinders were 17.5mm in diameter and and 42.2mm in length. The results of those experiments show that the crystalline form of the ice does not play a significant role in the impact force. Thus the influence from the crystalline form can be neglected.

5 NUMERICAL MODELLING INVESTIGATION

5.1 SPH method investigation

5.1.1 Principle

As the SPH method was found to be the closest way to simulate the ice projectile behaviour, and as it requires a smaller CPU-time than the FE method and the ALE method, it was selected as the simulation method in this research.

In the late 1970s, the Smoothed Particle Hydrodynamics (SPH) method was developed by Lucy [34], Gingold and Monaghan [35] in order to simulate astrophysics problems. Then this method was extended to the structural by Libersky et all [36].

The SPH method is a meshless computational method, solving continuously deformation problems through transporting a continuous medium into a finite set of interacting particles rather than depend on the grid, so it is a valuable tool to simulate large deformations and failure propagation.

The purpose of using the SPH method in computational engineering is to translate the conservation laws given in the form of partial equations into integrals, and then make it discrete on a domain. The conservation equation for mass, momentum and internal energy are given by Equation 5-1, Equation 5-2, and Equation 5-3, in Lagrangian framework [37].

$$\frac{d\rho}{dt} = -\rho \frac{\partial \dot{x_\alpha}}{\partial x_a} \qquad \textbf{Equation 5-1}$$

$$\frac{d\dot{x_\alpha}}{dt} = \frac{\partial}{\partial x_\beta}\left(\frac{\sigma_{\alpha\beta}}{\rho}\right) + \frac{\sigma_{\alpha\beta}}{\rho^2}\frac{\partial \rho}{\partial x_\beta} \qquad \textbf{Equation 5-2}$$

$$\frac{de_{int}}{dt} = \frac{\sigma_{\alpha\beta}}{\rho^2}\frac{\partial(\rho \dot{x_\alpha})}{\partial x_\beta} - \frac{\sigma_{\alpha\beta}}{\rho^2}\dot{x_\alpha}\frac{\partial \rho}{\partial x_\beta} \qquad \textbf{Equation 5-3}$$

The α and β denote the components: α (or x_β) =x, y or z.

5.1.2 Kernel function

Those conversion laws are transformed into integral equations through using the kernel interpolation function. A function f at the location x can be evaluated with the interpolation given in the Equation 5-4.

$$\langle f(x)\rangle = \int_{\Omega} f(x')\, W(x - x', h) dx' \qquad \textbf{Equation 5-4}$$

The brackets in Equation 5-4 denote the kernel approximation, and $W(x - x', h)$ is the kernel function. Thus a required variable can be estimated at any point in a domain, defined by the smoothing length, h, as shown in Figure 5-1.

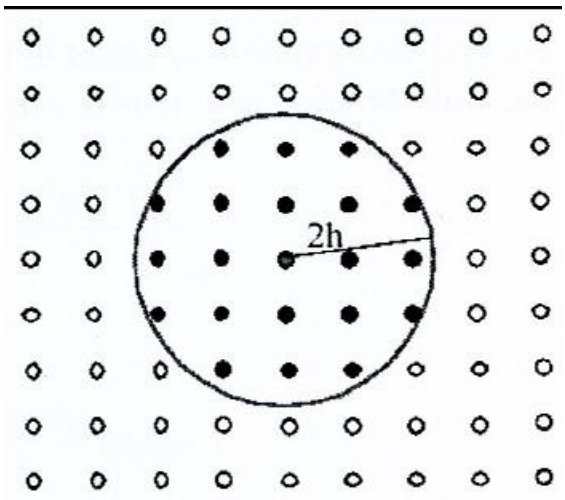

Figure 5-1 Set of Neighbouring SPH Particles [37]

Regarding the computation, the integral has to be transformed into a sum calculation on a number N of discrete points, as shown in Equation 5-5, if the function f is known [38].

$$\langle f(x^i)\rangle = \sum_{j=1}^{N} \frac{m^j}{\rho^j} f(x^j) W(x^i - x^j, h) \qquad \textbf{Equation 5-5}$$

The subscripts 'i' and 'j' represent the particle that is being calculated and a point within the domain respectively [42], and $\frac{m^j}{\rho^j}$ is the volume of the particle j [38].

There are several kernel functions which were used within the SPH method. Nowadays, the most common one used within three-dimensional models is the cubic B-spline function [37], defined by Equation 5-6, where y is given by Equation 5-7 and n is the number of dimensions in the model, C is a scaling factor that is dependent upon the number of dimensions in the model as shown in Equation 5-8.

$$W(q,h) = \frac{C}{h^n}\begin{cases} 1 - \frac{3}{2}q^2 + \frac{3}{4}q^3, & if\ 0 \le y \le 1 \\ \frac{1}{4}(2-q)^3\ , & if\ \ 1 \le y \le 2 \\ 0\quad\ , & if\ y > 2 \end{cases} \qquad \textbf{Equation 5-6}$$

$$q = \frac{\left|x^i - x^j\right|}{h} \qquad \textbf{Equation 5-7}$$

$$C = \begin{cases} \frac{2}{3}, & if\ n = 1 \\ \frac{10}{7\pi}\ , & if\ \ n = 2 \\ \frac{1}{\pi}\ , & if\ n = 3 \end{cases} \qquad \textbf{Equation 5-8}$$

There are 3 properties of this three kernel function.

The first one is that it has a compact support equal to $2h$ which can be represent by Equation5-9, that means there is no interaction occurring outside the circle whose centre is x and radius is h.

$$W\left(x^i - x^j, h\right) = 0,\ \ if\ |x - x'|\ \ge 2h \qquad \textbf{Equation 5-9}$$

The second one is that it has to equal to Dirac delta function when 'h' tends to zero as shown in Equation 5-10

$$\lim_{h\to 0}\langle f(x)\rangle = f(x) \qquad \textbf{Equation 5-10}$$

The third one is that it is normalised within its domain as shown in Equation 5-11

$$\int_{\Omega} W(x,h)dx = 1 \qquad \textbf{Equation 5-11}$$

After using Taylor series about x= x', integration by parts and Green's theorem, we obtain the derivation of the SPH Equations transformed from the conservation equations given by Equation 5-12, Equation 5-13, Equation 5-14.

$$\frac{d\rho^i}{dt} = \sum_{j=1}^{N} \frac{m^j}{\rho^j}(\dot{x}_\beta^j)\frac{\partial W(x^i - x^j, h)}{\partial \dot{x}_\beta^i} \qquad \textbf{Equation 5-12}$$

$$\frac{d\dot{x}_\alpha^i}{dt} = \sum_{j=1}^{N} m^j\left(\frac{\sigma_{\alpha\beta}^j}{(\rho^j)^2} - \frac{\sigma_{\alpha\beta}^i}{(\rho^i)^2}\right)\frac{\partial W(x^i - x^j, h)}{\partial \dot{x}_\beta^i} \qquad \textbf{Equation 5-13}$$

$$\frac{de_{int}^i}{dt} = \frac{\sigma_{\alpha\beta}^i}{(\rho^i)^2}\sum_{j=1}^{N} m^j(\dot{x}_\alpha^j - \dot{x}_\alpha^i)\frac{\partial W(x^i - x^j, h)}{\partial \dot{x}_\beta^i} \qquad \textbf{Equation 5-14}$$

5.1.3 Variable smoothing length, *h*

The smoothing length, noted by h, discussed above remains constant. However, under large deformation conditions, the interaction between particles can either become negligible or too significant due to their extreme distances. In this situation the calculation would slow down. This problem can be solved through using an adjustable smoothing length shown by Equation 5-15 [38].

$$h = h_0\left(\frac{\rho_0}{\rho}\right)^{\frac{1}{n}} \qquad \textbf{Equation 5-15}$$

Where h_0 and ρ_0 are the initial smoothing length and density respectively, and n is the number of dimensions.

5.1.4 Shortcomings of the SPH method

Although the SPH method has significant advantages dealing with large deformation problems, it has some limitations such as tensile instability, zero energy modes and consistency.

5.1.4.1 Tensile instability

During the simulations with the SPH method, a clustering of particles may occur which revealed instability from the artificial defect within the code. According to Swegle's research, this phenomenon does not come from the numerical time integration algorithm [38], but from an interaction between the constitutive relation and the kernel interpolation [37]. A stability criterion shown as Equation 5-16 was introduced by him. In Equation 5-16, the W represents the kernel function and W'' represents the second derivative with respect to its argument, and σ is the stress which was defined positive in tension and negative in compression.

$$W''\sigma < 0 \qquad \textbf{Equation 5-16}$$

A stability regime for the B-spline kernel function is given in Figure 5-2.

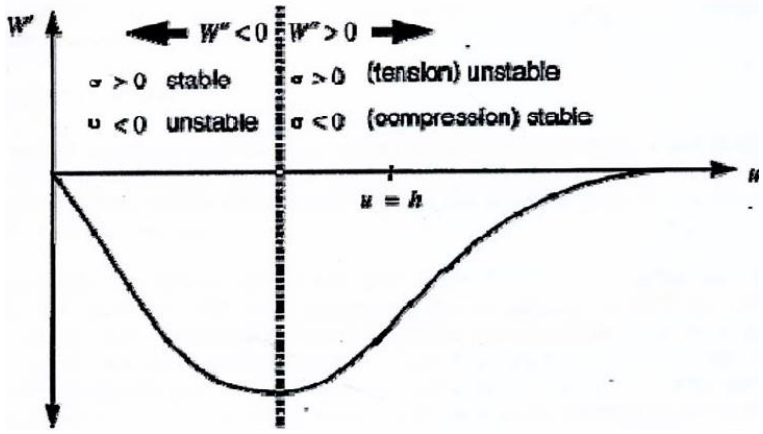

Figure 5-2 Stability regime for the B-spline kernel function [37]

From this figure, it can be found that the particle spacing needs to ensure the model remains stable both in compression and in tension. It can also be found that the instability occurs more readily under tensile loading.

5.1.4.2 Zero energy modes

Not only the Finite Element of Finite Different methods in the SPH method will also appear Zero-Energy modes which result from a pattern of nodal displacement with a strain energy equal to zero. It will occur when an element is under integrated. An example of this would occur when there is an oscillatory variable within the model Figure 5-3 thus causing negligible gradients at each point and therefore similar stress values.

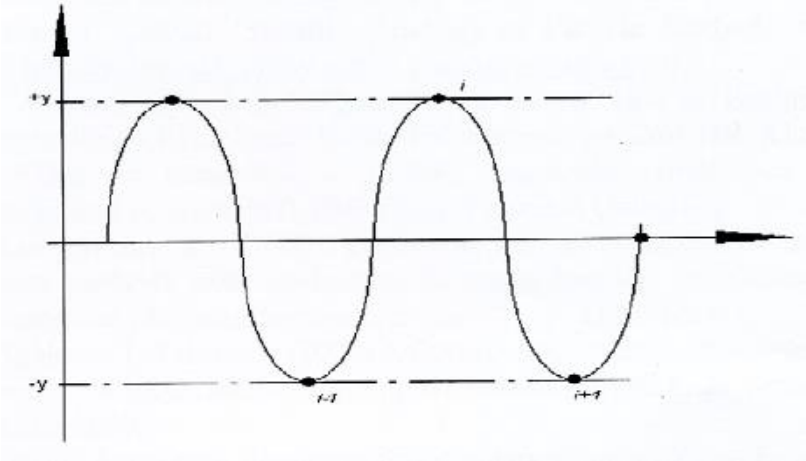

Figure 5-3 Zero Energy Modes [37]

5.1.4.3 Consistency

This short coming is related to the boundary condition. Under the free boundary condition, problems will arise due to the fact that neighbouring particles are not equally distributed within the kernel's domain [43]. A number of attempts has been made this problem to be addressed. For instance, Johnson [39] introduced the concept of Normalised Smoothing Function. It consists of basically in correcting the kernel function and then correcting the discrete form of the convolution integral of the SPH interpolation. Vignjevic improved this method with a kernel normalisation and correction called Corrected Normalised Smooth Particle Hydrodynamics (CNSPH) [35]. Consequently, boundary conditions are not any longer ignored in the SPH formulation.

5.2 Theoretical assessment of constitutive models available

The objective of this research is to optimise the current ice material model. So the evaluations of current ice material models need to be done first. Five material models have been investigated. Three of them are developed specifically for ice the other two are basic elastic plastic metallic material models which have been used in modelling ice before. Currently, there are three models that are available to use in LS-Dyna- MAT 13 which were used in the early stages of modelling ice [3]; MAT 10 which has been proved to be more accurate than Mat 13 in ice modelling by Marco [25]; MAT 155 which is the only model developed aimed at modelling ice [4]. The other two material models are user defined model in Abaqus and LS-Dyna respectively. Jeffery's model is a Abaqus user defined model which has the same function of MAT 155 [15]; Pernas's model is a user defined material model in LS-Dyna which used the Drucker-Prager yield function to reflect the pressure dependence [8].

5.2.1 MAT 10 (*MAT_ELASTIC_PLASTIC_HYDRO_{OPTION})

MAT 10 is a simple bilinear Isotropic Harding material model with equation of state and failure [9]. The plastic behaviour will be discussed in Chapter 5.2.2, it is the same as MAT 13. The application of the equation of state can reflect the nonlinear relationship between pressure and volume during the impact event.

Three failure criteria can be chosen in this material model - cut-off pressure, maximum principle stress and the combination of these two criteria. The cut-off pressure failure mode can present the ice failure behaviour. When the pressure cut-off is reached the deviatoric stresses and any tensile pressure are set to zero in order to prevent tensile loading which is quite similar to the failure criterion in MAT 13.

The disadvantage of this material is that the strain rate dependent failure strength which is the most significant characteristic of ice has not been taken into consideration, which was also seen in MAT 13. But compared to MAT 13, MAT 10 can provide a higher degree of accuracy, due to the application of the equation of state.

5.2.2 MAT 13 (*MAT_ISOTROPIC_ELASTIC_FAILURE)

This is a simple bilinear Isotropic hardening material model with failure [9].

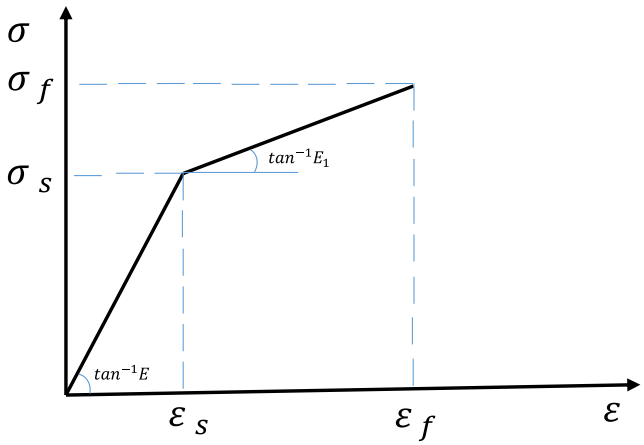

Figure 5-4 Strain-stress relationship

In the bilinear isotropic hardening model, material behaved like an elastic material as in Equation 5-17 before it reaches the yield stress, after that, it will go through the plastic process, the strain-stress relationship will change in to Equation 5-18.

$$\sigma = E\varepsilon \qquad (\sigma \le \sigma_s) \qquad \textbf{Equation 5-17}$$

$$\sigma = \sigma_s + E_1(\varepsilon - \varepsilon_s) \quad (\varepsilon \le \varepsilon_f) \qquad \textbf{Equation 5-18}$$

In this material, the user can input these parameters below

Table 5-1 Parameters need to be defined in MAT 13 [9]

Shear modulus.	G
Yield stress.	σ_s
Plastic hardening modulus.	E_1
Bulk modulus.	K
Plastic failure strain.	ε_f

Failure pressure	$P_{failure}$

From the relationship function among E , K , G

$$E = \frac{9KG}{3K + G} \qquad \textbf{Equation 5-19}$$

In MAT 13, the relationship between strain-stress can be described as equation 5-20,21.

$$\sigma = \frac{9KG}{3K + G}\varepsilon \qquad (\sigma \le \sigma_s) \qquad \textbf{Equation 5-20}$$

$$\sigma = \sigma_s + E_1(\varepsilon - \varepsilon_s) \quad (\varepsilon \le \varepsilon_f) \qquad \textbf{Equation 5-21}$$

Before failed, MAT 13 allows a plastic hardening behaviour that adequately reproduces the effect of the propagation of the micro cracks inside the ice before it crushes and reaches a fluid-like state.

After failed, when the pressure reaches the failure pressure, the element will lose its ability to carry tension and the deviatoric stresses are set to zero. This means $s_{i,j} = 0$, so the stress would be $\sigma_{i,j} = \delta_{i,j}\sigma_0$.

Based on the ice engineering properties and the impact mechanism discussed in Chapter 3, this model has its limitations in describing ice material. Firstly, the yield stress is a constant value which is dependent on the pressure in ice; secondly, there is no equation of state that can be used in this material, that makes MAT 13 non-linear relationship between the pressure and the volumetric strain; thirdly, as discussed in Chapter 3 the ice behaves significantly differently in tension and compression, but in this material model the failure stress is the same for both tension and compression and is not a function of the strain rate or pressure.

5.2.3 Carney's model (MAT 155)

MAT 155 is the only model developed for ice which is available for use in commercial code [8]. It is a phenomenological model rather than physics based model which is not trying to model the physics of ice but focusing on the behaviour of ice linking to the phenomena of the test.

The advantage of MAT 155 is that it is equipped with strain rate dependence, equation of state and different initial flow stress in tension and compression. The strain rate dependence is reflected as equation 5-23.

$$\bar{\sigma} = \hat{s}(|\boldsymbol{D}|, P) \cdot \hat{\sigma}_f(\bar{\epsilon}^P) \qquad \textbf{Equation 5-22}$$

Where $|\boldsymbol{D}|$ is the strain rate, $\bar{\sigma}$ is the flow stress, $\hat{s}$ is a scaling function composing two tabular functions which can represent the strain dependent relationship of ice.

The Equation of State used in MAT 155 is the compaction tabulate EOS in the form of:

$$P_{EOS} = \hat{C}(\epsilon_V) + \gamma \hat{T}(\epsilon_V) E \qquad \textbf{Equation 5-23}$$

$$\epsilon_V = \ln(V/V_0)$$

V_0 is the reference specific volume, E is the internal energy per reference volume, $\hat{C}$ and $\hat{T}$ are compression and tension tabular function, γ is the Gruneisen coefficient, which was set as zero in Carney's simulation.

The pressure used there can be evaluated by a tabulated equation of state, which can model the non-linear response accurately.

The pressure cut-off failure mode is the same as MAT 13 in the form of:

$$d^p = \begin{cases} 0 & if \;\; P > P_{cut-off} \;\; or \;\; P < P^T{}_{fail} \\ 1 & otherwise \end{cases} \qquad \textbf{Equation 5-24}$$

Currently, MAT 155 is regarded as the proper ice material model. But through the validation, it has been found that, although it can model cylinder ice perfectly, when modelling sphere ice the result does not seem that good, which will be discussed in Chapter 5.3 in detail. In addition, according to the mechanism of ice,

it is a kind of temperature dependent material, but in this model, this characteristic was neglected.

5.2.4 Jeffery Abaqus model

The failure mode of this material model is the same as MAT 13. Elastic properties of ice were chosen in this material set up. Since high velocity ice impacts can be considered as perfectly plastic, in this material model, a zero plastic hardening modulus was applied [15]. But the ice has been proved to have a hardening property after yield [27].

The improvement of this model is the addition of the strain rate dependent yield strength. In the same way as MAT 155, the strain rate dependent yield strength is presented as tabular data.

5.2.5 Pernas-Sánchez's constitutive model

As in MAT 155, the strain rate dependence and the same failure mode are composed in this material model as well. The improvement of this material model is that the influence of the current pressure on the yield stress is taken into consideration by implying the Drucker-Prager yield function rather than the Von-Mises yield function.

In this constitutive model, the author defines the deformation of the material as hypoelastic approach [8].

The motion of the material, $\mathbf{dx}$, was described through the deformation gradient tensor, $\mathbf{F}$, and an infinitesimal material vector, $\mathbf{dX}$, as described in equation 5-25.

$$\mathbf{dx} = \mathbf{F}\mathbf{dX} \qquad \textbf{Equation 5-25}$$

$\mathbf{F}$ can be assumed as Kroner-lee multiplicative split form which can separate $\mathbf{F}$ into reversible elastic deformation, $\mathbf{F}^e$, and inelastic deformation, $\mathbf{F}^p$, as shown in Equation 5-26.

$$\mathbf{F} = \mathbf{F}^e\mathbf{F}^p \qquad \textbf{Equation 5-26}$$

Under the consideration of the impact application, comparing to the plastic strains and rates, the elastic strains and rates are always very small. In this case the Kroner-lee multiplicative split can be changed into additive decomposition of the rate of the deformation tensor in its corresponding elastic and plastic components, as shown in Equation 5-27.

$$\mathbf{d} = \mathbf{d}^e + \mathbf{d}^p \qquad \textbf{Equation 5-27}$$

For the elastic component within hypoelastic behaviour, the relationship between strain rate and stress rate can be expressed by Hooke's law, as shown in Equation 5-28.

$$\boldsymbol{\sigma}^{\nabla} = \boldsymbol{C}\colon \mathbf{d}^e = \boldsymbol{C}\colon (\mathbf{d} - \mathbf{d}^p) \qquad \textbf{Equation 5-28}$$

$\boldsymbol{\sigma}^{\nabla}$ is an objective rate of the Cauchy stress tensor and $\boldsymbol{C}$ is the Hooke stress-strain tensor defined by the elastic constants G and K.

The pressure dependence was defined as the Drucker and Prager yield function as shown in Equation 5-29.

$$f = \bar{\sigma} - (\sigma_{0y} + 3\alpha p) \qquad \textbf{Equation 5-29}$$

$\bar{\sigma}$ is equivalent stress which can be represented by deviatoric stress tensor, σ_{0y} is material cohesion and 3α is a parameter related to the internal friction angle of the material. Both σ_{0y} and 3α are represented by the uniaxial initial flow stress in compression σ_C and in tensionσ_T.

p is the hydrostatic pressure in the form of:

$$p = -\frac{\boldsymbol{\sigma}\colon \mathbf{1}}{3} \qquad \textbf{Equation 5-30}$$

Thus the Drucker-Prager yield surface is completely shown in Figure 5-5.

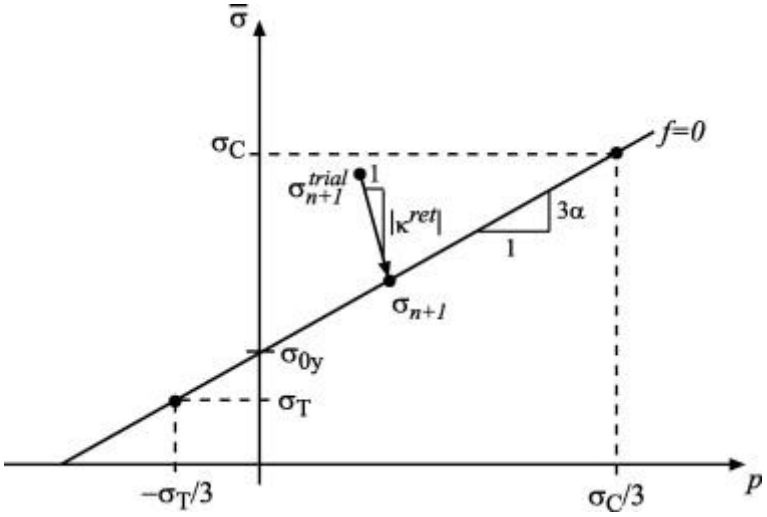

Figure 5-5 Drucker-Preager yield surface [8]

But there are two potential inaccuracies existing in this material model to reflect the ice behaviour.

1. According to the Drucker-Prager yield criteria, in metal plasticity the material cohesion, σ_{0y}, is equivalent to the current yield stress[26]. Additionally, the initial yield stress is different in tension and compression.
2. In his article the pressure has a linear relationship with the volumetric strain. But the relationship between the pressure and the volumetric strain has been proved to be nonlinear [9].

5.2.6 Conclusion

MAT 13 is a simple bilinear Isotropic hardening material model. Pressure and volumetric strain are simply related by the bulk modulus. When the pressure reaches the failure pressure the material will fail then the deviatoric stresses and the tensile pressure are set to zero.

MAT 10 is quite similar to MAT 13, but the containment of the equation of state makes it more accurate than MAT 13.

MAT 155 seems to be the most appropriate ice material model that is equipped with EOS, strain rate dependence.

The Jeffery Abaqus model is composed of simple elastic-plastic behaviour with failure criterion based on tensile pressure. The plastic yield stress contains the strain rate dependency using the dynamic compressive strength data. But it used a zero plastic hardening modulus.

Although the Pernas-Sánchez model is equipped with the pressure dependence of the yield stress, there are two potential inaccuracies existing in this material model to reflect the ice behaviour.

Based on the mechanism of ice material and the assessment of the current material models, the most complete ice model needs to include the following features:

1. Strain rate dependence.
   Strain rate dependence is the basic and specific characteristics of ice. The strain rate dependence can either be reflected through Carney's way [4] using tabular data to represent the relationship between yield stress, pressure and strain rate, or reflected through the Pernas-Sánchez way[8] by using a power law with strain rate sensitivity.
2. Nonlinear bulk response.
   EOS to be used for calculation of the pressure. The compaction feature of the equation of state has facilitated the matching of the calculation response to the experiment [4].
3. Pressure dependence.
   It has been proved that the compressive strength depends on the hydrostatic component of the applied stress [27]. The Drucker-Prager yield criteria can reflect this dependence [8].
4. Fluid like post-failure behaviour.
   After the ice fails, the ice will behave like fluid, which means that the ice will lose its ability to carry the sheer stress and the tensile pressure [27]. The deviatoric stress and the tensile pressure will be set to zero after failure.

5.3 Numerical assessment of constitutive models available in LS-Dyna

MAT 13 and MAT 155 are chosen to conduct the numerical assessment. As a typical metallic material model MAT 13 is chosen to investigate how well a metallic material model can reflect the ice properties. Mat 155 is the only material model available to use in commercial code which is developed specifically for ice. This material model is chosen to investigate its performance through different test problems.

5.3.1 Pressure recording test

A pressure transducer is used to record the pressure time history of this test. The projectile used in this test is a transparent ice sphere with a diameter of 35mm.

5.3.1.1 Model of the rigid target

Since the pressure transducer is installed in the centre of the rigid target and measures the impact pressure directly, in order to simplify the pressure measurement transducer the rigid target equipped with the pressure transducer is simplified as a solid plate that has the same diameter and the same thickness. It has been found that the mesh density of the target has a very small influence on the result, so it just needs to be small enough to avoid penetration problems with SPH nodes. As a rigid target, the constraint of the plate is “full constrained”.

The target used in this experiment is a titanium alloy plate with 200mm diameter and 20mm thickness. The parameters used in this target model are listed in Table 5-2. The model of this target is shown in Figure 5-7.

Table 5-2 Parameters used in modelling the rigid target of pressure recording test

Density	4400kg/m^3
Young’s modulus	109GPa
Poisson’s ratio	0.34
Diameter	200mm
Thickness	20.0mm

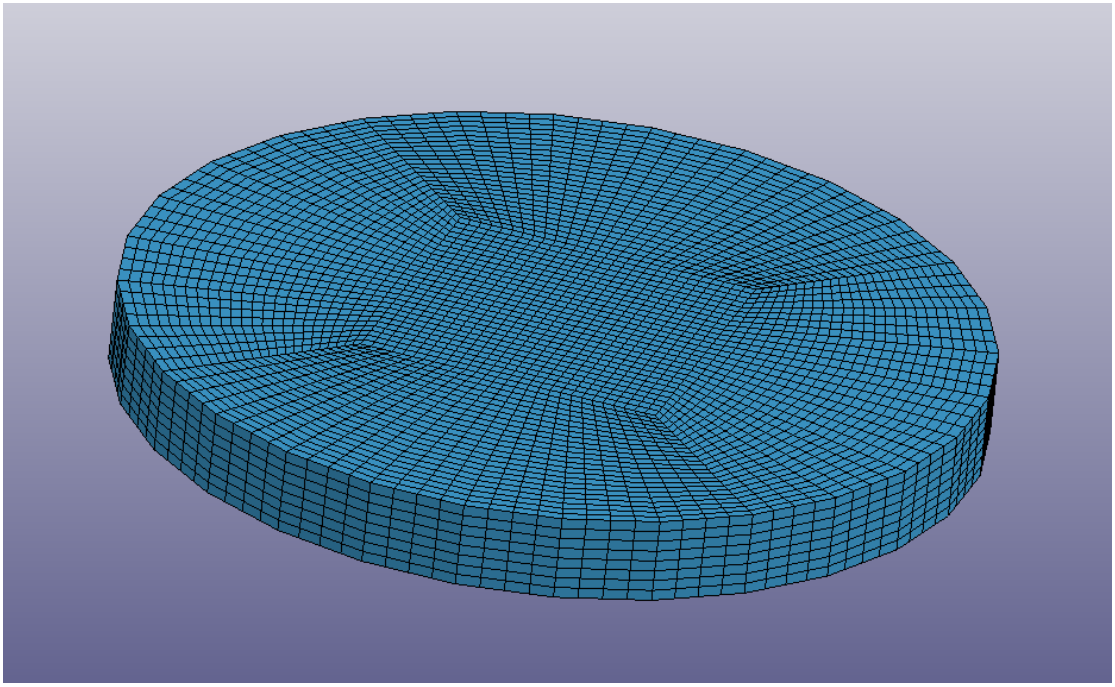

Figure 5-6 The model of rigid target of the pressure recording test

5.3.1.2 Model of the ice projectile

An SPH sphere with the same diameter of the ice projectile used in pressure recording test was modelled. The parameters used in the MAT 155 are listed in Tables 5-3, 4, 5, 6 which will also be used in the tests later on, the only change in the other test is the geometry of the projectile. The curve describing yield stress versus effective plastic strain in compression is listed in Table 5-4. The curve defining the yield stress versus effective plastic strain in tension is listed in Table 5-5. The equation of state needed by MAT 155 is listed in Table 5-6. The parameters used in MAT 13 are listed in Table 5-7. One thing needed to be noticed is that to make the computing fast the computation of the smoothing length during the initialization is set as the default form.

Table 5-3 Parameters used in modelling the ice projectile (MAT 155)[4]

Parameter	Value
Density	897kg/m^3
Young's modulus	9.3GPa

Poisson’s ratio	0.33
Compressive mean stress	6894.75Pa
Tensile mean stress	-6894.75Pa
Pressure cut-off in compression	4.93MPa
Pressure cut-off in tension	0.433MPa
Diameter	35mm

Table 5-4 yield stress versus effective plastic strain in compression[4]

Effective plastic strain	Yield stress
1.8711e-2	172.40MPa
0.35	174.68MPa

Table 5-5 yield stress versus effective plastic strain in tension[4]

Effective plastic strain	Yield stress
1.8711e-3	17.24MPa
0.35	19.639MPa

Table 5-6 yield stress versus effective plastic strain in compression[4]

Volumetric strain	Pressure	Bulk modulus
0	0	8963.2MPa
-7.693e-3	68.95MPa	8963.2MPa
-3.125e-2	68.95MPa	2206.3MPa
-10	68.95MPa	6.89MPa

Table 5-7 Parameters used in modelling the ice projectile (MAT 13)[3]

Parameter	Value
Density	897kg/m^3
Sheer modulus	3.46GPa
Yield stress	10.3MPa
Plastic hardening modulus	6.89GPa
Bulk modulus	-6894.75Pa
Failure pressure	-4MPa

The first step is mesh density study. This study is aimed at investigating the most appropriate mesh density to simulate the pressure recording test. The different

configurations which are employed in this study are listed in Table 5-8, and the result was shown in Figure 5-7.

Table 5-8 Mesh density configuration

Name	D14	D20	D22	D25	D30	D35
Number of particles across diameter	14	20	22	25	30	35

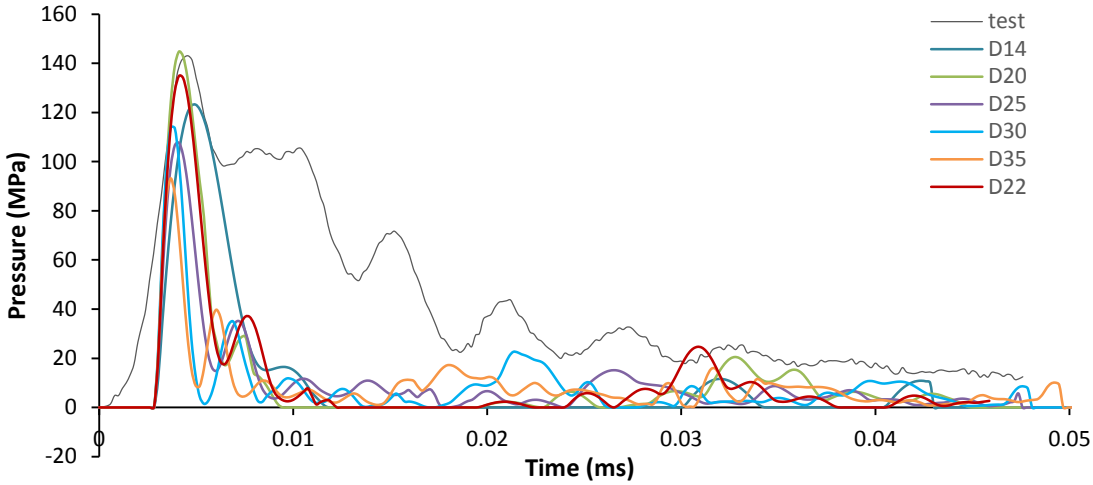

Figure 5-7 Mesh density study results

It can be inferred that when increasing the number of particles across the diameter from 14 to 20, the peak contact pressure increased about 16.3%, but after that the peak contact pressure begins to decrease and is shifting, especially when the number of particles across the diameter increases to 35 the magnitude of peak contact pressure dropped to 66% of the test magnitude.

The situation of the second peak contact pressure is the same as the first peak contact pressure, but after the number of particles across the diameter reaches 22 it becomes stable, the errors among these 4 tests are within 5%.

From this study, it can be found that when the number of particles across the diameter is 22, the simulation is closest to the test result.

5.3.1.3 Contact condition

In order to reflect the transducer, a contact with the same area as the front end of the transducer was set as shown in Figure 5-8. Each element is 0.00252579m long, and the area of the each element is 6.651241E-6m^2. This contact contains the centre 12 elements; the total area is 7.9814892E-5m^2. While the actual transducer's area is 5.042E-5m^2 which is a circle area whose radius is 0.004m.

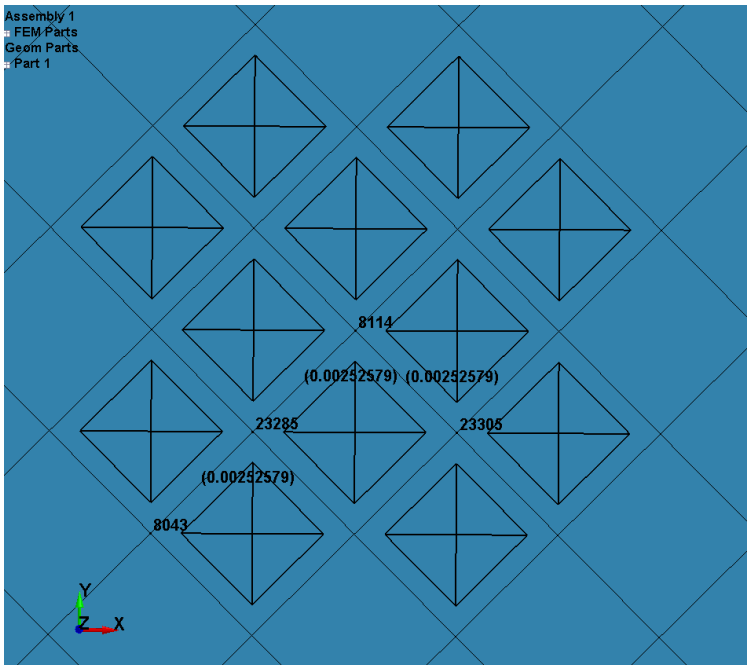

Figure 5-8 Contact area

According to the user manual of LS-Dyna [9], "*CONTACT_AUTOMATIC_NODES_TO_SURFACE" card was used in defining the contact between finite element and SPH nodes. An offset in contact was built under the consideration of the size of SPH particles.

5.3.1.4 Different impact speed simulation

Three different impact speeds are simulated - 66m/s, 91m/s and 165m/s. The simulation pressure time history is shown in Figures 5-9, 10, 11.

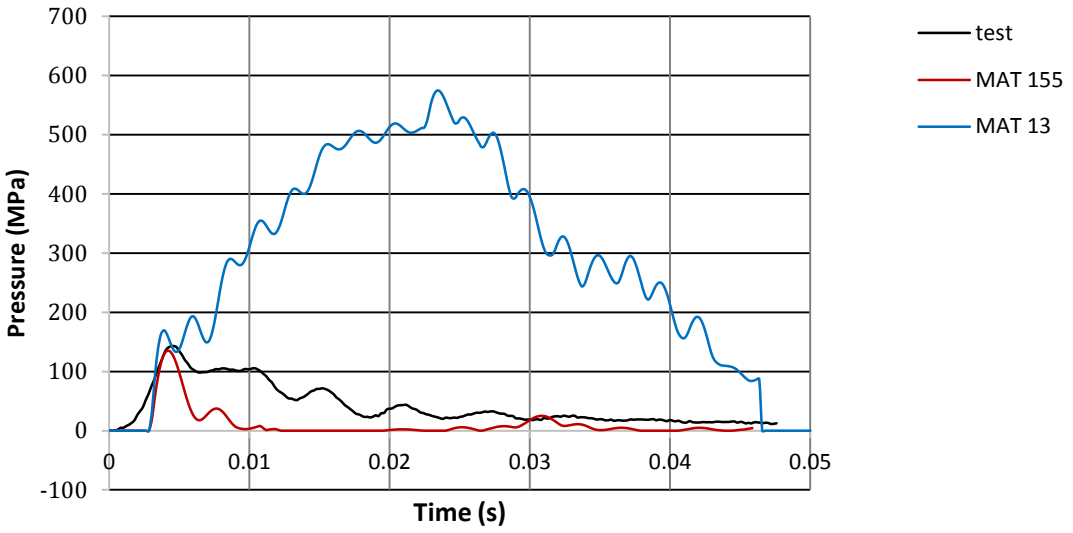

Figure 5-9 Impact pressure of Pressure record test model (66m/s)

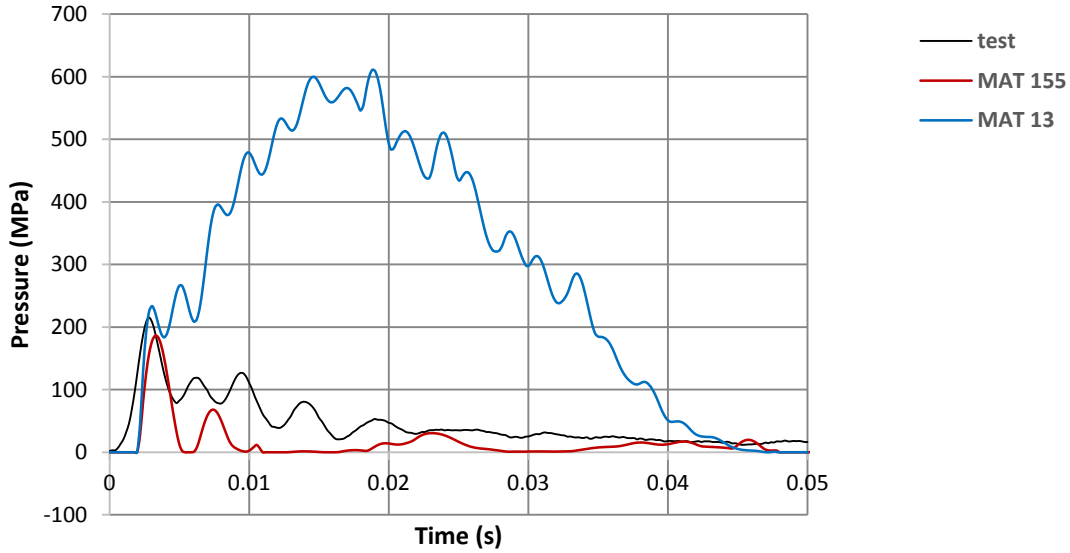

Figure 5-10 Impact pressure of Pressure record test model (91m/s)

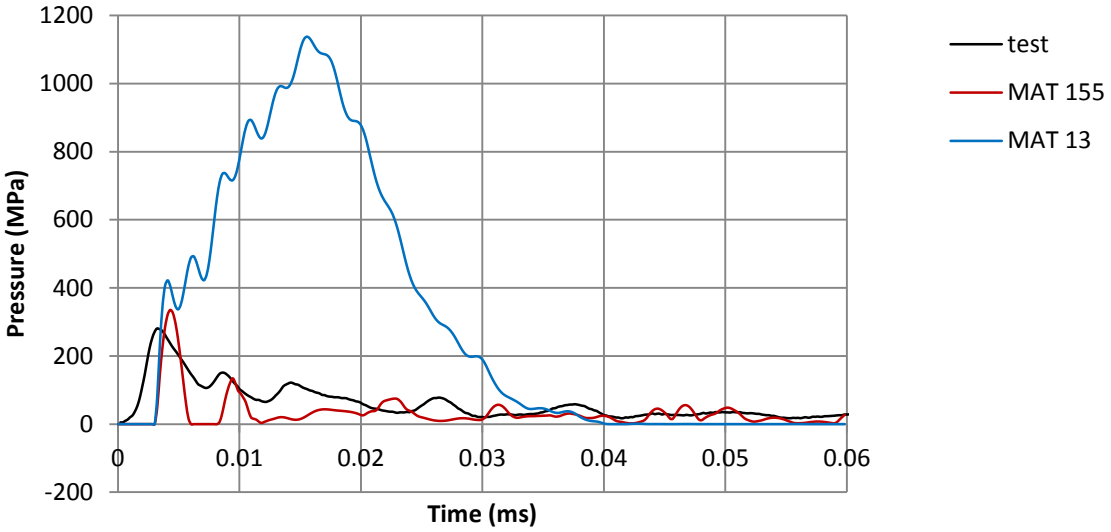

Figure 5-11 Impact pressure of Pressure record test model (165 m/s)

From the results of these three different simulations it can be inferred that MAT 155 can predict the magnitude of the peak pressure on the transducer's area well, while the MAT 13 cannot predict the pressure trends at all.

To investigate the pressure on the rest of the area of the rigid target, the pressure of the second contact is plotted in Figure 5-12.

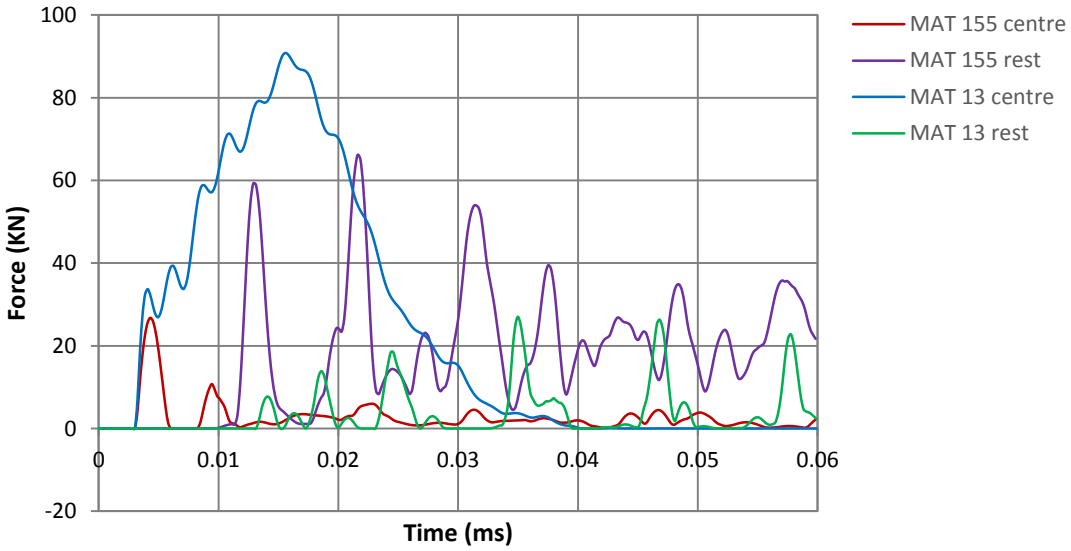

Figure 5-12 Total contact force history at 165m/s

The red and blue curve represent the contact force on the transducer area of the MAT 155 test and MAT 13 test respectively; the purple curve and the green curve represent the contact force on the rest of the target area of the MAT 155 test and the MAT 13 test respectively. It can be inferred that although there is a big contact force on the impact centre area, but there still exists contact force which cannot be neglected on the rest of the contact face. This shows that there is a distribution of the contact force on the contact interface.

It can be noticed that the maximum contact force of the MAT 13 test takes place at the centre area; however the maximum contact force of MAT 155 test takes place at the rest of the area of the target. Comparing these two contact force it can be found that the magnitude and the time of them are quite coincided.

As described in Chapter 3.3, one of the features of ice is progressive failure- the failure of the ice projectile happens once the ice contacts the target, but the failure is only localized to the contact point, while the geometry of the rest of the ice sphere kept very well with little change. Thus the maximum force should take place at the rest area of the target.

This study indicates that, MAT 13 is not suitable for the ice material, because it will generate a huge contact force concentration on the centre area at the early stage of the impact process. MAT 155 can reflect the pressure distribution which is a symbol of the ice projectile that can keep its geometry in the early stage of the impact which has been discussed in Chapter 2.2.

5.3.2 Kim's sphere ice test

The basic process of this simulation is quite similar to the Pressure recording test simulation, so there is only need to make a brief introduction to this simulation process, the highlight is put on the test results analysis.

The force measurement transducer was adopted in this test to record the impact force. According to the Carney article [4], simplify the force measurement transducer as a load cell which is a structure with plate and spring is an

appropriate way to model it. Thus in this research the force measurement transducer is simplified as structure with a solid plate and a single spring element which is shown in Figure 5-13, and the centre node on the bottom of this plate was shared by the spring. The parameters and geometry of the plate and the spring are listed in Tables 5-9, 10.

Table 5-9 Parameters used in modelling the force measurement transducer in Kim's test – Plate

Parameter	Value
Density	4400kg/m^3
Young's modulus	109GPa
Poisson's ratio	0.34
Diameter	76.2mm
Thickness	20.0mm

Table 5-10 Parameter used in modelling the force measurement transducer in Kim's test – Spring

Parameter	Value
Elastic stiffness	7GPa
Length	20.0mm

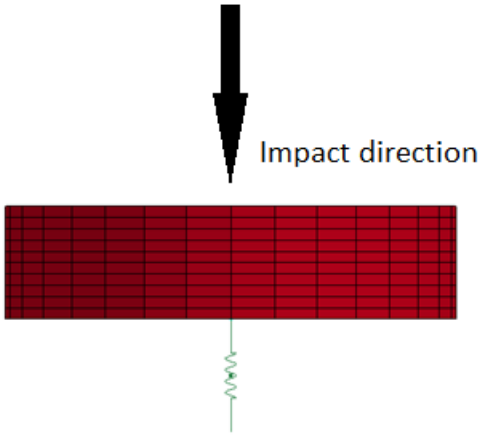

Figure 5-13 Simplification of force measurement transducer used in Kim test

There were three different diameters for the ice spheres 25.4mm, 42.7mm and 50.8mm, created either layer by layer, which aims to represent the layered structure of the real hail or monolithic ice. Even though the data from the Kim article is the layered ice sphere test result, but since Kim draw a conclusion that the monolithic sphere model can reflect the layered sphere thus in this research the sphere was built as monolithic sphere. The tests with a diameter of 42.7mm were detailed in Kim's simulation. Thus in this investigate study, the ice projectile is assumed as monolithic ice with a diameter of 42.7mm.

Three impact velocities were performed in Kim's test and all of these velocities were simulated.

In Kim's simulation the sphere-to-plate interface contact force was chosen as the impact force, but in Carney's simulation the inner force of the spring was chosen as the impact force. To investigate which way is more accurate to get the impact force, both of these two forces are out-put in this simulation.

Figures 5-15, 17, 19, show the numerically predicted force history from three different tests. The peak force and the error from three different tests are shown Table 5-11.

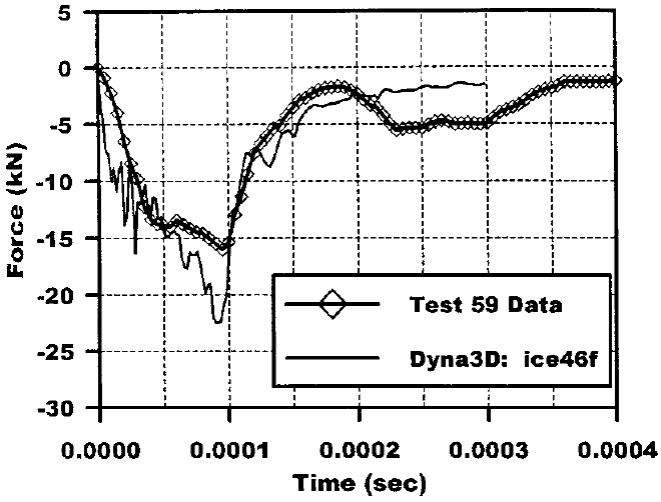

Figure 5-14 Test at 73.5 m/s [3]

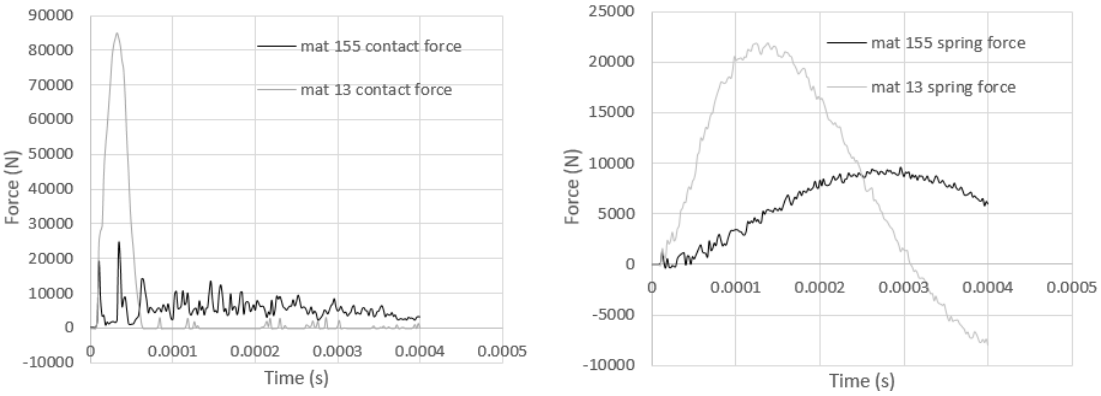

Contact force Inner spring force

Figure 5-15 Simulation of Kim's test (73.5 m/s)

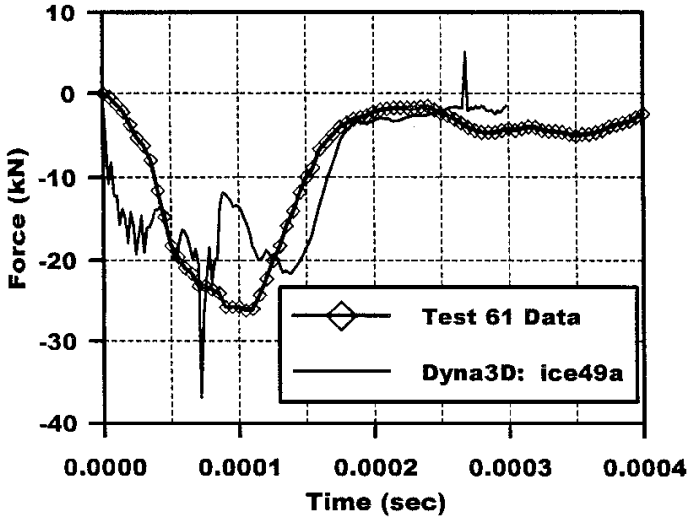

Figure 5-16 Test at 95.4 m/s [3]

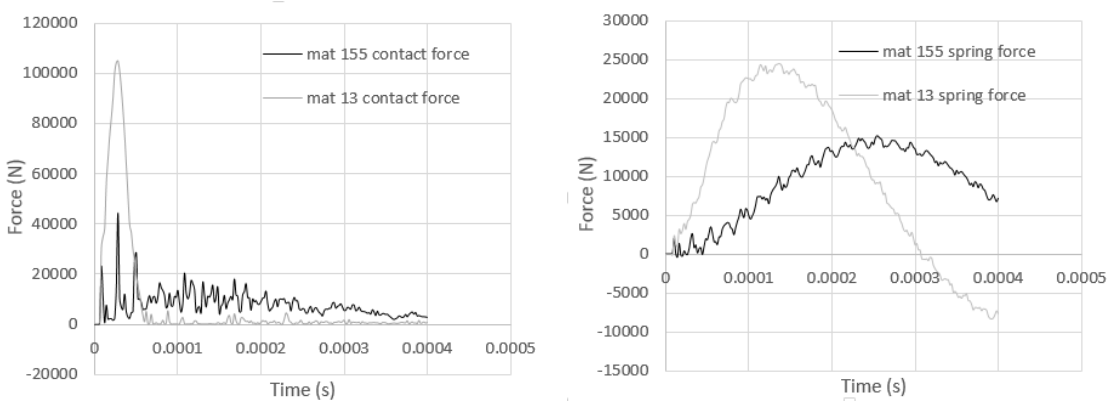

Contact force Inner spring force

Figure 5-17 Simulation of Kim's test (95.4m/s)

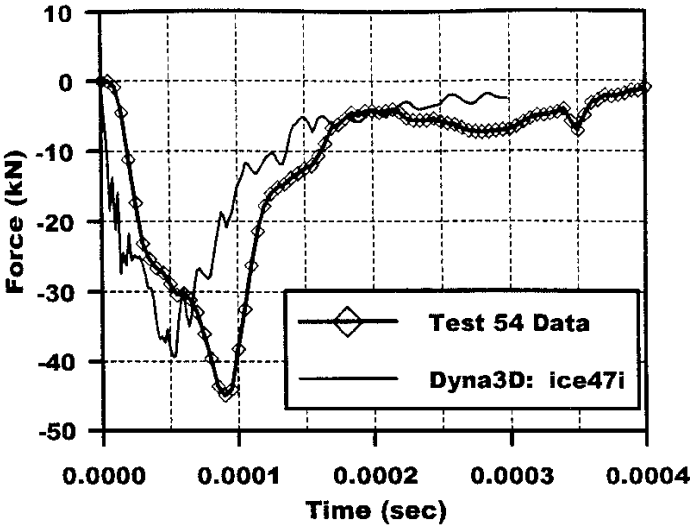

Figure 5-18 Test at 126 m/s [3]

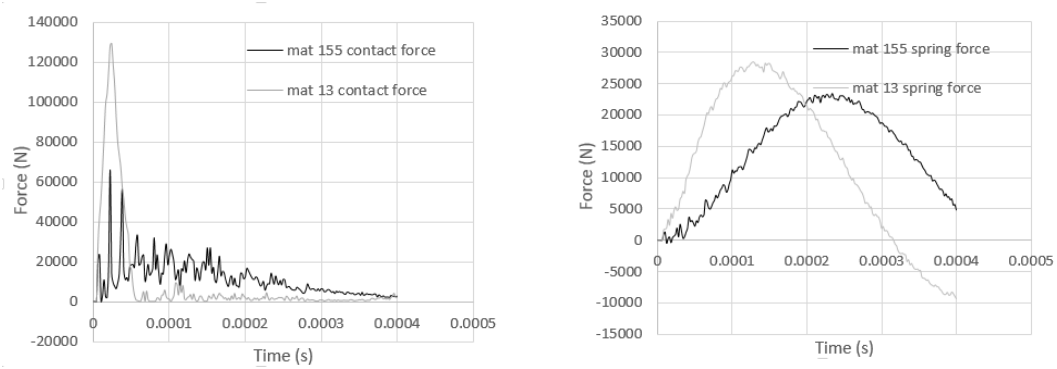

Contact force Inner spring force

Figure 5-19 Simulation of Kim's test (126m/s)

Table 5-11 The predicted peak force and error of Kim's test

	Test force	contact force				spring force			
		155		13		155		13	
		value	error	value	error	value	error	value	error
	73.5m/s								
Peak force (KN)	15	24.3	0.62	85.	4.7	9.6	-0.36	21.9	-0.46
Time (ms)	0.1	0.03		0.03		0.2		0.1	
	95.4m/s								
peak force (KN)	27	44.1	0.63	104.9	2.8	15.2	-0.44	24.5	-0.1
time (ms)	0.1	0.03		0.03		0.2		0.1	
	126m/s								
peak force (KN)	45	65.8	0.46	129.2	1.87	23.4	-0.49	28.5	-0.37
time (ms)	0.8	0.02		0.02		0.2		0.1	

From the simulation result, it can be found that the spring force can represent the force history more accurately than the contact force. The curve shape of the impact force history using MAT 155 is significantly better than using MAT 13. But

when it comes to the peak force the accuracy of MAT 155 drops, even worse than MAT 13.

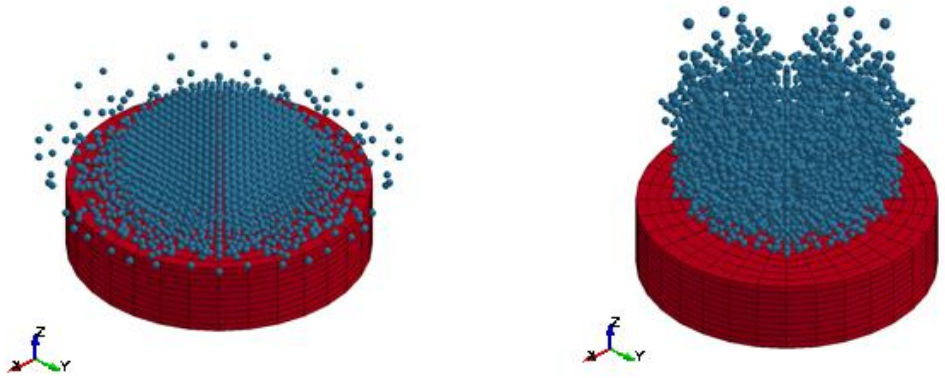

MAT 155 MAT 13

Figure 5-20 Kinematic behaviour of the projectile in Kim's test

Figure 5-20 shows the kinematic behaviour of the projectile of MAT 155 and MAT 13. It has been shown clearly that there is no fluid-like stage in the MAT 13 test however there is a clear fluid-like stage in the MAT 155 test.

5.3.3 Pereira cylinder ice test

In the Pereira cylinder ice test the force history was measured by the force measurement transducer [7] as well which is simplified as a load cell shown in Figure 4-4 by Carney [4]. The target model based on the simplification is shown in Figure 5-21. The parameter of the plate and spring are listed in Table5-6, 7.

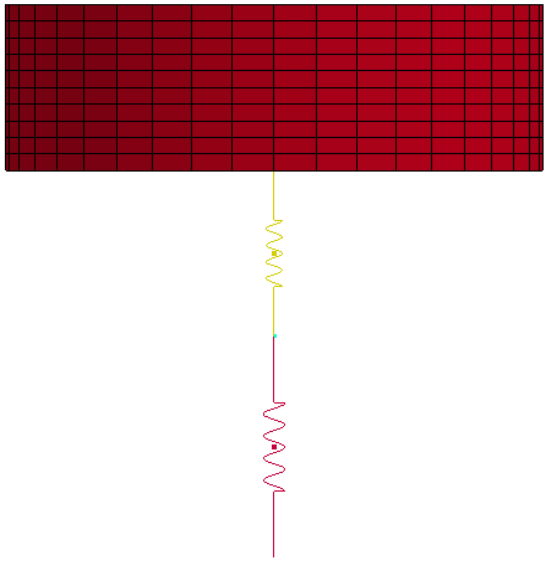

Figure 5-21 Load cell set up

Table 5-12 Parameters used in modelling the force measurement transducer of Pereira's test - Plate

Parameter	value
Density	4400kg/m^3
Young's modulus	109GPa
Poisson's ratio	0.34
Diameter	62.5mm
Thickness	20.0mm

Table 5-13 Parameter used in modelling the force measurement transducer in Pereira's test - Spring

Parameter	Spring		
	Transducer	Bolt	Back-up
Elastic stiffness	7GPa	2.347GPa	0.8231GPa
Length	20mm	20.0mm	25.4

A test focusing on particle resolution study was conducted first, aiming at finding the most appropriate resolution through altering the mesh density within the ice projectile. The impact velocity applied in this test is 91m/s.

As the SPH method was adopted, the distance between each particle must be taken into consideration. Since the projectile used in Pereira's test is an ice cylinder whose diameter and length are 17.5mm and 42.2mm respectively, in order to make sure the distance of each particle is similar in all directions, the ratio of particles' number along the length and across the diameter need to be equal to the ratio of the diameter and length of the projectile. Thus 4 configurations were employed in this study shown in Table 5-14.

Table 5-14 Mesh Density configurations

name	D15L36	D20L48	D30L72	D40L96
Number of elements across diameter	15	20	30	40
Number of elements along length	36	48	72	96

The simulation results are shown in Figure 5-23. When increasing the SPH particle's density, peak force will decrease slightly. The maximum difference among these four tests is the first trough force represented by 2 in Figure 5-23. The gap between D15L36 and D40L96 is 3.8%. A convergence was witnessed between D30L72 and D40L96. In this case, D30L72 was chosen to conduct the different impact speed test.

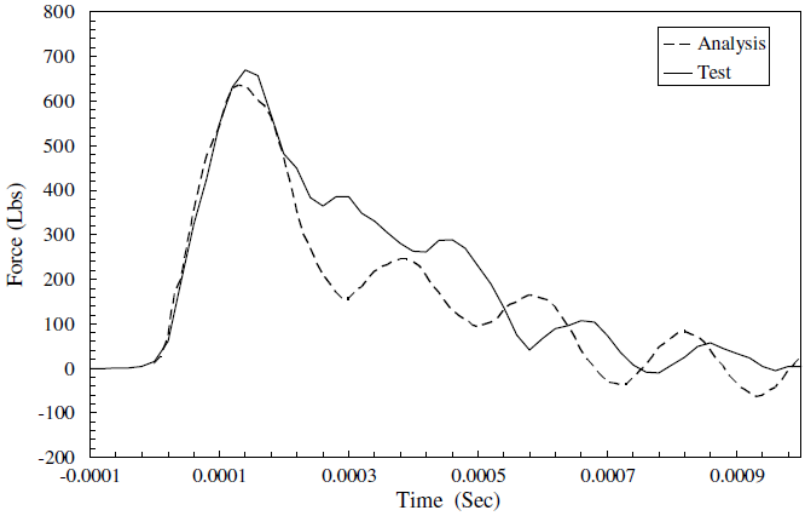

Figure 5-22 Pereira's test data (91m/s) [7]

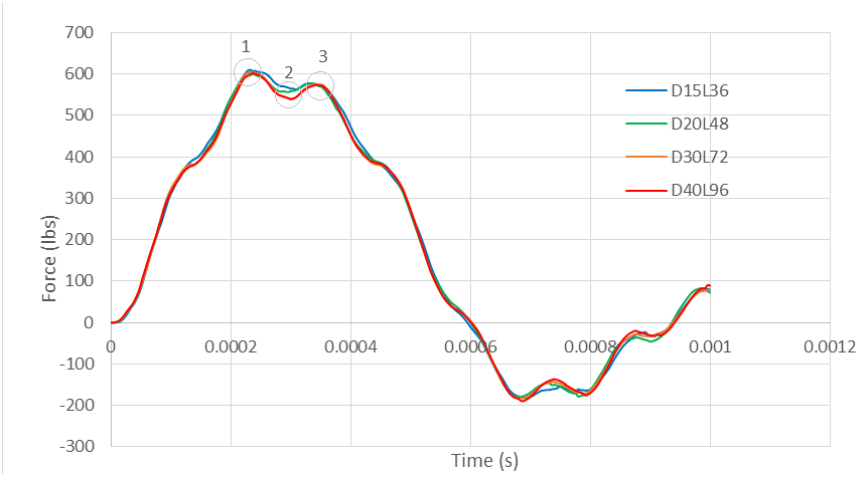

Figure 5-23 Mesh density study results of Pereira's test model (91m/s)

Table 5-15 Comparison of resolution test results

	max peak force(1)		first trough force(2)		following peak force(3)	
	time(ms)	force(lbs)	time(s)	force(lbs)	time(s)	force(lbs)
D15L36	0.23	610.5	0.3	562.9	0.3	577.8
D20L48	0.23	602.3	0.3	556.7	0.3	577.9
D30L72	0.23	605.6	0.3	540.7	0.3	576.2
D40L96	0.23	602.3	0.3	539.2	0.3	573.9

Three tests with different velocities were simulated. The test results and simulation results are shown in Figure 5-25. The comparison of peak force and duration is shown in Table 5-10.

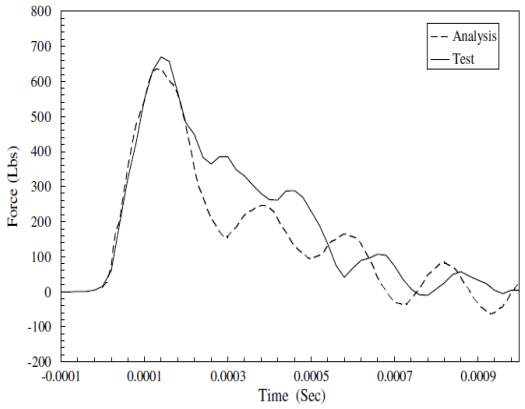

Test result (91m/s) [4]

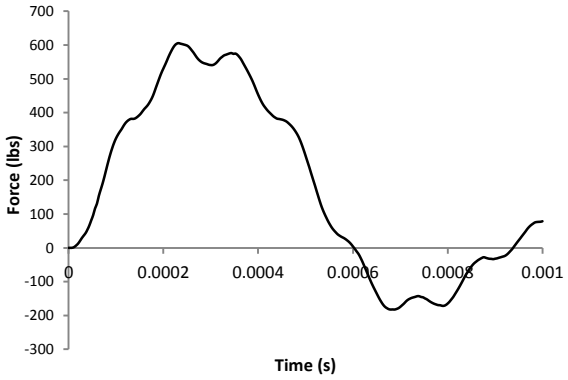

Current test result (91m/s)

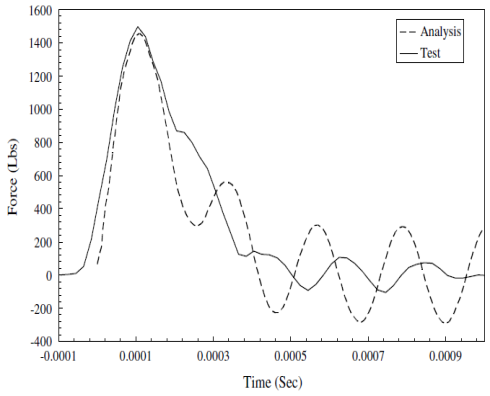

Test result (152.4m/s) [4]

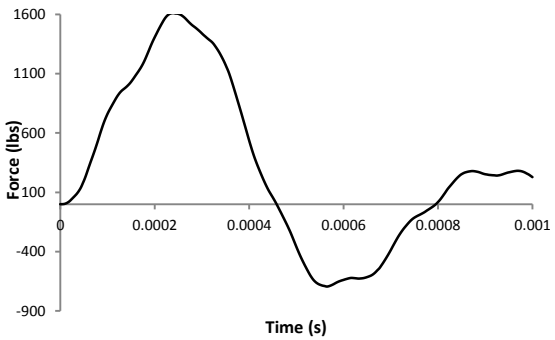

Current test result (152.4m/s)

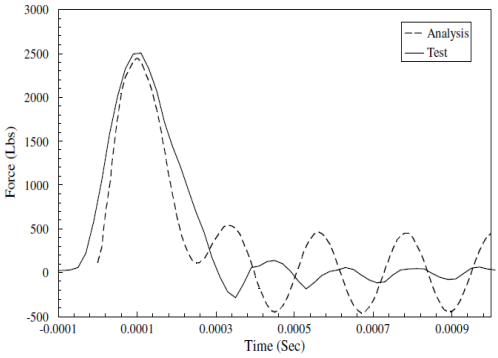

Test result (213.3m/s) [4]

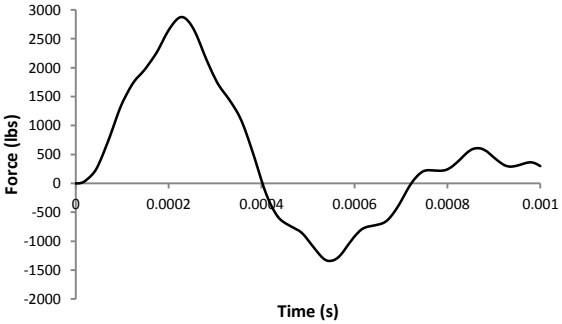

Current test result (213.36m/s)

Figure 5-24 Test result and Carney's FE model result

Table 5-16 Comparison of different speed simulation results

		91m/s		152.4m/s		213.36m/s	
		test	simulation	test	simulation	test	simulation
peak force	value (lbs)	680	606	1480	1610	2500	2875
	time(ms)	0.16	0.23	0.16	0.24	0.18	0.228
error		11%		8.7%		15%	

duration of the first pulse (ms)	0.6	0.604	0.48	0.46	0.4	0.4
error	0.67%		5%		0%	

From the comparison between simulation results and test results under different velocities, it can be inferred that when the velocity is 91.44m/s, the simulated peak force is nearly 50 Lbs (200N) lower than the test result, but as the velocity increases, the simulated peak force increases more severely than the test result. When the velocities are 152.4m/s and 213.36m/s, the simulation peak force is higher than the test result by about 450N and 2000N respectively. The duration of the first fluctuation is shorter as the velocity is increasing, but the simulation result is still longer than the test about 0.0001s.

But in general the predicted impact force is close enough to the test result whether on magnitude or the duration. It can be noticed that the error of the predicted peak force is within 15%, and the error of the duration is within 5%. This study illustrates that MAT 155 can reflect the ice cylinder projectile well.

5.3.4 Conclusion

After simulating these three different test problems, it can be concluded that:

1. MAT 13 is not suitable for the ice material. Firstly, even though in Kim's simulation MAT 13 can output a successful force history, the truth is that there is a huge force concentration on the centre of the target which is nearly the same as the total impact force and as a result there is nearly no impact force on the rest of the surface away from the centre. The impact force is represented by the contact force, whose inter face is the ice projectile surface and the whole front face of the plate. This is the reason why MAT 13 is successful in modelling Kim's test whose output is the total impact force, but failed in the modelling pressure recording test whose output is the centre area contact force. Secondly, MAT 13 cannot reflect the ice behaviour visually; this can be seen in Figure 5-20 which shows that the projectile totally crashed in the early stage of impact.

2. MAT 155 is suitable for modelling ice. Firstly, the test result from the simulation of the pressure recording test illustrates that there is no impact force concentration existing and there is a distribution of the contact force on the contact surface which is closer to the reality. Secondly, MAT 155 can reflect the ice behaviour visually; this can be seen in figure 5-20 which illustrates that the material goes in to a fluid-like stage after failure.
3. Through modelling Kim's sphere test, it can be found that for force measurement transducer tests it is more accurate to simplify the force measurement transducer to a load cell and the inner force within the spring can represent the impact force more accurately than the contact force.
4. By modelling two shapes of projectile, it is found that MAT 155 is very successful in modelling a cylindrical projectile but not that successful in modelling a spherical projectile. From the study in Chapter 3.1, this maybe because there is a loading condition dependence existing in ice, but MAT 155 did not take this feature into consideration.

5.4 Conclusion

Through theoretical investigation and the numerical investigation, it can be concluded that:

1. The ideal ice model needs to be equipped with at least 4 features – strain rate dependence, pressure dependence, nonlinear relationship between the pressure and volumetric strain, fluid-like post-failure behaviour.
2. As the most perfect ice material model Carney's model still has its limitations. It has not been equipped with pressure dependence. Although when simulating cylindrical projectiles MAT 155 is very successful, but the accuracy of the MAT 155 will drop. This maybe because the ice also has a loading condition dependence feature which MAT 155 is not been equipped with.
3. Although Pernas-Sánchez proposed a way to take the pressure dependence into consideration – using the Drucker-Prager yield criteria in the constitutive model. The material cohesion used in the Drucker-Prager yield criteria ought to be the current yield stress rather than a constant

value which was employed in his constitutive. Furthermore, the relationship between the pressure and the volumetric strain ought to be nonlinear rather than a linear which is employed in his constitutive model.

4. Reviewing the ice features and the current ice material model, the way of modifying the current ice material model can be proposed. Since MAT 155 is considered to be the most suitable ice material model, and three important features of ice have not been included in it – pressure dependence, loading condition dependence, temperature dependence - people can modify MAT 155 by adding these features to MAT 155. Since there is no test data available on the temperature dependence aspect and on the loading condition dependence, these two features are very hard to be added into Carney's model. But since the Drucker-Prager yield criteria is a very mature yield criteria which is widely used in the concrete and soil constitutive material models, it is possible to add this criteria into MAT 155 to realize the pressure dependence of MAT 155.

6 USER MODEL OF ICE BEHAVIOUR

This user defined material model accomplished a part of MAT 155 which has been used by Carney in his paper.

6.1 The UMAT building method

Based on the research of MAT155, five special features have been reflected in the MAT155, they are nonlinear bulk response, different performance in tension and compression, bilinear hardening mode, pressure based failure mode and strain rate dependent feature.

UMAT41 is a simple elastic user defined material model routine provided by the LS-Dyna company[9]. The reproduction of the MAT155 is started from this simple elastic model and adds those features reflected by MAT155 one by one. For accuracy consideration, the updated material model needs to be verified through conducting a specific test when a new feature is added into this material model.

The parameters needing to be defined in MAT 155 are shown in Table 6-1, parameters related to the ice will be studied in detail in this chapter, to figure out exactly the functions and how to reproduce those functions in UMAT.

Table 6-1 MAT 155 parameter

Being discussed (Y/N)	Variable	Description
N	RO	Mass density
N	E	Young's modulus
N	PR	Poisson's ratio
N (is not set in ice material parameter published by NASA)	C	Strain rate parameter
N (is not set in ice material parameter published by NASA)	P	Strain rate parameter
N	TDEL	Minimum time step size for element deletion

(is not set in ice material parameter published by NASA)		
Y (discussed in 6.2.3)	LCIDC	Load curve ID defining yield stress-effective plastic strain in compression
Y (discussed in 6.2.3)	LCIDT	Load curve ID defining yield stress-effective plastic strain in tension
Y (discussed in 6.2.5)	LCSRC	Strain rate scaling effect on yield stress in compression
N (is not set in ice material parameter published by NASA)	LCSRT	Strain rate scaling effect on yield stress in tension
N (is not set in ice material parameter published by NASA)	SRFLAG	Formulation for rate effects
Y (discussed in 6.2.3)	PC	Compressive mean stress at which the yield stress follows the load curve LCIDC. If the pressure falls between PC and PT a weighted average of the two load curves is used.
Y (discussed in 6.2.3)	PT	Tensile mean stress at which the yield stress follows the load curve LCIDC.
Y (discussed in 6.2.4)	PCUTC	Pressure cut-off in compression. When the pressure cut-off is reached the deviatoric stress tensor is set to zero. The compressive pressure is not, however limited to PCUTC. Scaled by the rate effects.
Y (discussed in 6.2.4)	PCUTT	Pressure cut-off in tension. When the pressure cut-off is reached the deviatoric stress tensor and the tensile pressure is set to zero. Scaled by the rate effects.
Y (discussed in 6.2.1)	PCUTF	Pressure cut-off flag.

N (is not set in ice material parameter published by NASA)	SCALEP	Scale factor applied to the yield stress after the pressure cut-off is reached.
N (is not set in ice material parameter published by NASA)	SCALEE	Scale factor applied to the yield stress after the strain exceeds the failure strain set by FAIL.
N (is not set in ice material parameter published by NASA)	K	Optional bulk modulus for the viscoelastic material.
N (is not set in ice material parameter published by NASA)	GI	Optional shear relaxation modulus for the ith term.
N (is not set in ice material parameter published by NASA)	BETAI	Optional shear decay constant for the ith term

The whole process of this reproduction study is shown in Figure 6-1. Because the pressure of the element will influence the stress state, and the pressure was controlled by the equation of state, so the compaction feature is the first feature chosen to be added into the basic elastic model. The pressure cut-off is the next feature that needed to be added into the material model by noticing that the pressure was also limited by the pressure cut-off value both in tension and compression. From Carney's article, it has been found that Von-Mises yield criteria and bilinear hardening model was adopted in the MAT155, so the third feature needed to be added in is the plasticity feature. The failure criteria of the MAT155 is for the pressure, when the pressure is over the compressive pressure cut off value or the pressure is less than the failure pressure in tension the material will fail, so the forth feature chosen to be added into the material model is pressure based failure criteria. The final feature is strain rate dependence. Strain rate will influence the yield stress of the material. These updates are all verified by single element tests, and judged by specific test data. After the whole

material model was completed, the reproduced MAT155 was tested through simulating the Nanjing ice impact experiment.

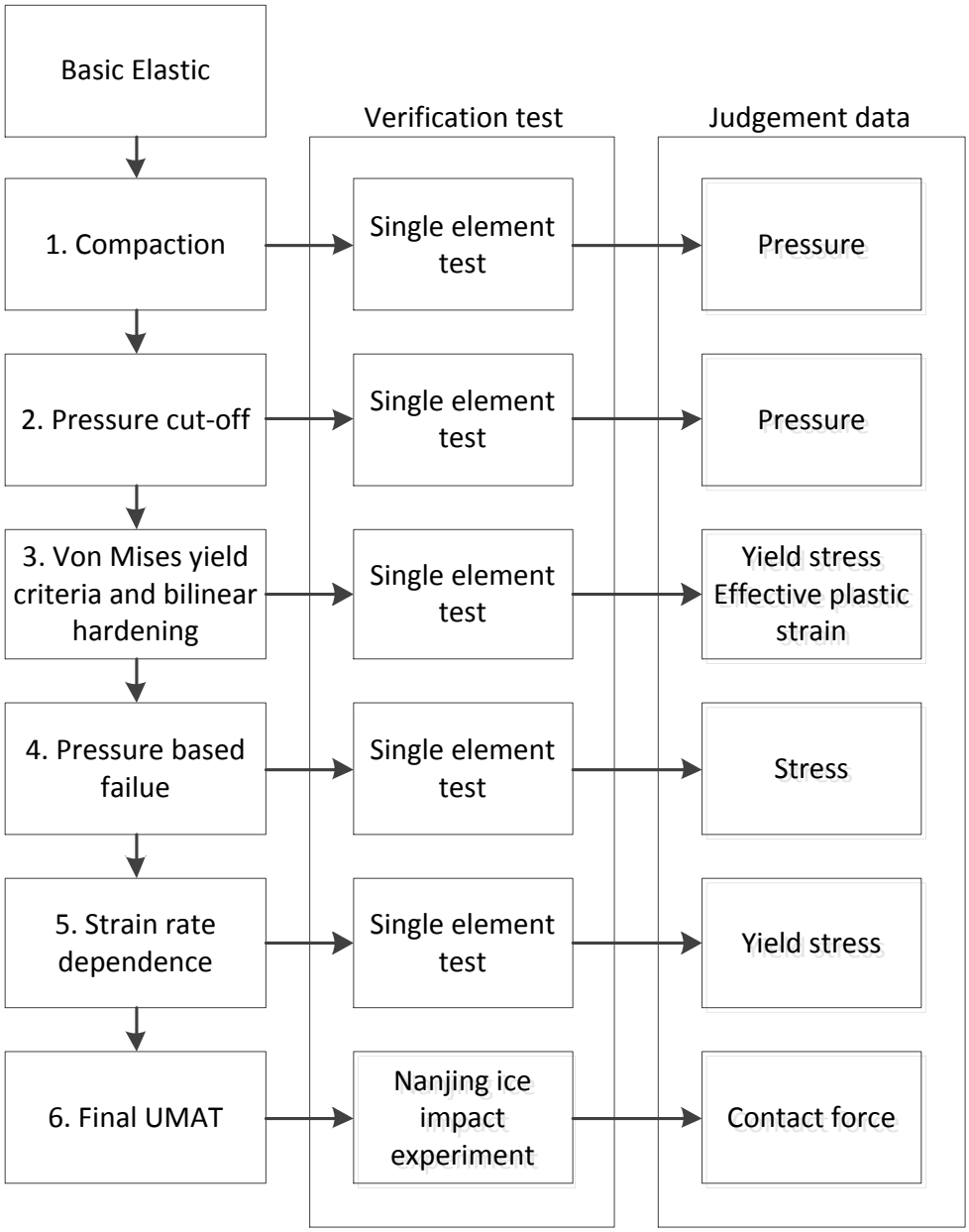

Figure 6-1 Reproduction Process

Throughout the whole reproduction process, there are several default settings of the MAT 155 parameters in the check test need to be noted.

1. Because the strain rate dependence is considered at the end of the process, so in the first 4 stages of the reproduction process the load curve represented by LCSRC is set as a curve with a constant ordinate which is

equal to 1. This default can neglect the influence of the strain rate dependence.

2. In stage 1, the PCUTF is set active.
3. In stage 2, the PCUTF is set inactive.
4. The test result are all noted positive in compression and negative in tension.

6.2 Building and verification procedure

6.2.1 EOS controlled compaction feature

In order to apply the compaction feature into the simply elastic user defined material UMAT 41, a test aimed at figuring out how the EOS works was conducted. In this test both the MAT 155 and the NULL material model with *EOS_TABULATED_COMPACTION card were tested under tension-compression looping loading. In MAT 155 the pressure cut-off flag was turned on. The parameters used in the MAT 155 and MAT NULL are shown in Table 6-2.

Table 6-2 Eos test input parameters

Parameter	MAT 155	MAT NULL
Density	897.6kg/m^3	897.6kg/m^3
Young's modulus	9.31GPa	9.31GPa
Poisson's ratio	0.33	0.33
Pressure cut-off in tension	-0.433MPa	-0.433MPa
Pressure cut-off in compression	4.93MPa	-

It is needs to be noted that the MAT NULL only defined the pressure cut-off in tension, and did not define the pressure cut-off in compression. Both of the pressure cut-off in tension and compression are defined in the MAT 155. The pressure cut-off flag set as inactive in this test. The rate dependent curve in MAT 155 is set as a curve with the y value equal to 1 constantly. The loading condition and the test result are shown in Figure 6-2.

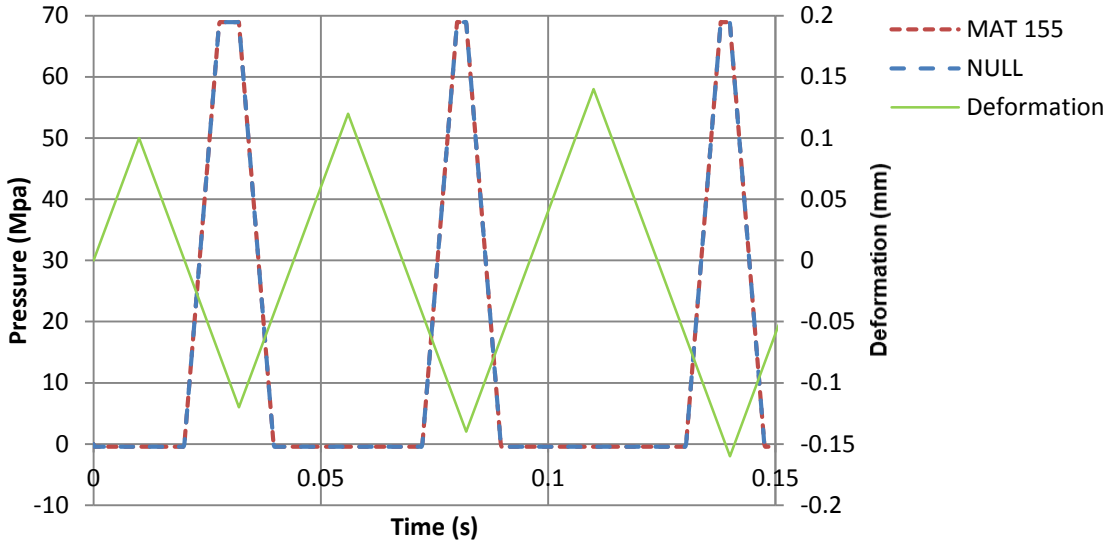

Figure 6-2 EOS test under inactive pressure cut-off flag

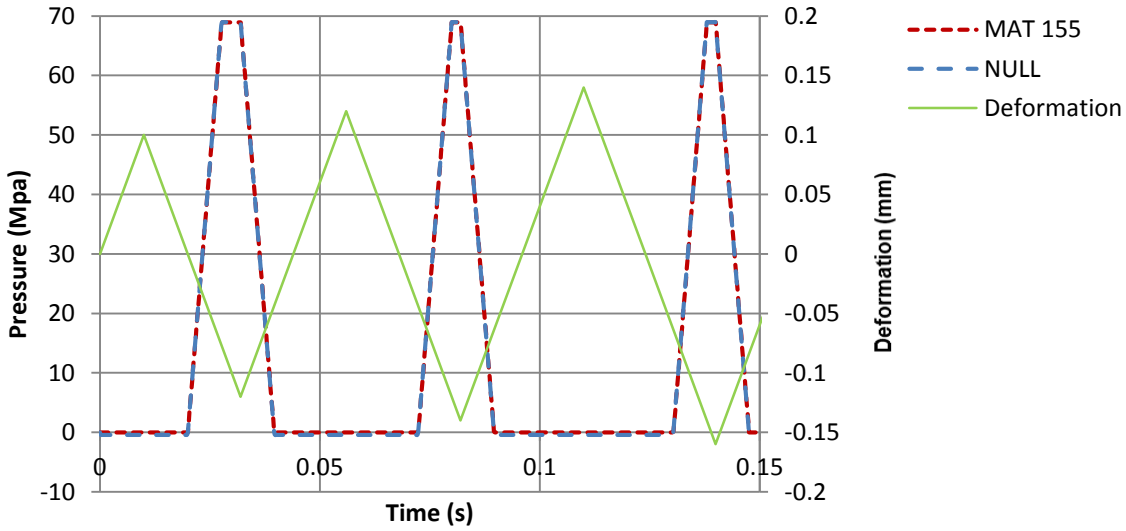

Figure 6-3 EOS test under active pressure cut-off flag

From the result of this test it can be observed that under the same loading condition and when the pressure cut-off flag was inactive, the performance of these two material models are the same which reflects that the pressure of the element will be controlled by the EOS during the whole loading process under the situation that the pressure cut-off flag is inactive. When the pressure cut-off flag is active, the tensile pressure will limited to 0. This phenomena shows that if

the pressure cut-off flag is active the pressure of the compressive loading will controlled by the EOS, and the pressure of the tensile loading will set be as 0.

Because there is no information about the ice performance under tensile loading, to simplify the reproduction, under the following EOS study the pressure cut-off flag is active. The pressure cut-off value and the pressure cut-off flag will be researched in Chapter 6.2.2.

The EOS adopted in MAT 155 is illustrated in Figure 6-4. The Pressure is defined by[9];4]

$$P = C(\boldsymbol{\varepsilon_v}) + \gamma T(\boldsymbol{\varepsilon_v})E \qquad \textbf{Equation 6-1}$$

But MAT 155 defines γ as 0. Thus during loading the pressure is linear with volumetric strain. If unloading occurs, the slope of the unloading will be corresponding to the bulk modulus at the peak volumetric strain and the reloading will be along the same path as the unloading path.

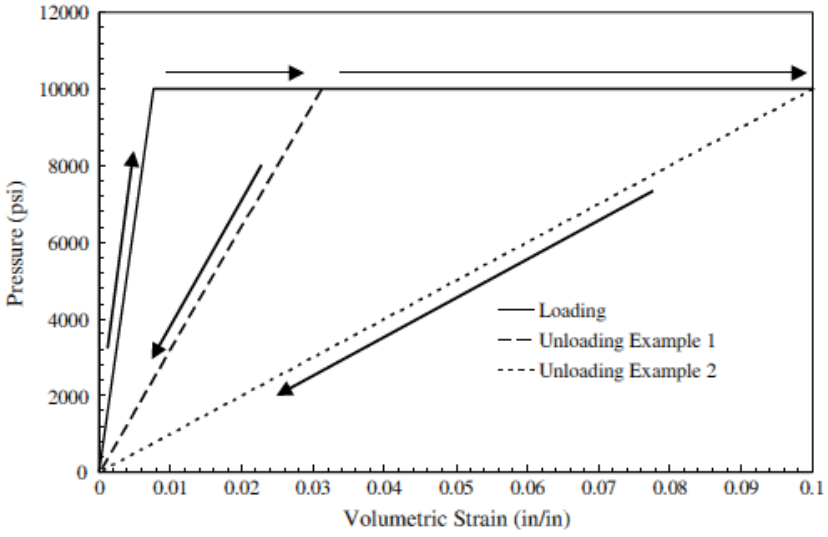

Figure 6-4 Equation of state adopted in MAT 155 [4]

After understanding the function of the EOS, how to reflect the EOS can be taken in to consideration. The original constitutive relationship between the strain and stress reflected in UMAT 41 is in the form [9]

$$\boldsymbol{\sigma} = 2G\boldsymbol{\varepsilon_d} - k\boldsymbol{\varepsilon_v} \qquad \textbf{Equation 6-2}$$

Where $\boldsymbol{\sigma}$ is the stress tensor, G is sheer modulus, $\boldsymbol{\varepsilon_d}$ is the deviatoric strain tensor, k is bulk modulus, $\boldsymbol{\varepsilon_v}$ is the volumetric strain tensor.

For the consideration of the compaction and the plasticity feature, the volumetric part and the deviatoric part of the stress tensor need to be calculated separately, and then the stress tensor can be calculated by combining these two parts. Rewrite Equation 6-2 in the form [40]

$$\boldsymbol{\sigma} = \boldsymbol{S} + \boldsymbol{P} \qquad \textbf{Equation 6-3}$$

Where $\boldsymbol{S}$ is the deviatoric stress tensor, $\boldsymbol{P}$ is the volumetric stress tensor. In this research the pressure is in the form [9]

$$P = -k'\varepsilon_v \qquad \textbf{Equation 6-4}$$

Where k' is the current bulk modulus changing with the loading and unloading history and current volumetric strain.

In this research, the EOS feature is reflected by a curve defined in the pre-processing, which will be called by the user defined material (UMAT) during calculation. The bulk modulus is calculated from dividing the maximum pressure throughout the whole loading and unloading history by the maximum volumetric strain. Noticing that the maximum pressure is corresponding to the maximum volumetric strain, so only the maximum volumetric strain needs to be stored and the maximum pressure can be acquired by calling the EOS curve.

The process to calculate the pressure can be shown as Figure 6-5. Where ev is the volumetric increment, hsv(ev) is the current volumetric strain, hsv(max) is the maximum volumetric strain historically, k' is the need bulk modulus, Pmax is the ordinate value of the EOS curve.

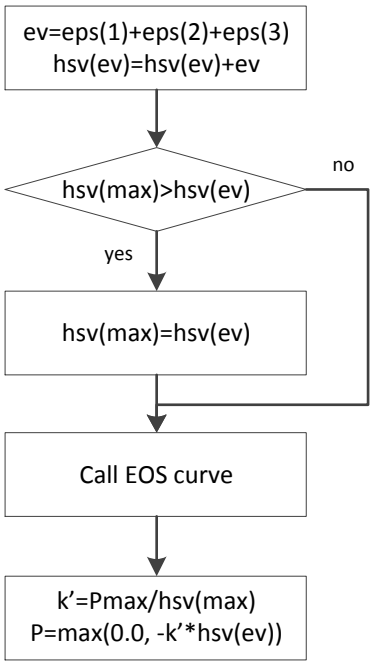

Figure 6-5 Pressure calculating procedure

This elastic with EOS UMAT was verified through running a single element with compression – tension looping loading test. The check test was conducted by using MAT 155 to run the same single element test. The feature of the single element and the loading condition is shown in Figure 6-6. Fixing the bottom 4 nodes and adding deformation load on the top 4 nodes.

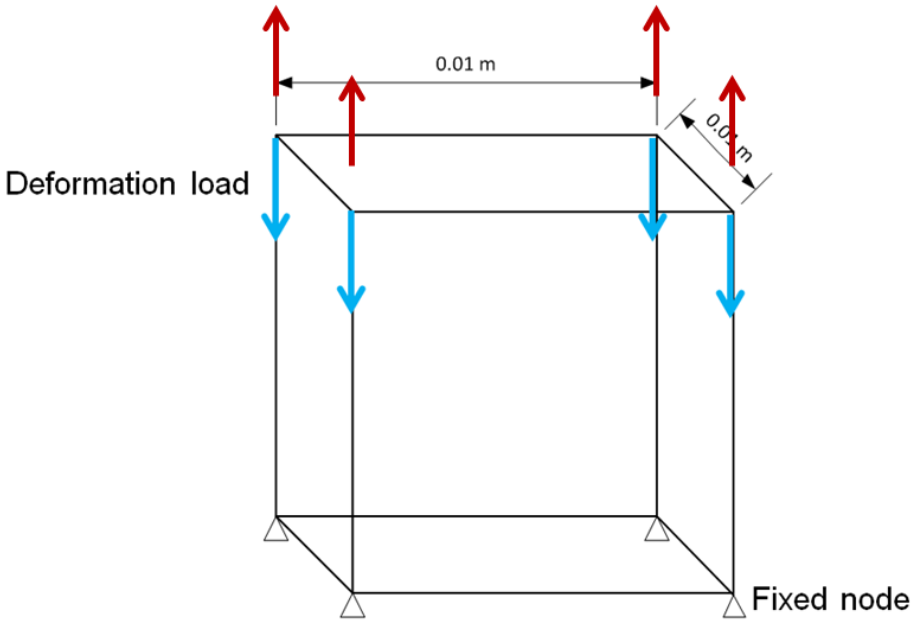

Figure 6-6 Single element test of compressive-tensile looping loading

Parameters set in this test are the same as Table 6-2.

The comparison of the results from these two tests is shown in Figure 6-7. The bulk modulus of each loading stage is shown in Table 6-3.

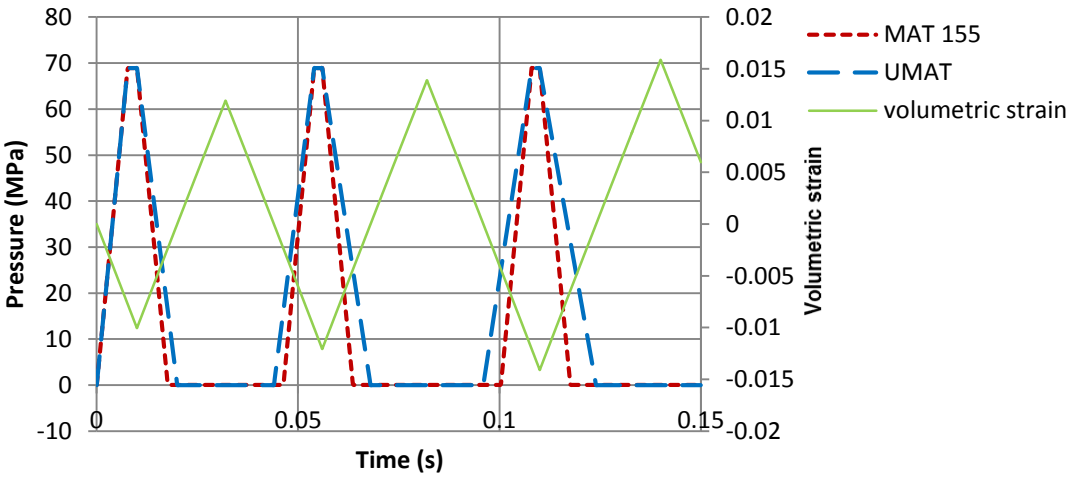

Figure 6-7 EOS reproduction test

From Figure 6-7, it has been found that the bulk modulus of these two material is not the same in each loading-unloading stage, and the bulk modulus of MAT 155 seems has not been changed through the loading-unloading looping. Thus plot the bulk modulus of MAT 155 and UMAT in table 6-3Table 6-3 Bulk modulus of each loading stage

	MAT 155	MAT NULL
1	9.0GPa	9.0GPa
2	-9.0GPa	-7.0GPa
3	9.0GPa	7.0GPa
4	-9.0GPa	-6.0GPa
5	9.0GPa	6.0GPa
6	-9.0GPa	-4.5GPa

From table 6-3 it can be seen proved that the bulk modulus of MAT 155 is remain the same which is not accordance with the description file of MAT 155 [4]. To make the UMAT perform the same as MAT 155, an EOS calculation choice constant was set in the UMAT. If cm(6) – the number 6th parameter needs to be typed in when setting up the material is set as 2, the UMAT will calculate the pressure as the Carney, just using a constant bulk modulus, and the pressure would be in the form of

$$P = -k\varepsilon_v \qquad \textbf{Equation 6-5}$$

Where k is the constant bulk modulus of the material. If this parameter is set as 1 the UMAT will calculate the pressure as Carney described in his article. The optional EOS pressure calculation process is reflected in Figure 6-8.

The same single element test is conducted to verify whether this optional EOS UMAT can perform as MAT 155. The test result is shown in Figure 6-9.

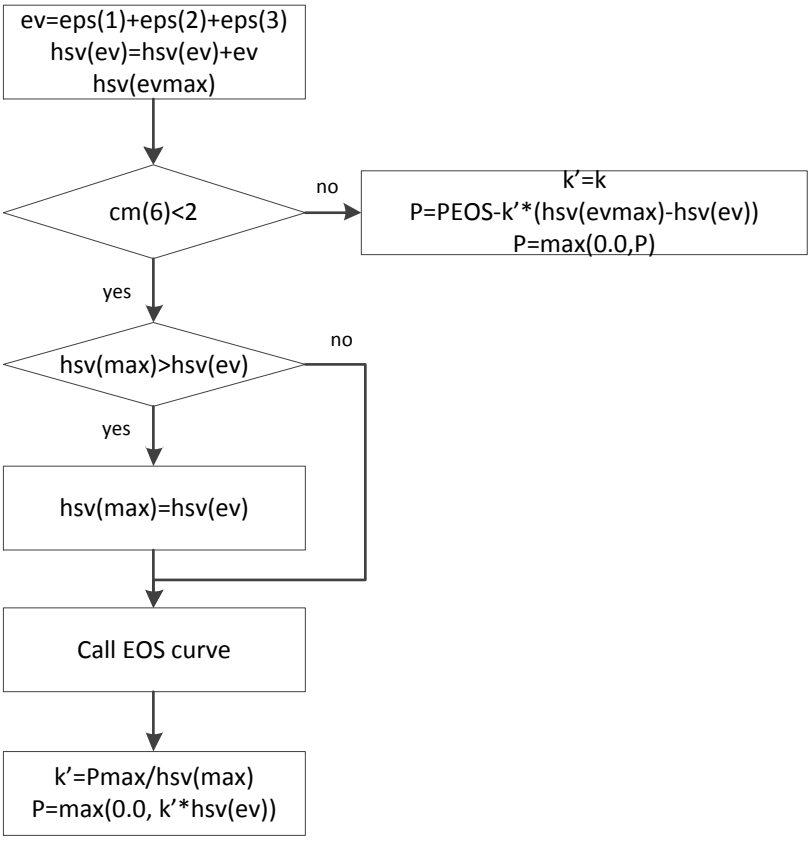

Figure 6-8 Optional EOS pressure calculation process

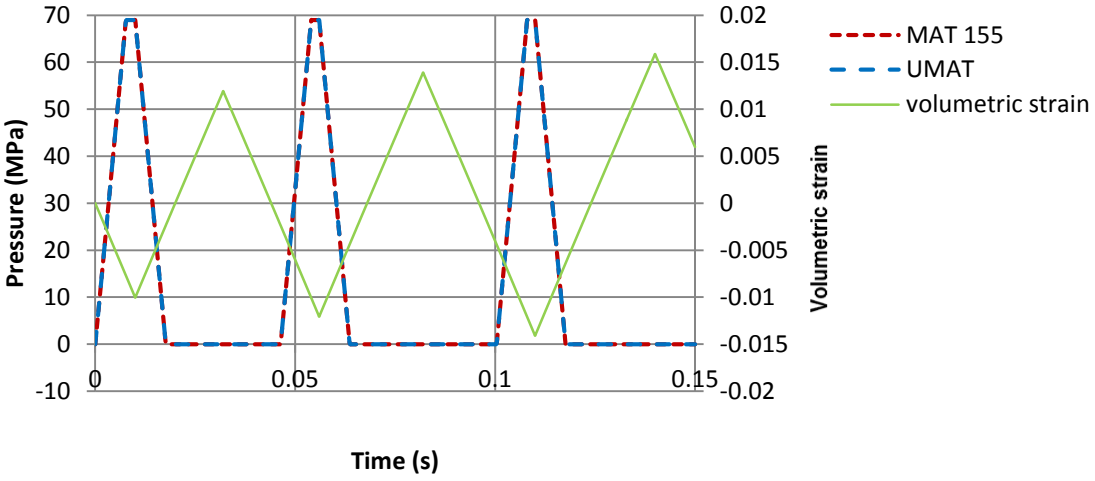

Figure 6-9 EOS reproduction updating test

The result of the UMAT test shows a great agreement with the result of the MAT 155 test. This test demonstrates that the EOS feature defined in the UMAT can

perform the same as the MAT 155, which means the first stage of the reproduction is accomplished.

6.2.2 Pressure cut-off

In Carney's article, the author mentioned that the pressure cut-off limits the magnitude of the pressure in tension. Thus a series of tests focusing on the function of pressure cut-off was conducted.

In order to simplify the EOS test, the pressure cut-off flag has been studied in Chapter 6.2.1. The results of the tests shown in Figure 6-2 and 6-3 which demonstrated that under tensile loading the pressure would be set as the PCUTT when the PCUTF is inactive, and would be set as 0 when PCUTF is active. Under compressive loading the pressure will only be controlled by the EOS and will not be influenced by the PCUTC. This test also demonstrates that the PCUTT will work only when the PCUTF is inactive.

The aim of this stage is to investigate the influence of the PCUTC and PCUTT value on the pressure. So firstly, the PCUTF is set inactive in the check test. The influence of the PCUTC value on the pressure is tested firstly and the influence of the PCUTT value on the pressure is tested secondly.

The tensile-compressive looping loading test on the same single element which is shown in Figure 6-6 using MAT 155 is conducted to investigate the influence of PCUTT on the pressure. The parameters set in the MAT 155 are listed in Table 6-4. Three different values of PCUTT are tested.

Table 6-4 Parameters setting in PCUTT influence investigating test

Parameter	1	2	3
Density	897.6kg/m^3	897.6kg/m^3	897.6kg/m^3
Young's modulus	9.31GPa	9.31GPa	9.31GPa
Poisson's ratio	0.33	0.33	0.33
Pressure cut-off in tension	-0.433MPa	-4.33MPa	-43.3MPa
Pressure cut-off in compression	4.93MPa	4.93MPa	4.93MPa

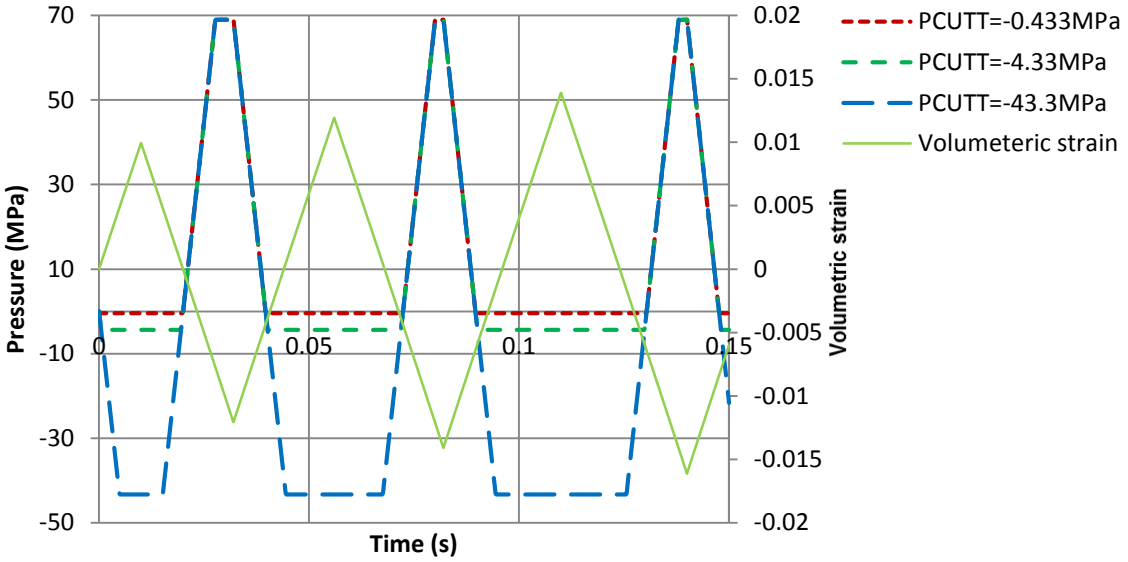

Figure 6-10 Pressure of PCUTT influence investigating test

The pressure of the tests is shown in Figure 6-10. It can be inferred that the pressure in tension would descend to the PCUTT value until the loading changes to compression.

The same single element tensile-compressive looping loading is conducted to find the influence of the PCUTC on the pressure. Three different PCUTC values are tested. The parameters are listed in Table 6-5.

Table 6-5 Parameters setting in PCUTC influence investigating test

Parameter	1	2	3
Density	897.6kg/m^3	897.6kg/m^3	897.6kg/m^3
Young's modulus	9.31GPa	9.31GPa	9.31GPa
Poisson's ratio	0.33	0.33	0.33
Pressure cut-off in tension	0	0	0
Pressure cut-off in compression	4.93MPa	49.3MPa	493MPa

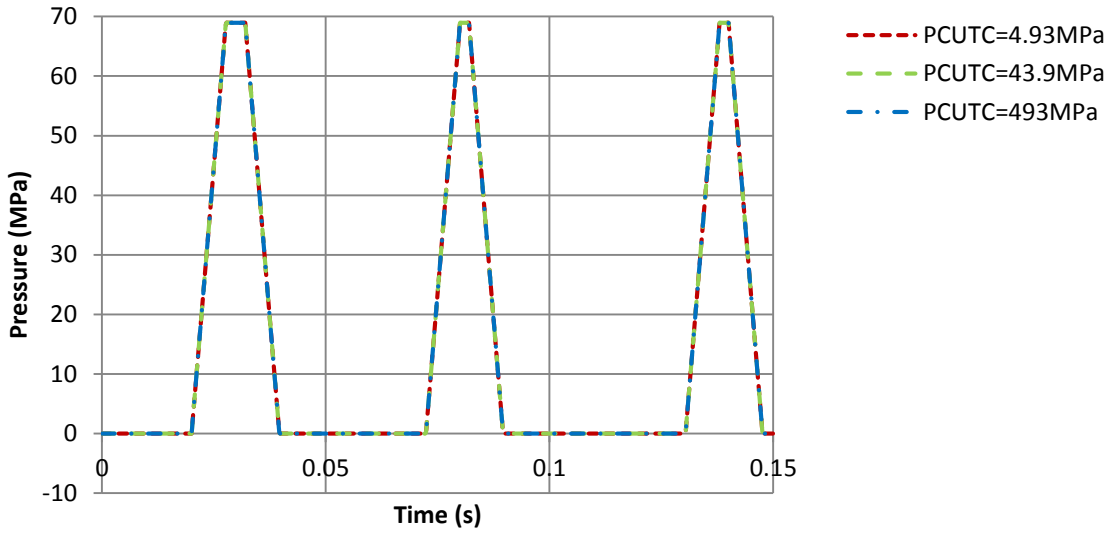

Figure 6-11 Pressure of PCUTC influence investigating test

The pressure of PCUTC influence investigating test is shown in Figure 6-11, from this it can be found that the value of PCUTC will not influence the pressure in the element.

From the result of these two tests, it can be found that, only the PCUTT will influence the pressure of the element under tensile loading, the PCUTC will not influence the pressure of the element whether in tension or compression.

From the pressure cut-off study, it can be concluded that the pressure of MAT 155 will be defined by three factors; they are EOS, PCUTT and PCUTF. The compressive pressure is calculated by the EOS and the pressure in tension will set as 0 when the PCUTF is active and will descend to the PCUTT when the PCUTF is inactive.

Thus the pressure calculation routine can be updated by adding an optional pressure cut-off flag and can be represented as shown in Figure 6-12.

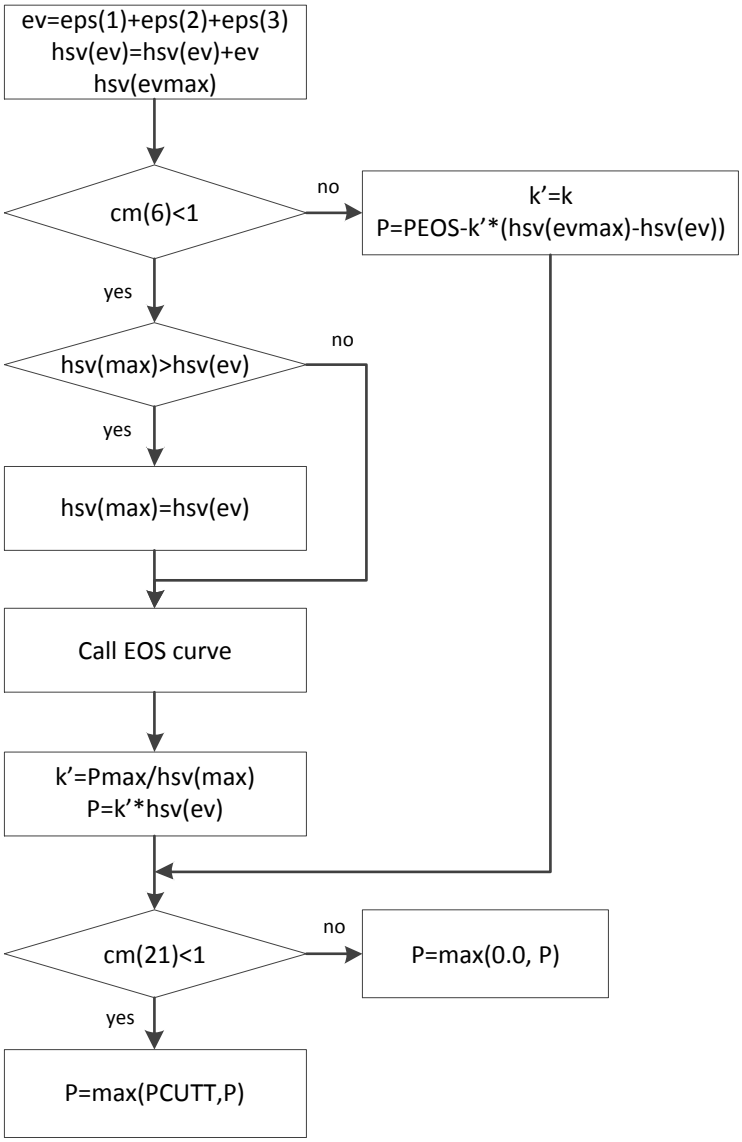

Figure 6-12 Pressure influenced by pressure cut-off calculation process

cm(21) is the 21th parameter need to be defined in the UMAT card. The UMAT will correspond to MAT 155 with an active PCUTF when cm(21) is set as 1, and will correspond to MAT 155 with an inactive PCUTF when cm(21) is set as 0.

The same single element test was conducted to verify this updated UMAT to see whether the pressure can be calculated correctly. The parameter set in UMAT is listed in Table 6-6. The test result is shown in Figure 6-13

Table 6-6 EOS and pressure cut-off controlled pressure UMAT verification test parameters

	1	2
Density	897.6kg/m^3	897.6kg/m^3
Young's modulus	9.31GPa	9.31GPa
Poisson's ratio	0.33	0.33
Pressure cut-off in tension	-493Mpa	-493Mpa
Pressure cut-off in compression	4.93MPa	4.93MPa
cm(6)	0	0
cm(21)	0	1

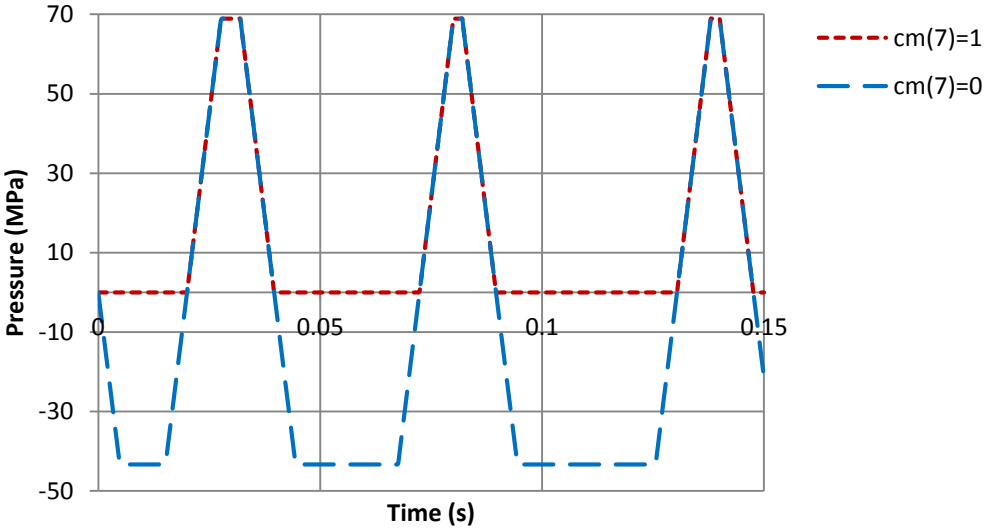

Figure 6-13 EOS and pressure cut-off controlled pressure UMAT verification test

Comparing Figure 6-13 with Figures 6-10 and 6-11, it can be found that the UMAT can perform the same as MAT 155.

With the pressure cut-off influence addition, the pressure calculation routine is finished.

6.2.3 Von-Mises yield criteria and bilinear hardening

MAT 155 has different properties in tension and compression which was reflected in the different initial yield stress value. This property was achieved through implying two load curves within MAT 155. The load curve was chosen according to the element of pressure. If the pressure is greater than PC the yield stress will follow LCIDC, which means the yield stress can be obtained directly by calling LCIDC, which can be described as:

$$\sigma_y = C(LCIDC)|_{\varepsilon^p} \qquad \textbf{Equation 6-6}$$

Where $C(LCIDC)$ is the load curve defining yield stress versus effective plastic strain in compression.

If the pressure is less than PT the yield stress will follow LCIDT, which means the yield stress will be given directly by calling LCIDT, which can be described as:

$$\sigma_y = C(LCIDT)|_{\varepsilon^p} \qquad \textbf{Equation 6-7}$$

Where $C(LCIDT)$ is the load curve defining yield stress versus effective plastic strain in tension.

If the pressure falls between PC and PT a weighted average of the two load curves is used. Which can be described as

$$\sigma_y = \sigma_{y0} + h\varepsilon^p \qquad \textbf{Equation 6-8}$$

$$\sigma_{y0} = \left(\sigma_f^C - \left(\sigma_f^C - \sigma_f^T\right)\left(\frac{P_C - P}{P_C - P_T}\right)\right) \qquad \textbf{Equation 6-9}$$

Where σ_y is yield stress, σ_f^C is initial compressive flow stress, σ_f^T is initial tensile flow stress, P_C is compressive mean stress, P_T is tensile mean stress, h is plastic tangent modulus, ε^p is the effective plastic strain.

From Equations 6-7, 6-8 and 6-9 it can be found that once the effective plastic strain is known, the yield stress can be obtained directly. The main target in this stage is calculating the current effective plastic strain.

According to the radial return algorithm, the effective plastic strain increment can be represented as:

$$d\varepsilon^p = \frac{\sigma_e - {\sigma_f}^{(1)}}{3g + h} \qquad \textbf{Equation 6-10}$$

Where σ_e is the current trial stress, which can be represented as:

$$\sigma_e = \sqrt{3J_2} \qquad \textbf{Equation 6-11}$$

Where J_2 is the second deviatoric invariant.

${\sigma_f}^{(1)}$ is the last time step yield stress, which has already known in the current time step. Thus the current plastic can be represented as:

$$\varepsilon^p = \varepsilon^p + d\varepsilon^p \qquad \textbf{Equation 6-12}$$

Thus the calculation process of the yield stress can be described as shown in Figure 6-14.

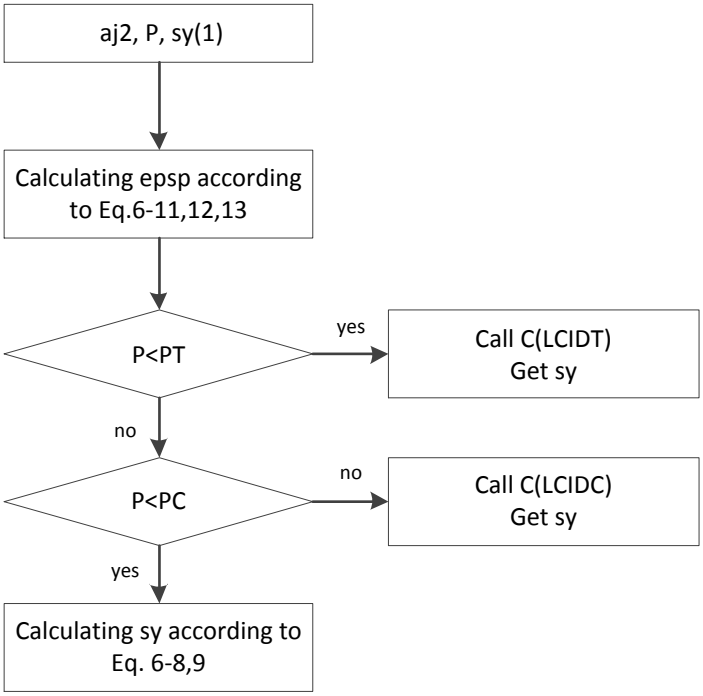

Figure 6-14 Yield stress calculation process

Where aj2 is the current trial stress, P is current pressure, sy(1) is yield stress of last time step, epsp is effective plastic strain, PT is tensile mean stress; PC is

compressive mean stress; C(LCIDT) is the curve defining yield stress versus effective plastic strain in compression; C(LCIDT) is the curve defining yield stress versus effective plastic strain in tension; sy is the current yield stress.

Apply both of the updated UMAT and MAT 155 to the same single element with tensile-compressive looping loading test to see whether it performs the same as the MAT 155. The single element is the same as above. The parameters used in this test are listed in Table 6-7, and the test result is shown in Figure 6-15.

Table 6-7 With Von-Mises yield criteria UMAT verification test parameters

	UMAT	MAT 155
Density	897.6kg/m^3	897.6kg/m^3
Young's modulus	9.31GPa	9.31GPa
Poisson's ratio	0.33	0.33
Pressure cut-off in tension	-0.433Mpa	-0.433Mpa
Pressure cut-off in compression	4.93MPa	4.93MPa
PC	6894.75Pa	6894.75Pa
PT	-6894.75Pa	-6894.75Pa
cm(6)	0	-
cm(21)/PCUTF	1	active

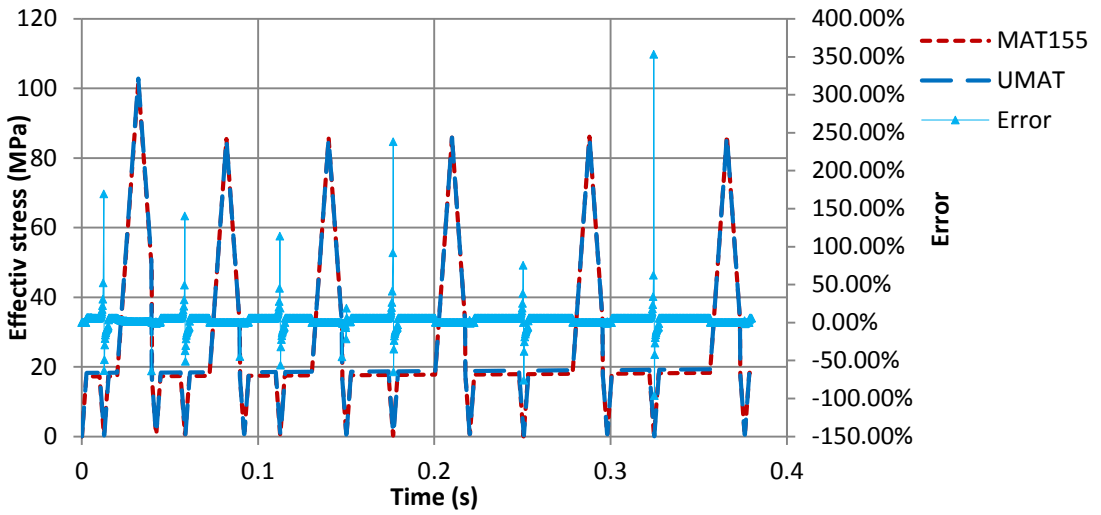

Figure 6-15 Effective stress of the UMAT which has Von-Mises yield criteria verification test

From this tensile-compressive loading test, it can be found that the effective stress of the UMAT and the MAT 155 are nearly the same, the error is within 20%, and a huge error can only happen when the changing of loading condition taken place. So this error is within the permitted level.

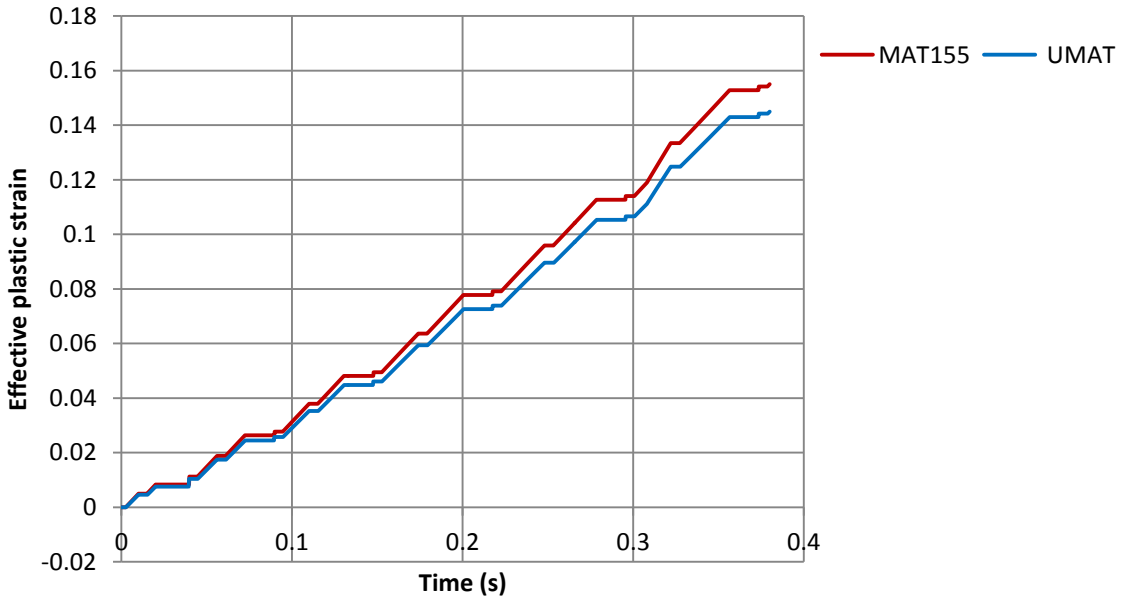

Figure 6-16 Effective plastic strain of the UMAT which has Von-Mises yield criteria verification test

From the effective plastic strain result, it can be found that the trends of the effective plastic strain are the same. The difference between the result of UMAT and MAT 155 is only restricted to the magnitude. The gap within the first 3 loops is very small, and considering that the ice is a brittle material, there cannot be many loops during the impact event. Thus this test result can be accepted.

6.2.4 Pressure based failure mode

The pressure based failure in MAT 155 is described as when the pressure cut-off in compression is reached the deviatoric stress tensor will be set as 0, and the compressive pressure will be limited to the PCUTC; when the pressure cut-off in tension is reached both of the deviatoric stress tensor and the tensile pressure will be set as 0. This stress updating process is shown in Figure 6-17.

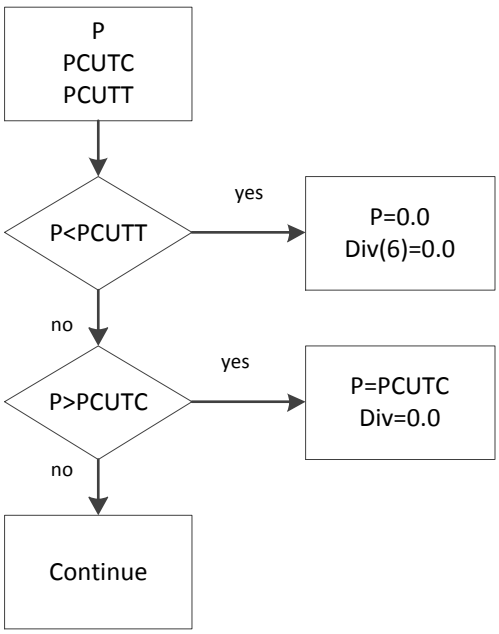

Figure 6-17 Stress updating process according to pressure based failure mode

A single element under tensile-compressive looping loading test is conducted to verify the stress updating is correct or not.

The parameters used in this verification test are listed in Table 6-8.

Table 6-8 Parameters used in UMAT with failure verification test

	UMAT	MAT 155

Density	897.6kg/m^3	897.6kg/m^3
Young's modulus	9.31GPa	9.31GPa
Poisson's ratio	0.33	0.33
Pressure cut-off in tension	-0.433Mpa	-0.433Mpa
Pressure cut-off in compression	4.93MPa	4.93MPa
PC	6894.75Pa	6894.75Pa
PT	-6894.75Pa	-6894.75Pa
cm(6)	0	-
cm(21)/PCUTF	1	active

The result of this test is shown in Figures 6-18 and 6-19.

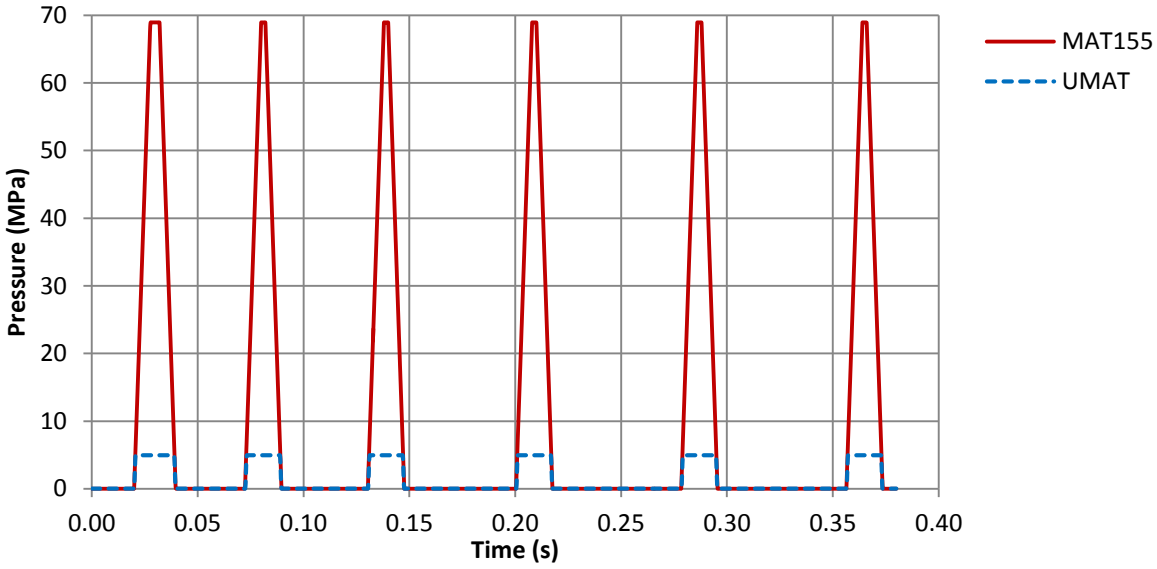

Figure 6-18 Pressure of the UMAT with failure verification test

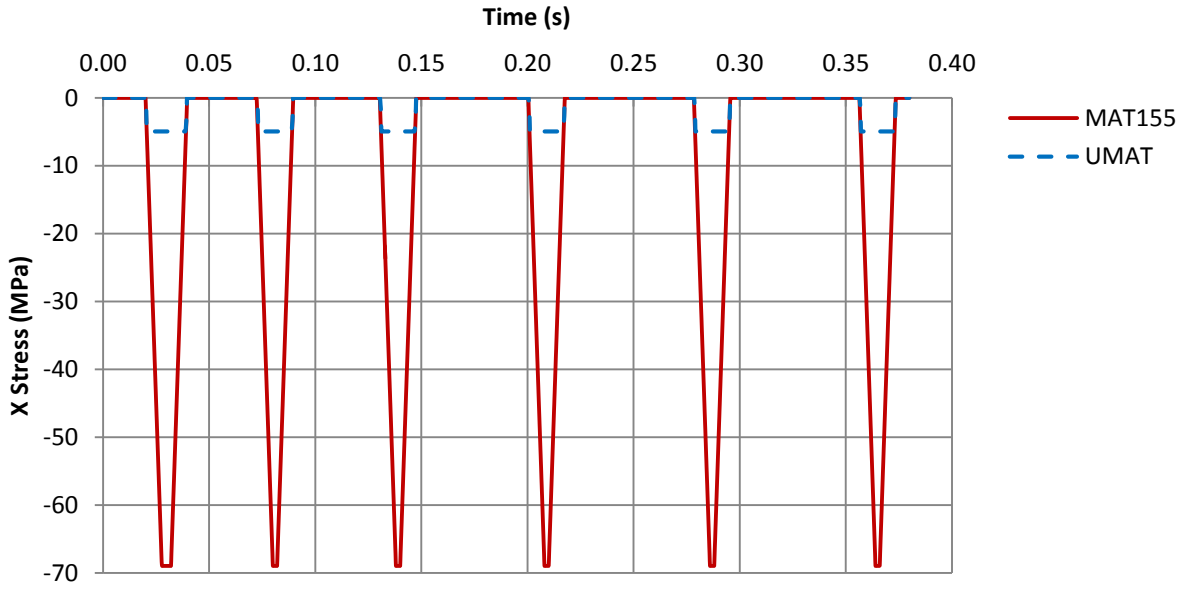

Figure 6-19 X axil stress of the UMAT with failure verification test

From the test result, it can be found that the MAT 155 did not perform as has been described. The pressure has not been limited to PCUTC when the pressure reaches this value, and only the tensile pressure is set to 0. To realize what the MAT 155 performs, cm(22) is set as the failure mode flag which describes the modification introduced by UMAT. When cm(22) set as 1, the UMAT will perform as the MAT 155 being described, and when cm(22) is set as 0, the UMAT will perform as the MAT 155 real performance. Thus the stress updating process of the pressure based failure mode is changed as shown in Figure 6-20.

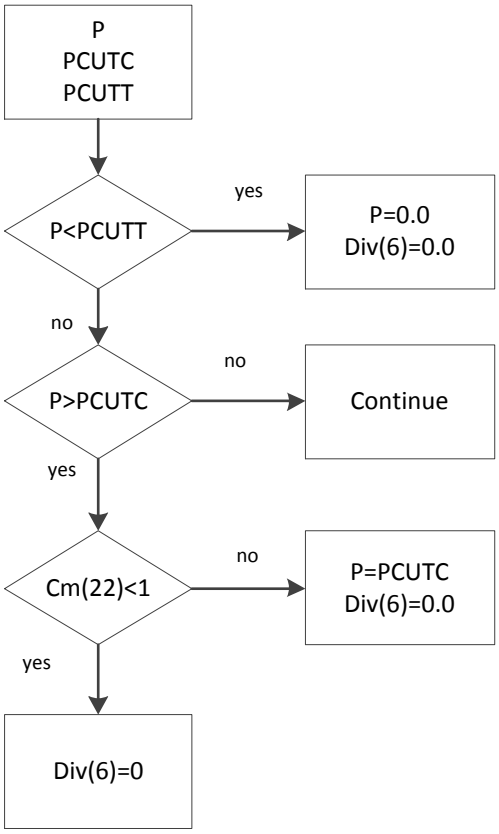

Figure 6-20 Stress updating process performs the same as MAT 155

The same verification test is conducted, and the cm(22) set as 0. The result is shown in Figures 6-21 and 6-22.

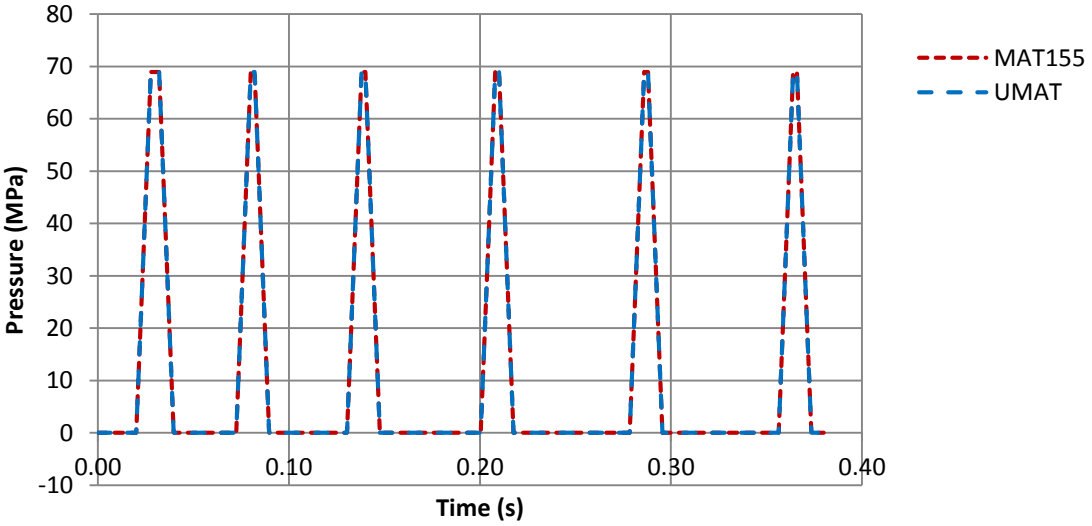

Figure 6-21 Pressure of the UMAT with MAT 155 failure mode verification test

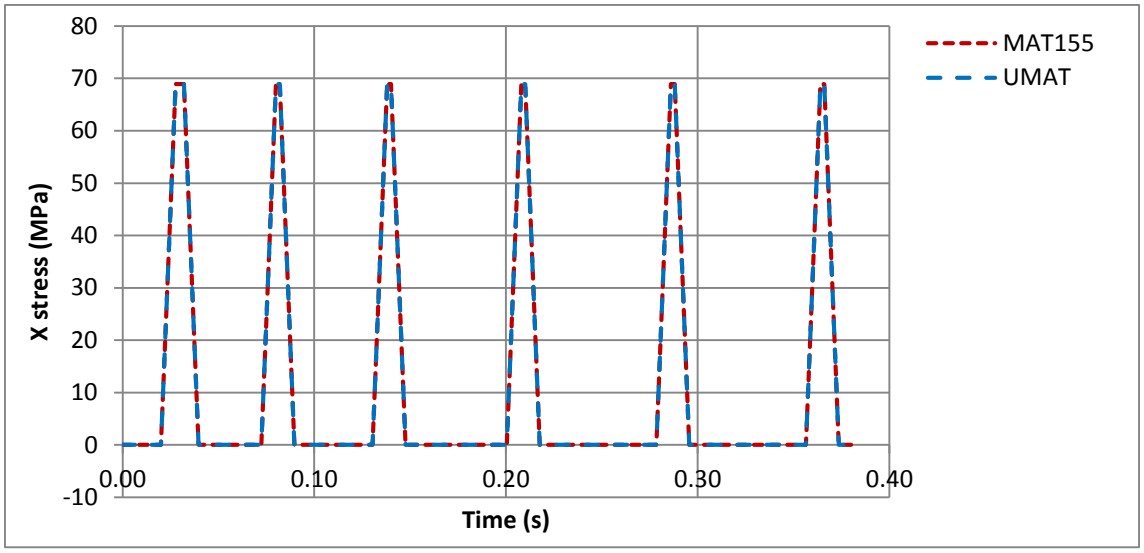

Figure 6-22 X axial stress of the UMAT with MAT 155 failure mode verification test

According to the result from the verification test, it can be proved that the updated failure mode can perform the same as MAT 155. Thus the Failure feature addition is completed.

6.2.5 Strain rate dependence

The last feature need to be added into the UMAT is the strain rate dependence. In MAT155 tabular data is used to define the dependence of the flow stress on the strain rate and pressure.

After carefully checking the MAT 155, it is found that not only the flow stress will influenced by the strain rate but also the pressure cut-off will be influenced by the strain rate. But based on the research in Chapter 6.2.1, 6.2.2 and 6.2.4, it has been proved that the value of the pressure cut-off will not influence the stress state of the element, so in this study it will only be necessary to consider the strain rate dependence of the yield stress.

The flow stress can be represented as the Equation 6-13 [4]

$$\sigma_y = \hat{s}(|\boldsymbol{D}|, P) \cdot \sigma_y{}' \qquad \textbf{Equation 6-13}$$

There are two components of the scaling function, which are two tabular functions of the strain rate at a specified tensile pressure and compressive pressure respectively [4].

$$\hat{s}(|\boldsymbol{D}|, P) = f\hat{c}_C(|\boldsymbol{D}|) + (1 - f) \cdot \hat{c}_C(|\boldsymbol{D}|) \quad \textbf{Equation 6-14}$$

$$f = \min(1, \max(0, \frac{P - P_T}{P_C - P_T})) \quad \textbf{Equation 6-15}$$

But due to no tensile tabular function data, so the scaling function was simplified as Equation 6-16.

$$\hat{s}(|\boldsymbol{D}|, P) = \hat{c}_C(|\boldsymbol{D}|) \quad \textbf{Equation 6-16}$$

The input strain sensitivity of ice is shown in Table 6-9 and Figure 6-23.

Table 6-9 Strain sensitivity of ice [4]

Strain rate	rate
1	1
10	1.2566
100	1.5132
200	1.59044
300	1.63562
400	1.66768
500	1.69255
600	1.71287
700	1.73005
800	1.74493
900	1.75805
1000	1.76979
1100	1.78042
1500	1.81498
10000	2.02639

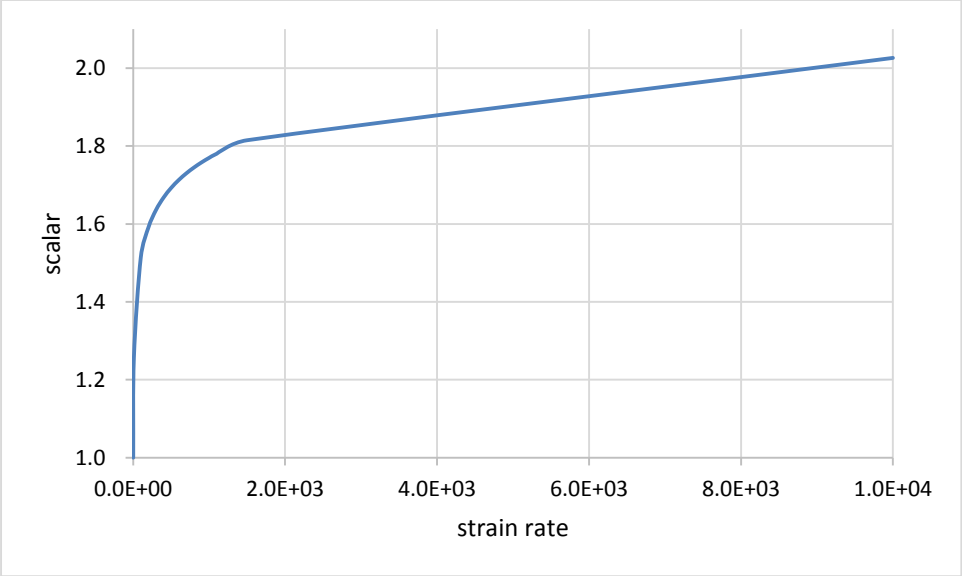

Figure 6-23 Strain sensitivity of ice

The strain rate can be calculated as the effective strain increment divided by the current time step.

$$\dot{\varepsilon^p} = \frac{d\varepsilon^p}{tt} \qquad \textbf{Equation 6-17}$$

Where tt is the current time step. The yield stress updating process can be described as shown in Figure 6-24.

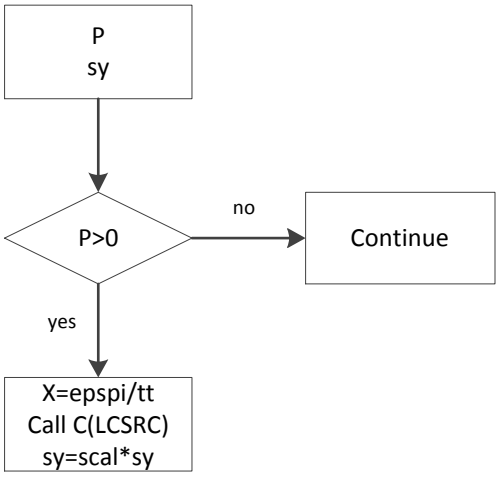

Figure 6-24 Yield stress updating according to the strain rate

Apply this UMAT to the Nanjing ice impact test to verify the reproduction of MAT 155. The test basic condition has been described detailed in Chapter 5.3.1. The test results are shown in Figures 6-25 and 6-26.

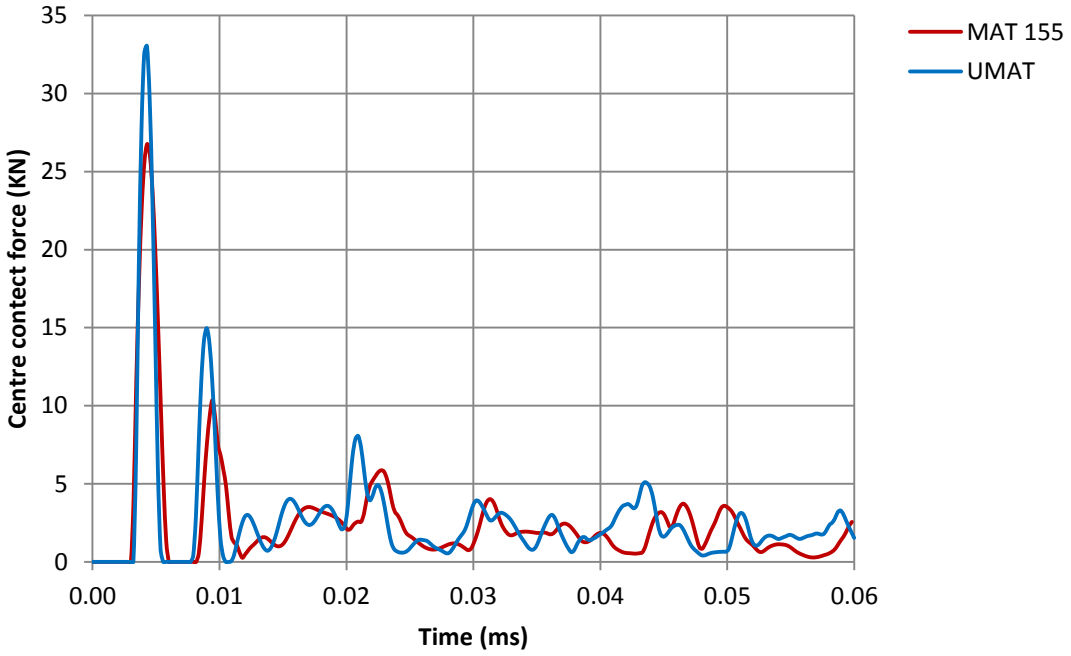

Figure 6-25 Contact force of the UMAT verification test

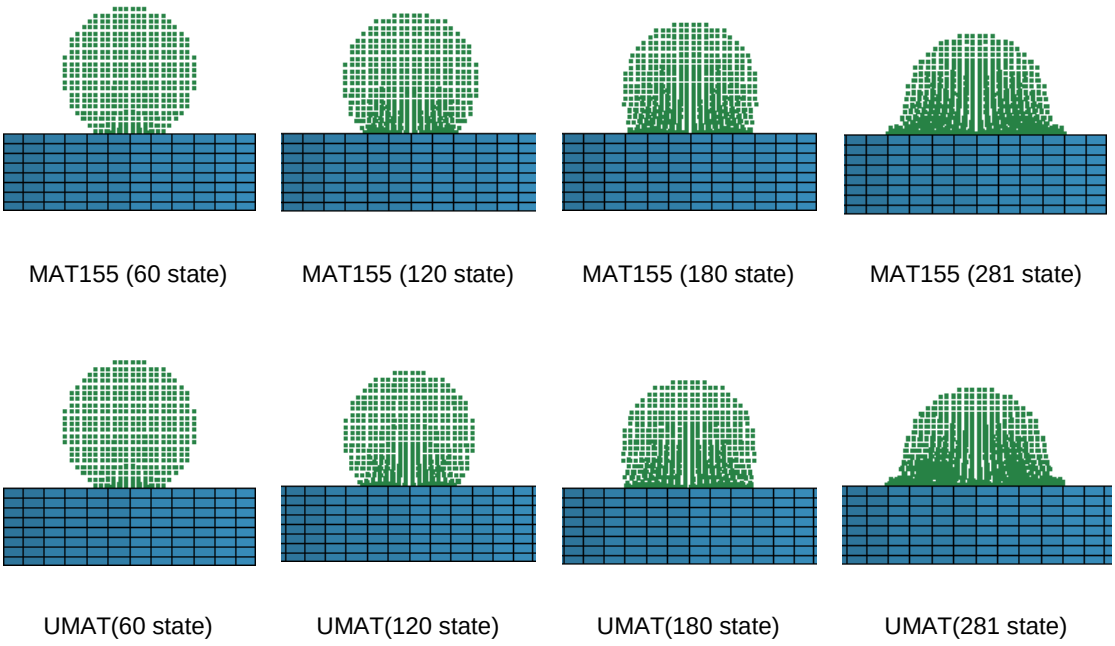

Figure 6-26 Impact process of the UMAT verification test

From the test result, it can be found that the impact process of the UMAT test matches very well with the MAT 155 test. The shape of the contact force curve of the UMAT test is accordant to the result of the MAT 155. Although there are some differences in the peak force with an error of 22%, the whole result is within the tolerance range. The UMAT has demonstrated that it can reflect the features of the MAT 155, thus the reproduction of the MAT 155 is accomplished.

6.3 Conclusion

A user defined ice material which performs the same as the MAT 155 is developed through five steps. Within the developing approach two differences between the MAT 155 as described and the real performance of MAT 155 are found.

7 USER MODEL FOR ICE BEHAVIOUR WITH PRESSURE DEPENDENT FEATURE

7.1 Modifying method

From the early study of the ice material model, it has been found that there are three aspects of the MAT155 that can be modified; they are pressure dependence, temperature dependence and the loading condition dependence.

Currently the temperature dependence has not been studied well and consequently there is a lack of test data and the same applies to the state of stress dependence. So in this research, the author has chosen to add the pressure dependence feature to the MAT155 as the improvement of the ice material model.

From the literature review, the author found that in the concrete and soil simulation, the Drucker-Prager yield criteria is always used to represent the pressure dependence feature. So in this research, the author changed the Von-Mises criteria which is used in the MAT155 to the Drucker-Prager yield criteria to see whether there will be an improvement or some different features emerge.

7.2 Drucker-Prager bilinear isotropic hardening model development

7.2.1 Yield function

From the literature reviews, many authors such as Schulson[27], Shazly et al.[11; 12] have observed that the strength of ice is influenced by the pressure.

The yield function at time t+$\Delta t$is given by [26]

$$f = \overline{\sigma^{eff}} - 3\alpha P - \sigma_{ys}(\varepsilon^p) \qquad \textbf{Equation 7-1}$$

Where $\overline{\sigma^{eff}}$ is equivalent stress defined as:

$$\overline{\sigma^{eff}} = \sqrt{3J_2} \qquad \textbf{Equation 7-2}$$

Where 3α, is a parameter related to the internal friction angle of the material. From Pernas-Sánchez's research, this parameter was described as a factor related to the flow stress in compression σ_C and in tension σ_T[8].

$$\alpha = \frac{\sigma_C - \sigma_T}{\sigma_C + \sigma_T} \qquad \textbf{Equation 7-3}$$

Where $\sigma_{ys}(\varepsilon^p)$ is the current yield stress. Normally $\sigma_{ys}(\varepsilon^p)$ is a function of the equivalent plastic strain.

P is the volumetric stress which can be called as hydrostatic pressure as well defined as:

$$P = -\frac{\boldsymbol{\sigma}:\mathbf{1}}{3} \qquad \textbf{Equation 7-4}$$

This defined the pressure would be positive under compression and negative under tension.

7.2.2 Radial return method

The radial return method is the most popular method for integrating the plasticity equation.

In the current time step, the trial stress (equivalent stress), $\sigma_t(\varepsilon^p)$, is the deviatoric part of the stress which can be calculated based on the strain increment directly by assuming that the response is elastic. The key question at this stage is how to calculate the current stress tensor from the trial stress and the yielding condition. The relationship between the trial stress tensor, S_{ij}^t, the current deviatoric stress tensor, $S_{ij}^{(2)}$ and the last time step deviatoric stress tensor, $S_{ij}^{(1)}$ is illustrated in Figure 7-1.

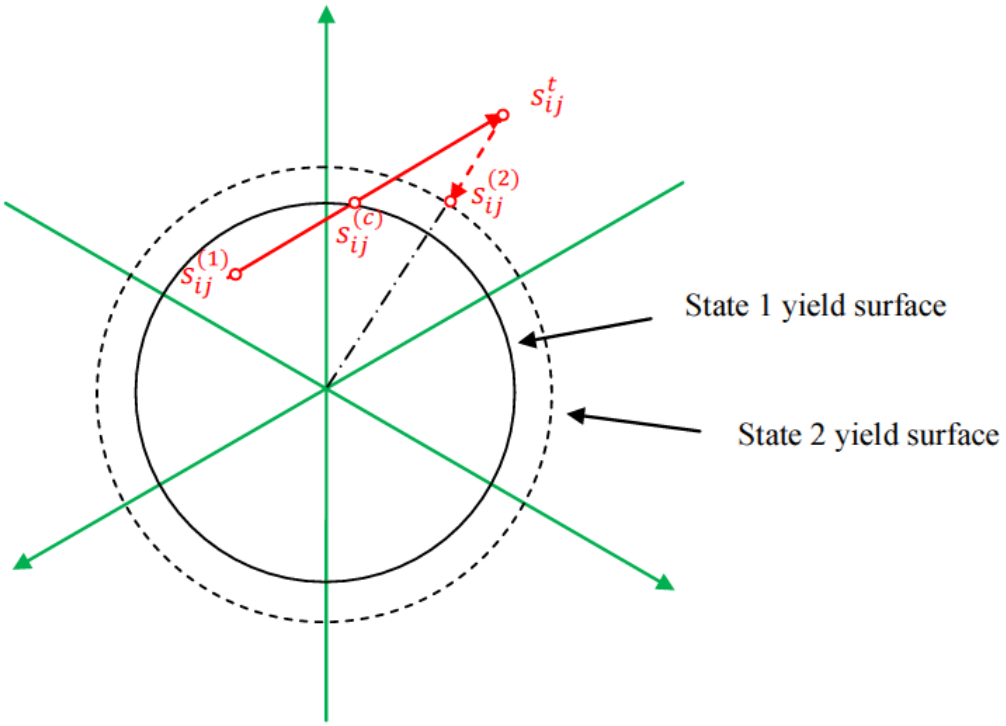

Figure 7-1 Schematic of radial return [44]

The original yield surface is represented as State 1 yield surface. If the plastic flow has already happened in the current time step, the trial stress tensor,S_{ij}^{t}, would cross the original yield surface and the current yield surface which is represented as State 2 yield surface. Thus in this time step, it is necessary to make the current stress state satisfying the current yield condition at the end of this iteration. This is the basic idea of the radial return method. S^{t}

The procedure of the radial return is shown in Figure 7-2

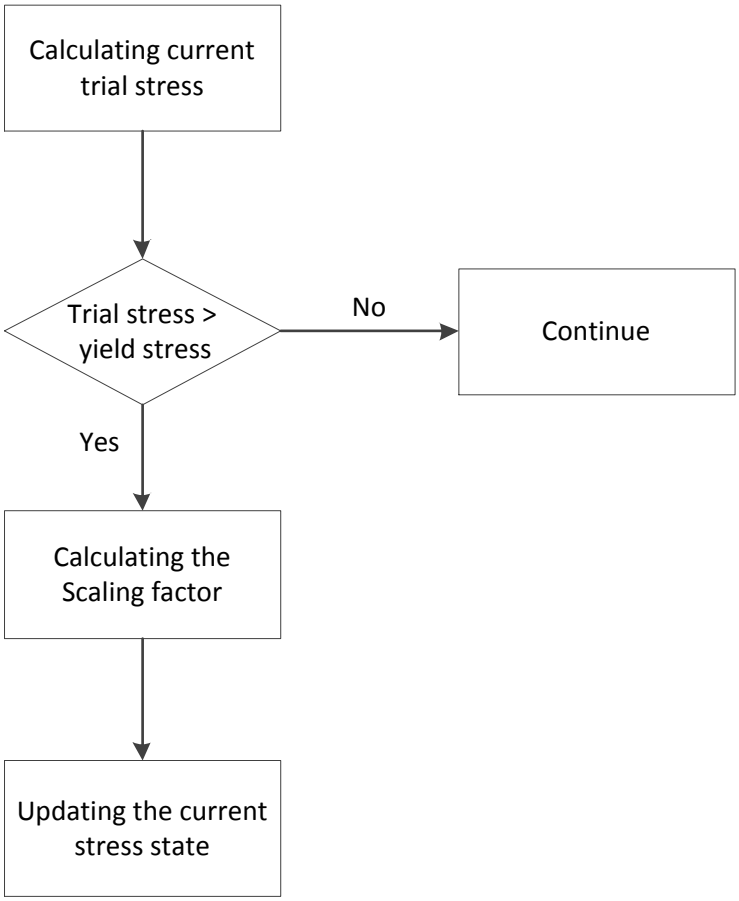

Figure 7-2 Radial return process of pressure based yield stress

When the stress increment is sufficiently small, the deviatoric stress can be updated by multiplying by a scaling factor, κ, which is a function of the current yield stress and the trial stress.

$$\kappa = \frac{{\sigma_{ys}}^{(2)}}{max({\sigma_{ys}}^{(2)}, {\sigma_t}^{(2)})} \qquad \textbf{Equation 7-5}$$

Where ${\sigma_{ys}}^{(2)}$ is the current yield stress and ${\sigma_t}^{(2)}$ is the current trial stress. As mentioned before the trial stress can be gained directly through the strain increment.

$${\sigma_t}^{(2)} = {\sigma_t}^{(1)} + D_{ijkl}\Delta\varepsilon_{kl} \qquad \textbf{Equation 7-6}$$

Where ${\sigma_t}^{(1)}$ is the last time step deviatoric stress, $\Delta\varepsilon_{kl}$ is the strain increment which is already known in the computing process and D_{ijkl} is the generalised linear elasticity stiffness tensor, which can be represented as:

$$D_{ijkl} = 2G[\frac{1}{2}\left(\delta_{ik}\delta_{jl} + \delta_{il}\delta_{jk}\right) + \frac{\mu}{1-2\mu}\delta_{ik}\delta_{jl}] \quad \textbf{Equation 7-7}$$

Where G is the shear modulus and μ is the Poisson ratio.

The crucial task in this stage is to calculate the current yield stress${\sigma_{ys}}^{(2)}$. In this research a bilinear hardening model was adopted. Thus the yield stress, ${\sigma_{ys}}^{(2)}$, can be represented as:

$${\sigma_{ys}}^{(2)} = \sigma_0 + h{\varepsilon^p}^{(2)} \quad \textbf{Equation 7-8}$$

Where ε^p is the plastic strain which can be calculated by:

$${\varepsilon^p}^{(2)} = {\varepsilon^p}^{(1)} + d\varepsilon^p \quad \textbf{Equation 7-9}$$

Where ${\varepsilon^p}^{(2)}$ is the current time step plastic strain. ${\varepsilon^p}^{(1)}$ is the last time step plastic strain, and the $d\varepsilon^p$ is the plastic strain increment in this time step. Based on the Drucker-Prager yield function and the hardening model, the plastic strain increment, $d\varepsilon^p$, can be calculated by:

$$d\varepsilon^p = \frac{1}{3G + h + 9K\alpha^2} \cdot max\left(0, \left({\sigma_t}^{(2)} - {\sigma_{ys}}^{(1)} + 3\alpha P\right)\right) \quad \textbf{Equation 7-10}$$

Where h is the plastic tangent modulus, K is the bulk modulus, ${\sigma_{ys}}^{(1)}$ is last time step yield stress which has already known.

With those equations above the scaling factor κ can be calculated. And the deviatoric stress can be updated by:

$$\boldsymbol{\sigma} = \kappa{\boldsymbol{\sigma}_t}^{(2)} \quad \textbf{Equation 7-11}$$

7.2.3 Drucker-Prager yield function test

The yield stress calculation method in the UMAT, which has been developed in Chapter 6, is changed from the Von-Mises yield criteria to the Drucker-Prager yield criteria. The Equations from 7-8 to 7-11 have been implicated into the UMAT routine

In order to test the Drucker-Prager yield criteria performance a series of single element tests were conducted. These tests basically centre on the different performance from the Von-Mises yield criteria.

The first test is aimed at verifying the function of the Drucker-Prager yield routine by comparing the yield stress calculated by the routine and calculated by hand. Because this test is purely on testing the Drucker-Prager yield criteria, it is necessary to remove other features of the final model such as the failure, the rate dependence, the different performance in tension and compression and the pressure cut-off. It should be noted that the bulk modulus is needed when calculating the effective plastic strain increment,$d\varepsilon^p$, therefore the compaction feature was kept in this test in order to test whether the variable bulk modulus given by the compaction feature can be tracked or not. Thus in this routine this model was simplified into a material with the compaction feature and only have a yield stress value both in tension and compression.

The main process is writing up the routine and run a single element test. The basic condition of the test is listed below.

1. Element geometrical characteristic and the boundary condition:
   The length of the single cube element is 0.01m. These bottom 4 nodes were fixed.

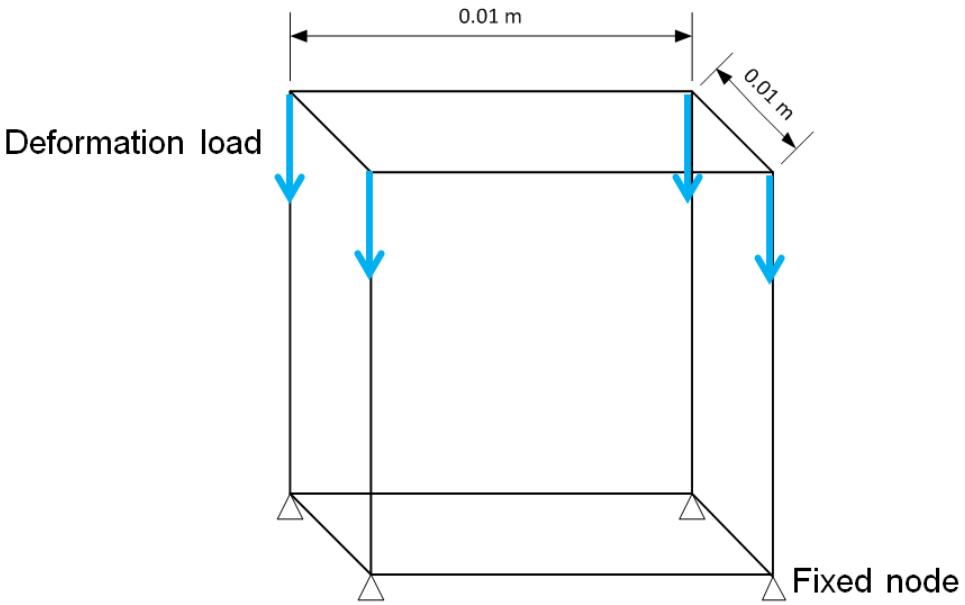

Figure 7-3 Single element geometrical characteristic of Drucker-Prager yield testing

2. Loading condition: compressive loading.

   In this test the yield stress was selected as the compressive yield stress which is 172.4MPa. Based on the basic elastic theory, under the Von-Mises yield criteria when the deformation is 1.2E-4m this element begins to yield. In order to reflect the yield process more clearly, the maximum deformation was set as 6E-4m.

3. Time step and time interval between outputs.

   Because in the manual calculation the effective plastic strain is calculated through integral the equivalent plastic strain increment in each time step, so the deviatoric stress of each time step is needed in this test. Thus the computing time step and the time interval between outputs need to be the same. In this simulation these two values were set as 2e-4s.

The variable bulk modulus was output first, in order to check whether the bulk modulus of the compaction equation of state can be tracked or not.

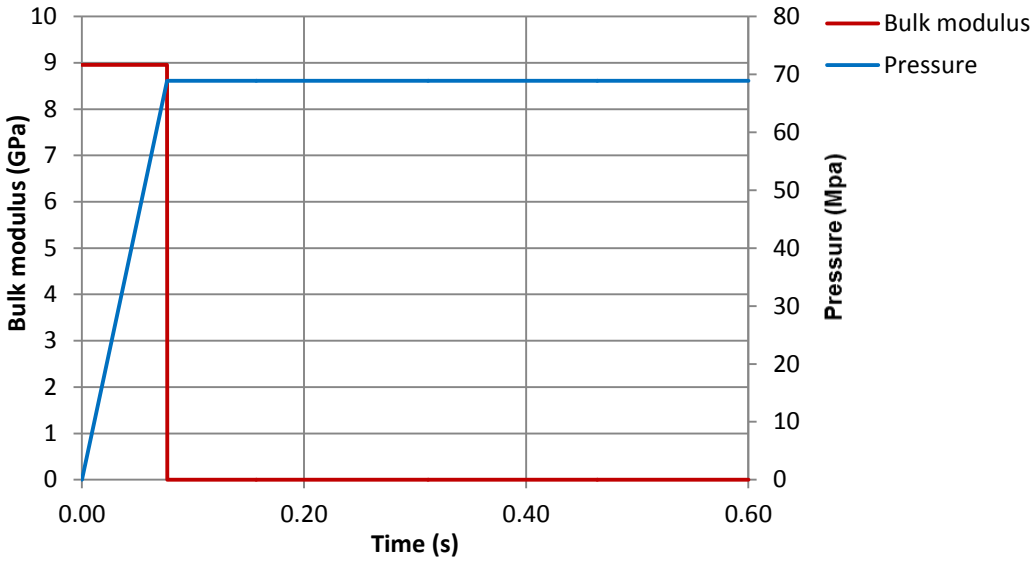

Figure 7-4 Bulk modulus tracking result

From Figure 7-4 it can be seen that the variable bulk modulus was tracked successfully, when the pressure is limited to the value the bulk modulus is zero.

The manually calculated yield stress was calculated from those Equations from 7-6 – 7-11. Substituting the deviatoric stress output from the numerical test to Equation 7-6 and combines the hardening feature shown by Equation 7-8 then Equations 7-9 – 7-11can be solved. Through this procedure the effective plastic strain increment, $d\varepsilon^p$, the yield stress, σ_{ys} , can be calculated out. The comparison of the effective plastic strain increment and the yield stress are show in Figure 7-5 and Figure 7-6 respectively.

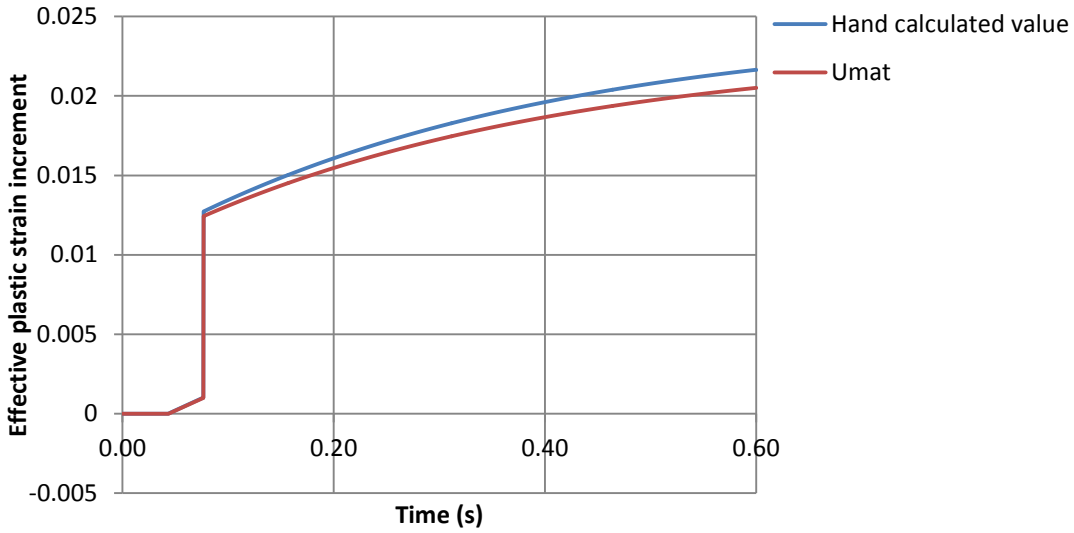

Figure 7-5 Comparison of the Drucker-Prager effective plastic strain increment between the UMAT routine and the manual calculation

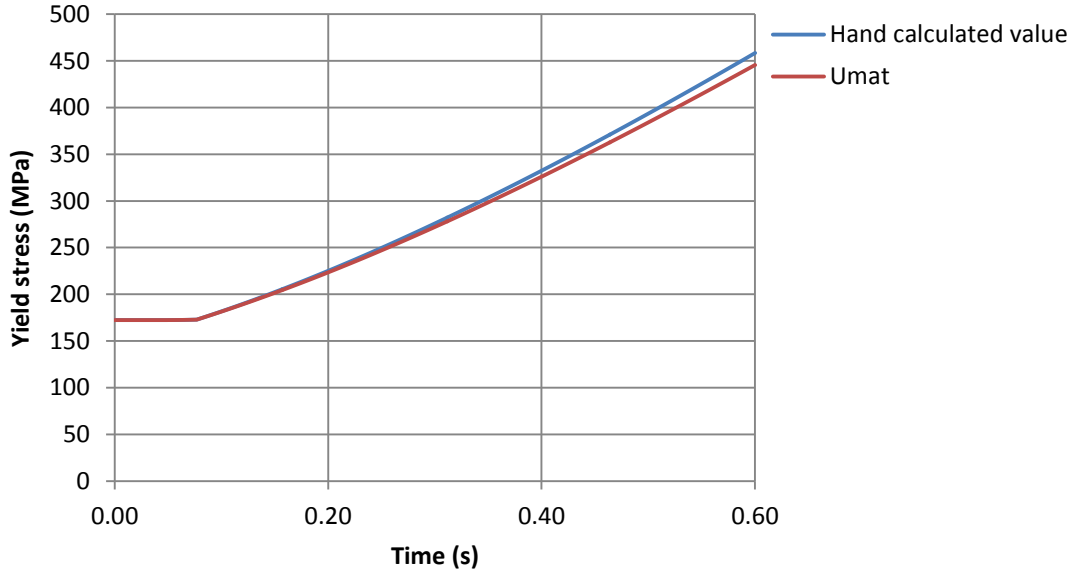

Figure 7-6 Comparison of the Drucker-Prager yield stress between the UMAT routine and manual calculation

These results from this test shows the result from the manual calculation and the UMAT routine are close enough, this routine can match the requirement of the Drucker-Prager yield function.

The second series of tests are aimed at testing the feature of the Drucker-Prager yield criteria. Taking note of the basic expression of the Drucker-Prager yield function, when the stress satisfied the yield condition, this function is equal to 0, thus the effective stress can be represented by the pressure and the yield stress.

$$\overline{\sigma^{eff}} = 3\alpha P + \sigma_{ys}(\varepsilon^{p}) \qquad \textbf{Equation 7-12}$$

Comparing the expression of plastic strain increment between the Von-Mises yield criteria and the Drucker-Prager yield criteria, it can be found that the Drucker-Prager yield criteria reflects the pressure dependent yield stress through the pressure parameterα. Two features were identified by this function.

1. When α was set as 0, the Drucker-Prager yield criteria degraded into the Von-Mises criteria.
2. When α is greater than 0, the material will strengthen as the compression pressure increases, and weakens as the tension pressure increases.

Based on these two features, two tests were conducted. The first one is to set the pressure parameter α as 0, to see whether the function of the Drucker-Prager yield routine will degrade into the Von-Mises yield criteria.

This test problem is the same as the Drucker-Prager yield routine verifying test, run this test problem through the Von-Mises UMAT routine and Drucker-Prager UMAT routine respectively, and compare the effective plastic strain and the yield stress. It should be noted that in this test the compaction feature was kept as well.

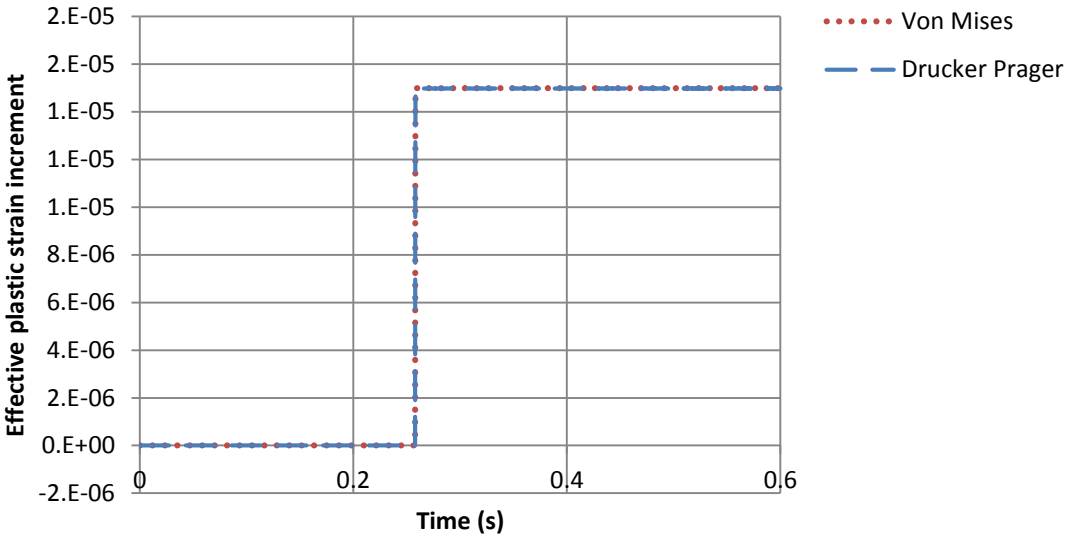

Figure 7-7 Comparison of the effective plastic strain increment between the Von-Mises UMAT routine and Drucker-Prager UMAT routine with pressure parameter set as 0

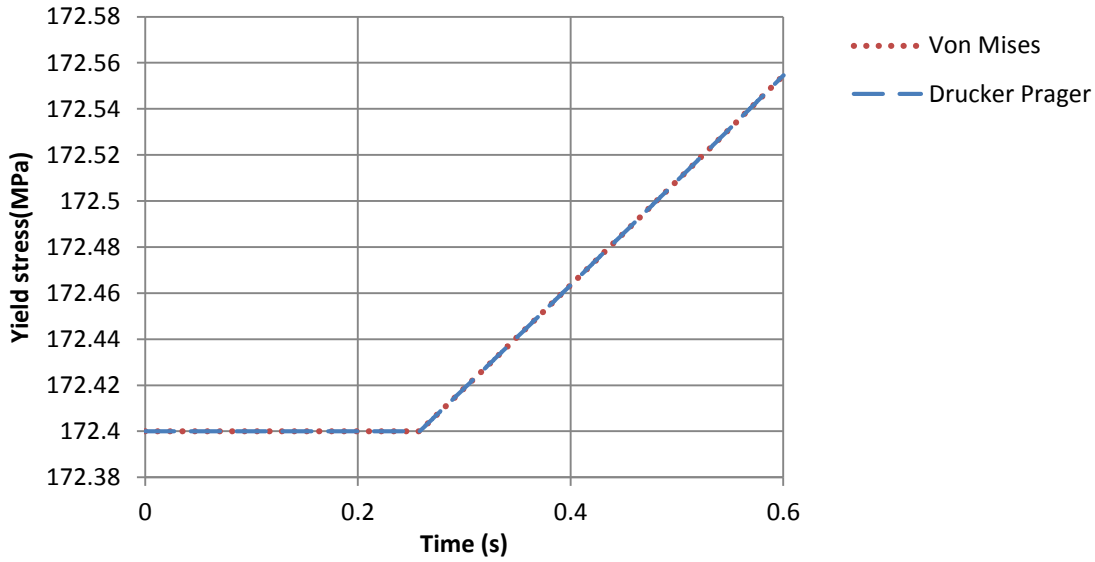

Figure 7-8 Comparison of the yield stress between the Von-Mises UMAT routine and Drucker-Prager UMAT routine with pressure parameter set as 0

From the comparison of these two results it can be found that when setting the pressure parameter α as 0, the Drucker-Prager yield criteria will degrade into the Von-Mises yield criteria.

The final test is aimed at seeing with the pressure parameter how the pressure influences the yield stress in the Drucker-Prager yield criteria. Considering the

original MAT155, under tensile loading the pressure was set as 0 when the pressure is less then -0.433MPa, and under compressive loading the pressure was limited to 6.89E7, and the compaction feature has been tested before. Therefore in order to purely test the influence of the pressure these two limitations and the compaction feature were removed. Also the failure, the rate dependent and the different performance in tension and compression were neglected. Thus this material model was simplified as a normal material whose pressure was calculated as the product of a constant bulk modulus and the volumetric strain, whose initial flow stress is 172.4MPa both in tension and in compression. The failure was not taken into consideration in this test.

Two test problems are tested – the compressive loading test and the tensile loading test. The largest displacement is -6e-4 and 6e-4 respectively. The tested single element is the same as the element used in the Drucker-Prager yield criteria verifying test which was shown in Figure 7-3. The first test is the compressive loading test, the aim is to study how the compressive pressure influences the yield stress. The test result is shown in Figure 7-9.

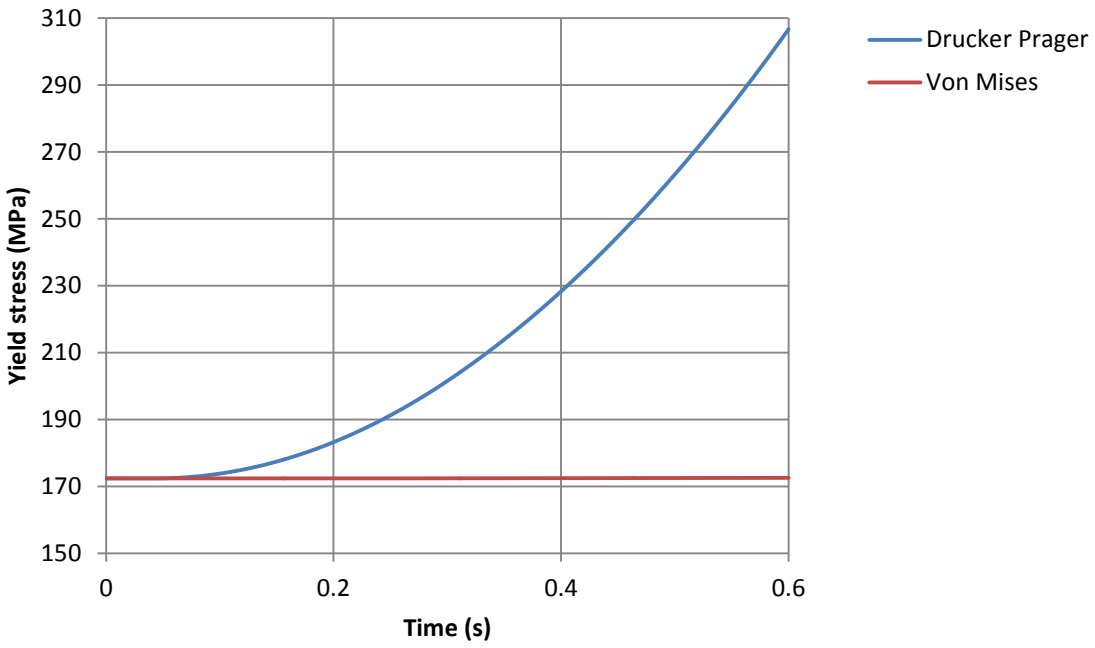

Figure 7-9 Comparison of the yield stress between the Drucker-Prager yield criteria and Von-Mises yield criteria under compressive loading

From Figure 7-9, it can be found that the pressure dependency feature will largely influence the yield stress; this feature will strengthen the material as the compressive pressure increases. It can be deduced that if applying the Drucker-Prager yield criteria to the ice model, the ice would be strengthened more severely than using the Von-Mises criteria.

The other test is the tensile loading test, the aim is to study how the tensile pressure influences the yield stress. The test result is shown in Figure 7-10.

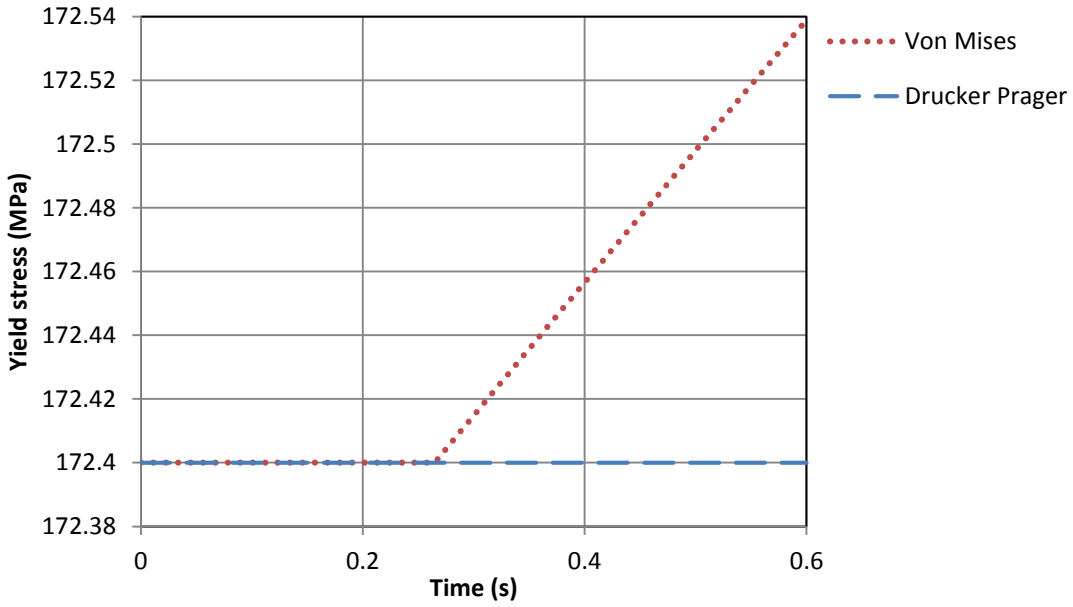

Figure 7-10 Comparison of the yield stress between the Drucker-Prager yield criteria and Von-Mises yield criteria under tensile loading

From Figure 7-10, it can be found that this material modal does not strengthen the material under tensile loading. Checking the effective strain increment function Equation 7-10, it can be found that if the multiplier $\left({\sigma_t}^{(2)} - {\sigma_{ys}}^{(1)} + 3\alpha P\right)$ is less than 0, this multiplier would be set as 0. Then output this multiplier value to figure out the reason why this material has not been strengthened under tensile loading.

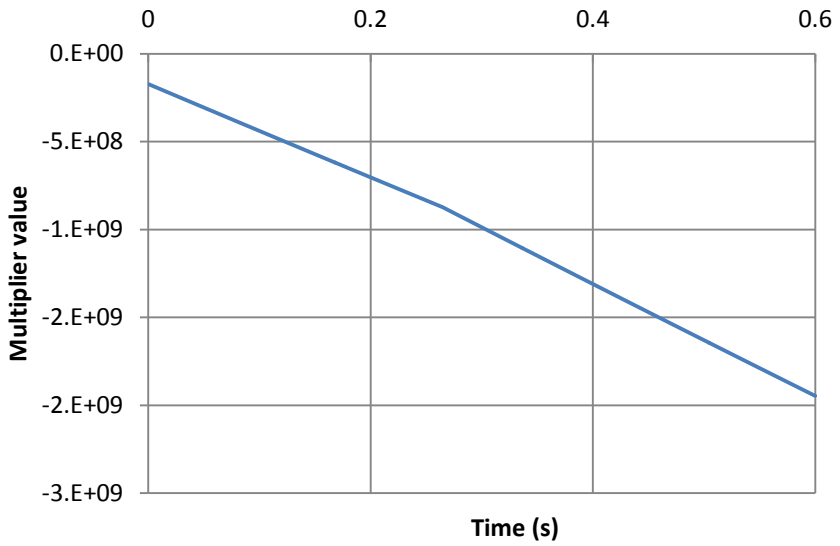

Figure 7-11 Effective plastic strain increment function multiplier value

From Figure 7-11, it should be noted that the value of the multiplier is always 0 during the whole test process, so this value has been set as 0, thus the effective plastic strain increment is always 0 within the whole test process. This is why this material has not been strengthened in the tensile loading.

From these 4 single element tests, it can be concluded that:

1. This Drucker-Prager UMAT routine can track the variable bulk modulus during the calculation.
2. This routine can work properly in calculating the yield stress.
3. This routine will strengthen the material with an increasing compressive pressure.
4. This routine will not strengthen or weaken the material with an increasing tensile pressure.

7.3 Pressure dependent ice material verification

After testing the function of the Drucker-Prager UMAT routine, the Drucker-Prager yield function part of the routine can be applied to the new ice UMAT material model.

Changing the Von-Mises yield function part of the UMAT routine developed before to the Drucker-Prager yield function.

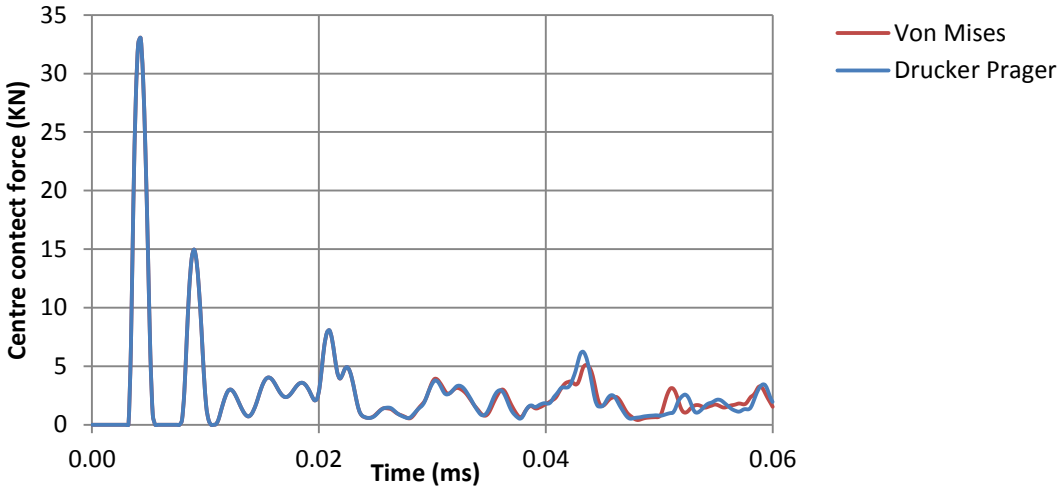

Figure 7-12 Contact force comparison of Von-Mises model and Drucker-Prager model (165m/s)

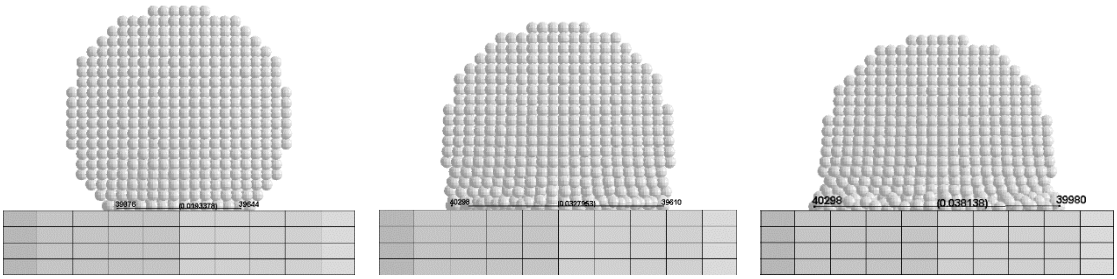

Drucker-Prager (0 state) Drucker-Prager (90 state) Drucker-Prager (224 state)

0.0193378 0.0327953 0.038183

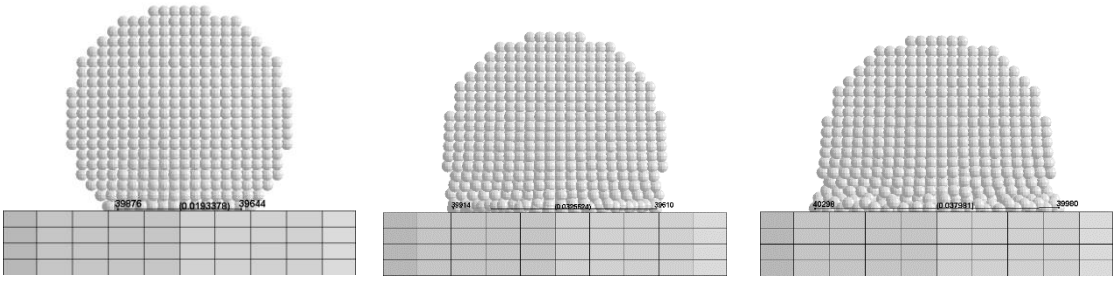

Von-Mises (0 state) Von-Mises (90 state) Von-Mises (224 state)

0.0193378 0.0325624 0.037981

Figure 7-13 Visual comparison of Von-Mises model and Drucker-Prager model (165m/s)

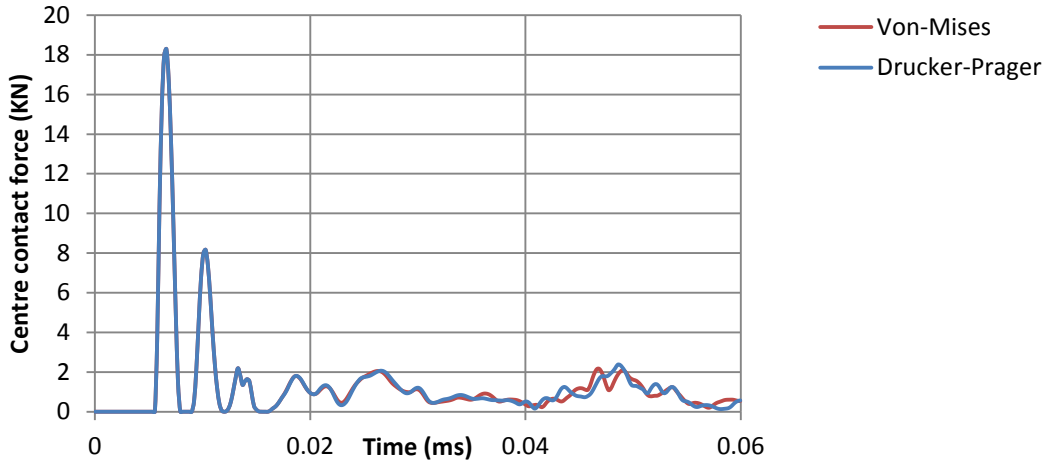

Figure 7-14 Contact force comparison of Von-Mises model and Drucker-Prager model (91m/s)

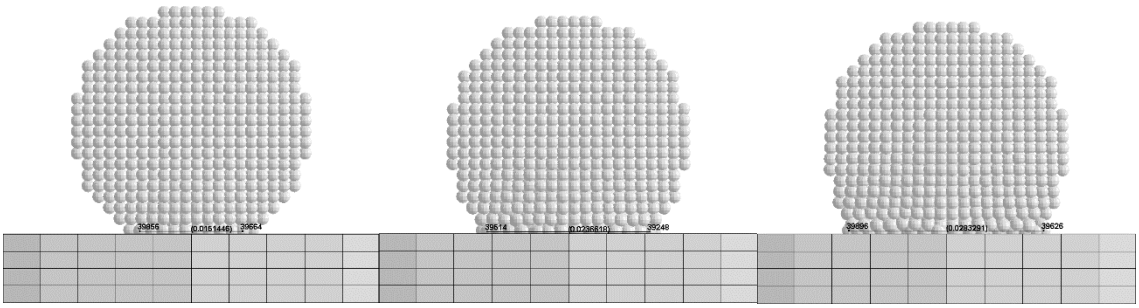

Drucker-Prager (90 state)

0.0151446

Drucker-Prager (180 state)

0.0236618

Drucker-Prager (224 state)

0.0283291

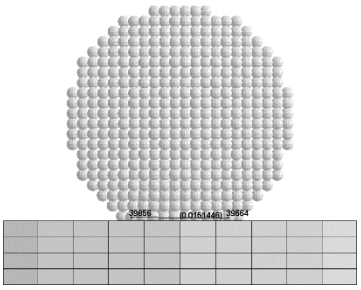

Von-Mises (90 state)

0.0151446

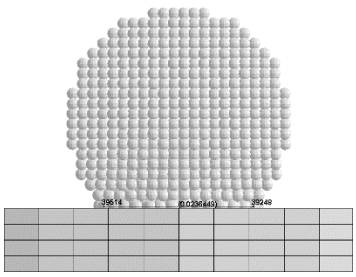

Von-Mises (180 state)

0.0236449

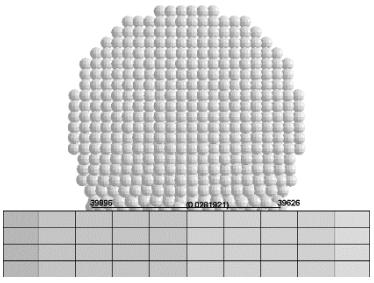

Von-Mises (224 state)

0.0281921

Figure 7-15 Visual comparison of Von-Mises model and Drucker-Prager model (91m/s)

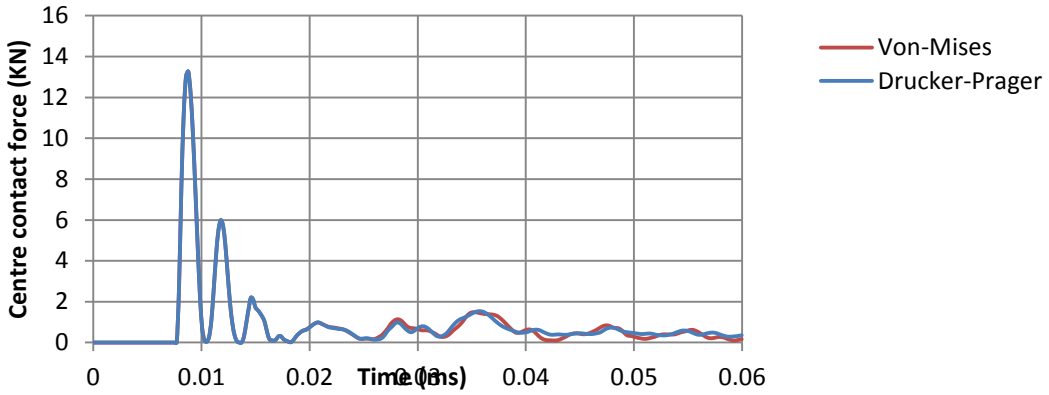

Figure 7-16 Contact force comparison of Von-Mises model and Drucker-Prager model (66m/s)

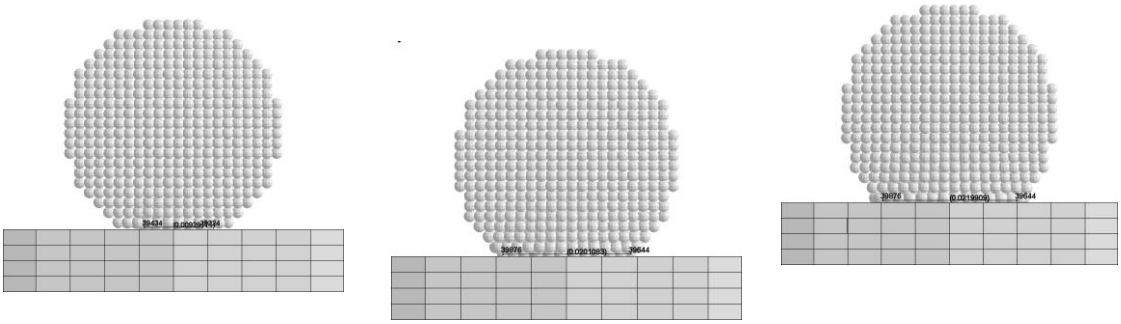

Drucker-Prager (90 state) | Drucker-Prager (180 state) | Drucker-Prager (224 state)

0.00929171 | 0.0201093 | 0.0219909

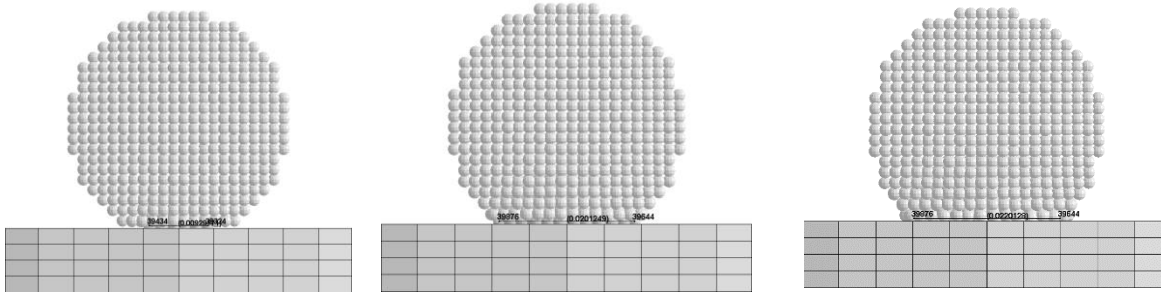

Von-Mises (90 state) | Von-Mises (180 state) | Von-Mises (281 state)

0.00929171 | 0.0201049 | 0.0220128

Figure 7-17 Visual comparison of Von-Mises model and Drucker-Prager model (66m/s)

Frome the test result, it can be seen that at the early stage of the impact process these two material model matches well to each other. The difference emerges at the end of the impact process. This is mainly because at the early stages of the impact process, there are a lot of failures of the ice that happen at the contact face. But by the end of the impact process the contact force is descending, so in this period, the pressure dependent feature shows up.

8 CONCLUSION

8.1 Conclusion

A complete work around the ice material model has been done in this research, the main contents of this research are summarised below:

1. The properties of ice are fully investigated through the literature review. Eight properties which are crucial for ice modelling are summarised. This work set up a foundation of assessing the ice material model.
2. Five ice material models are assessed theoretically. It concluded that the MAT 155 model is the most appropriate material model for ice, but 3 important features were not included in MAT 155 – pressure dependence, loading condition dependence and temperature dependence; the Pernas-Sánchez model is equipped with the pressure dependence through using the Drucker-Prager yield criteria, but the material cohesion should be set as current yield stress rather than a constant value, and nonlinear bulk response was not constructed in this material model.
3. Two material models which are available to use in LS-Dyna were assessed numerically through simulating three different test problems. The conclusion was that MAT 13 is not suitable for modelling ice because there is a concentration of the impact force which is nearly equal to the total force on the centre area of the target which made it successful in modelling the load cell test but failed in modelling the pressure transducer test; MAT 155 can model the cylinder ice projectile successfully but does not perform well in modelling the spherical ice projectile which was expected that the loading condition dependence was not composed in this material model.
4. The modified method was proposed based on the theoretical and numerical assessments. MAT 155 can be modified by changing the Von-Mises yield criteria to the Drucker-Prager criteria or adding the temperature dependence or adding the loading condition dependence.
5. As a basis for further research, a user defined material routine is developed according to the part of MAT 155 which is related to the ice

material model, and verified through a series of single element tests and the simulation of a true test.

6. The Drucker-Prager yield criteria was added into the user defined material routine. The new user defined material routine is verified through a series of tests which shows that the new routine can work properly in the single element test but there is no big difference between the test result from the new routine and the original routine and the slight difference is the force value in the later stages of the impact.

8.2 Recommendations for further work

Although a complete work has been done around ice properties and the ice material model also a modified material model is proposed in this research, but there still are several domains where improvements are required. The modified work was restricted to the yield criteria, but there are two other modifications of the MAT 155 which are worth researching more in the future – the temperature dependence and loading condition dependence. Also, no work has been done on the residual strength of the ice after impact and the visco-elastic stress calculated using a Prony series. However, this domain can be quite difficult to study because of the numerical data that is needed to model these phenomena correctly.

REFERENCES

[1] Souter, R. K. and Emerson, J. B. (1952), *Summary of available hail literature and the effect of hail on aircraft in flight,* .

[2] Render, P. and Pan, H. (1995), "Experimental studies into hail impact characteristics", *Journal of Propulsion and Power,* vol. 11, no. 6, pp. 1224-1230.

[3] Kim, H. and Kedward, K. T. (2000), "Modeling hail ice impacts and predicting impact damage initiation in composite structures", *AIAA Journal,* vol. 38, no. 7, pp. 1278-1288.

[4] Carney, K. S., Benson, D. J., DuBois, P. and Lee, R. (2006), "A phenomenological high strain rate model with failure for ice", *International Journal of Solids and Structures,* vol. 43, no. 25, pp. 7820-7839.

[5] Field, P., Hand, W., Cappelluti, G. and McMillan, A. (2008), "Hail threat standardisation", *Research project EASA,* vol. 5.

[7] Pereira, J. M., Padula, S. A., Revilock, D. M. and Melis, M. E. (2006), "Forces generated by high velocity impact of ice on a rigid structure", .

[8] Pernas-Sánchez, J., Pedroche, D. A., Varas, D., López-Puente, J. and Zaera, R. (2012), "Numerical modeling of ice behavior under high velocity impacts", *International Journal of Solids and Structures,* vol. 49, no. 14, pp. 1919-1927.

[9] Hallquist, J. O. (2007), "LS-DYNA keyword user's manual", *Livermore Software Technology Corporation,* vol. 970.

[10] Kim, H. and Keune, J. N. (2007), "Compressive strength of ice at impact strain rates", *Journal of Materials Science,* vol. 42, no. 8, pp. 2802-2806.

[11] Shazly, M., Prakash, V. and Lerch, B. A. (2009), "High strain-rate behavior of ice under uniaxial compression", *International Journal of Solids and Structures,* vol. 46, no. 6, pp. 1499-1515.

[12] Shazly, M., Prakash, V. and Lerch, B. A. (2006), "High-strain-rate compression testing of ice", .

[13] Kim, H. and Keune, J. N. (2007), "Compressive strength of ice at impact strain rates", *Journal of Materials Science,* vol. 42, no. 8, pp. 2802-2806.

[14] Tippmann, J. D., Kim, H. and Rhymer, J. D. (2013), "Experimentally validated strain rate dependent material model for spherical ice impact simulation", *International Journal of Impact Engineering,* vol. 57, pp. 43-54.

[15] Tippmann, J. D. (2011), "Development of a strain rate sensitive ice material model for hail ice impact simulation", MSc Thesis. *UC San Diego* 2011.

[16] Appleby-Thomas, G. J., Hazell, P. J. and Dahini, G. (2011), "On the response of two commercially-important CFRP structures to multiple ice impacts", *Composite Structures,* vol. 93, no. 10, pp. 2619-2627.

[17] Askari, A., Nelson, K., Weckner, O., Xu, J. and Silling, S. (2011), "Hail impact characteristics of a hybrid material by advanced analysis techniques and testing", *Journal of Aerospace Engineering,* vol. 24, no. 2, pp. 210-217.

[18] Heimbs, S., Cichosz, J., Klaus, M., Kilchert, S. and Johnson, A. (2010), "Sandwich structures with textile-reinforced composite foldcores under impact loads", *Composite structures,* vol. 92, no. 6, pp. 1485-1497.

[19] Johnson, A. F. and Holzapfel, M. (2003), "Modelling soft body impact on composite structures", *Composite Structures,* vol. 61, no. 1, pp. 103-113.

[20] Kim, H., Welch, D. A. and Kedward, K. T. (2003), "Experimental investigation of high velocity ice impacts on woven carbon/epoxy composite panels", *Composites Part A: applied science and manufacturing,* vol. 34, no. 1, pp. 25-41.

[21] Park, H. and Kim, H. (2010), "Damage resistance of single lap adhesive composite joints by transverse ice impact", *International Journal of Impact Engineering,* vol. 37, no. 2, pp. 177-184.

[22] Rhymer, J., Kim, H. and Roach, D. (2012), "The damage resistance of quasi-isotropic carbon/epoxy composite tape laminates impacted by high velocity ice", *Composites Part A: Applied Science and Manufacturing,* vol. 43, no. 7, pp. 1134-1144.

[23] Park, H. (2006), *Resistance of adhesively bonded composite lap joints to damage by transverse ice impact,* MSc Thesis, *Purdue University, 2006.*

[24] Keune, J. (2004), *Development of a hail ice impact model and the dynamic compressive strength properties of ice,* .MS thesis, *Purdue University West Lafayette*, 2004

[25] Anghileri, M., Castelletti, L., Invernizzi, F. and Mascheroni, M. (2005), "A survey of numerical models for hail impact analysis using explicit finite element codes", *International Journal of Impact Engineering,* vol. 31, no. 8, pp. 929-944.

[26] Allen, P. A. and Wilson, C. D. (2004), "Development of a pressure-dependent constitutive model with combined multi-linear kinematic and isotropic hardening", *ABAQUS Users' Conference,* pp. 49.

[27] Schulson, E. M. (2001), "Brittle failure of ice", *Engineering Fracture Mechanics,* vol. 68, no. 17–18, pp. 1839-1887.

[28] Schulson, E. (1990), "The brittle compressive fracture of ice", *Acta Metallurgica et Materialia,* vol. 38, no. 10, pp. 1963-1976.

[29] Kennedy, F., Schulson, E. and Jones, D. (2000), "The friction of ice on ice at low sliding velocities", *Philosophical Magazine A,* vol. 80, no. 5, pp. 1093-1110.

[30] Smith, T. and Schulson, E. (1993), "The brittle compressive failure of fresh-water columnar ice under biaxial loading", *Acta metallurgica et materialia,* vol. 41, no. 1, pp. 153-163.

[31] Schulson, E. and Gratz, E. (1999), "The brittle compressive failure of orthotropic ice under triaxial loading", *Acta materialia,* vol. 47, no. 3, pp. 745-755.

[32] Petrovic, J. (2003), "Review mechanical properties of ice and snow", *Journal of Materials Science,* vol. 38, no. 1, pp. 1-6.

[33] DeWitt, K. J. and Britton, R. K. (1994), "Measurements of the impact forces of shed ice striking a surface", http://arc.aiaa.org/doi/abs/10.2514/6.1994-713 .

[34] Lucy, L. B. (1977), "A numerical approach to the testing of the fission hypothesis", *The astronomical journal,* vol. 82, pp. 1013-1024.

[35] Gingold, R. A. and Monaghan, J. J. (1977), "Smoothed particle hydrodynamics: theory and application to non-spherical stars", *Monthly notices of the royal astronomical society,* vol. 181, no. 3, pp. 375-389.

[36] Allahdadi, F. A., Carney, T. C., Hipp, J. R., Libersky, L. D. and Petschek, A. G. (1993), *High strain Lagrangian hydrodynamics: a three dimensional SPH code for dynamic material response,* .

[37] Vignjevic, R. and Campbell, J. (2009), "Review of development of the smooth particle hydrodynamics (SPH) method", in *Predictive Modeling of Dynamic Processes,* Springer, , pp. 367-396.

[38] Swegle, J., Hicks, D. and Attaway, S. (1995), "Smoothed particle hydrodynamics stability analysis", *Journal of computational physics,* vol. 116, no. 1, pp. 123-134.

[39] Johnson, G. R., Stryk, R. A. and Beissel, S. R. (1996), "SPH for high velocity impact computations", *Computer Methods in Applied Mechanics and Engineering,* vol. 139, no. 1, pp. 347-373.

[40] Bathe, K. (2006), *Finite element procedures,* Klaus-Jurgen Bathe.

[41] Truchelut, F. Modelling Hail Ice Impact Upon Composite Fan Blades. MSc Thesis. *Cranfield University.* 2010.

[42] Bee, T. A Study into Hailstone Impacts upon Compressor Blades. MSc Thesis. *Cranfield University.* 2008.

[43] Vigneau, M. Study of Ice Impact on Aerospace Components. MSc Thesis. *Cranfield University.* 2005.

[44] KRABBENHØFT, KRISTIAN. "Basic computational plasticity." Lecture Notes (2002). http://homes.civil.aau.dk/lda/continuum/plast.pdf

Appendix A Ice UMAT

```
      subroutine umat41 (cm,eps,sig,epsp,hsv,dt1,capa,etype,tt,
     1 temper,failel,crv,cma,qmat,elsiz,idele)
c
c************************************************************************
c|  Livermore Software Technology Corporation  (LSTC)                    |
c|  ---------------------------------------------------------  |
c|  Copyright 1987-2008 Livermore Software Tech. Corp                    |
c|  All rights reserved                                                  |
c************************************************************************
c
c     isotropic elastic material (sample user subroutine)
c
c     Variables
c     cm(1)=first material constant, here young's modulus
c     cm(2)=second material constant, here poisson's ratio
c     cm(6)=eos solution control
c     cm(7)=initial yield stress
c     cm(8)=harding parameter
c     cm(9)=meanstress in compression
c     cm(10)=meanstress in tension
c     cm(11)=load curve id defining yield stress versus effective plastic strain
             in compression
c     cm(12)=load curve id defining yield stress versus effective plastic strain
             in tension
c     cm(13)=initial compressive flow stress
c     cm(14)=initial compressive flow stress
c     cm(15)=pressure cut-off in compression
c     cm(16)=pressure cut-off in tension
c     cm(17)=load curve id defining strain rate sensitivity
c     cm(20)=maximum PEOS
c     cm(21)=PCUTF
c     cm(22)=whether set to PCUTC when exceeding the PCUTC
c     cm(n)=nth material constant
c     eps(1)=local x  strain increment
c     eps(2)=local y  strain increment
c     eps(3)=local z  strain increment
c     eps(4)=local xy strain increment
c     eps(5)=local yz strain increment
c     eps(6)=local zx strain increment
c
c     sig(1)=local x  stress
c     sig(2)=local y  stress
c     sig(3)=local z  stress
c     sig(4)=local xy stress
c     sig(5)=local yz stress
c     sig(6)=local zx stress
c
c     devia(1)=local x  deviatoric stress
c     devia(2)=local y  deviatoric stress
c     devia(3)=local z  deviatoric stress
c     devia(4)=local xy deviatoric stress
c     devia(5)=local yz deviatoric stress
c     devia(6)=local zx deviatoric stress
c
c     hsv(1)=current volumatric strain
```

```
c     hsv(2)=current element pressure
c     hsv(3)=diviatoric stress 1
c     hsv(4)=diviatoric stress 2
c     hsv(5)=diviatoric stress 3
c     hsv(6)=diviatoric stress 4
c     hsv(7)=diviatoric stress 5
c     hsv(8)=diviatoric stress 6
c     hsv(9)=historical maximum volumetric strain
c     hsv(10)=eos bulk modulus
c        .
c     hsv(n)=nth history variable
c
c     dt1=current time step size
      include 'nlqparm'
      include 'bk06.inc'
      include 'iounits.inc'
      dimension cm(*),eps(*),sig(*),hsv(*),crv(lq1,2,*),cma(*),qmat(3,3)
      dimension devia(6),devs(6)
      logical failel
      character*5 etype
c
      if (ncycle.eq.1) then
        if (cm(16).ne.1234567) then
          call usermsg('mat41')
        endif
      endif
      if(hsv(9).gt.-1.0e-7) hsv(9) = -1.0E-07
c
c
      g2 =abs(cm(1))/(1.+cm(2))
      g  =.5*g2
      if (etype.eq.'solid') then
        if (cm(16).eq.1234567) then
          call mitfail3d(cm,eps,sig,epsp,hsv,dt1,capa,failel,tt,crv)
        else
          if (.not.failel) then
c Computing current volumetric strain
          ev=eps(1)+eps(2)+eps(3)
          davg=ev/3
          es=sqrt((2/9)*((eps(1)-eps(2))**2+(eps(2)-eps(3))**2
     &     +(eps(3)-eps(1))**2)+(6*(eps(4)**2+eps(5)**2+eps(6)**2)))
          esr=es/dt1
c Computing volumetric strain
          hsv(1)=hsv(1)+ev
c Computing the pressure
          if (hsv(9).gt.hsv(1)) then
            hsv(9)=hsv(1)
          end if
c
          external_lc_id = cm(5)
          call crvval(crv,external_lc_id,hsv(9),y_lc,sl_lc)
          bulktrack = sl_lc
          eosnumber=cm(6)
          if (eosnumber.gt.1) then
          hsv(2)=y_lc-abs((cm(1))/(3*(1.-2.*cm(2))))*(hsv(1)-hsv(9))
          hsv(2)=max(0.0,hsv(2))
          else
          hsv(10)=y_lc/hsv(9)
          hsv(2)=hsv(1)*hsv(10)
          end if
```

```
            if (cm(21).gt.0) then
                hsv(2)=max(0.0,hsv(2))
            else
                hsv(2)=max(cm(16),hsv(2))
            end if
            davg=ev/3
            devia(1)=eps(1)-davg
            devia(2)=eps(2)-davg
            devia(3)=eps(3)-davg
            devia(4)=eps(4)
            devia(5)=eps(5)
            devia(6)=eps(6)
            hsv(21)=hsv(21)+eps(1)
            hsv(22)=hsv(22)+eps(2)
            hsv(23)=hsv(23)+eps(3)
            hsv(24)=hsv(24)+eps(4)
            hsv(25)=hsv(25)+eps(5)
            hsv(26)=hsv(26)+eps(6)
            hsv(27)=(2/3)*sqrt((3/2)*(hsv(21)**2+hsv(22)**20+hsv(23)**2)+
     &           (3/4)*(hsv(24)**2+hsv(25)**2+hsv(26)**2))
c Computing Deviatoric Stress
            hsv(3)=hsv(3)+g2*devia(1)
            hsv(4)=hsv(4)+g2*devia(2)
            hsv(5)=hsv(5)+g2*devia(3)
            hsv(6)=hsv(6)+g*devia(4)
            hsv(7)=hsv(7)+g*devia(5)
            hsv(8)=hsv(8)+g*devia(6)
            if (hsv(2).lt.cm(16)) then
                hsv(3)=0
                hsv(4)=0
                hsv(5)=0
                hsv(6)=0
                hsv(7)=0
                hsv(8)=0
                hsv(2)=0
                sig(1)=0
                sig(2)=0
                sig(3)=0
                sig(4)=0
                sig(5)=0
                sig(6)=0
            end if
            if (hsv(2).gt.cm(15)) then
                if (cm(22).gt.0) then
                hsv(2)=cm(15)
                hsv(3)=0
                hsv(4)=0
                hsv(5)=0
                hsv(6)=0
                hsv(7)=0
                hsv(8)=0
                sig(1)=-hsv(2)
                sig(2)=-hsv(2)
                sig(3)=-hsv(2)
                sig(4)=0
                sig(5)=0
                sig(6)=0
                else
                hsv(3)=0
                hsv(4)=0
```

```
          hsv(5)=0
          hsv(6)=0
          hsv(7)=0
          hsv(8)=0
          sig(1)=-hsv(2)
          sig(2)=-hsv(2)
          sig(3)=-hsv(2)
          sig(4)=0
          sig(5)=0
          sig(6)=0
          end if
      end if
      mstress_c=cm(9)
      mstress_t=cm(10)
      sy0c=cm(13)
      sy0t=cm(14)
      fam=(sy0c-sy0t)/(sy0c+sy0t)
      ofac=1.0/(3.0*g+h-9.0*bulktrack*fam*fam)
      external_lc_c = -cm(11)
      external_lc_t = -cm(12)
      external_lc_cc = -cm(18)
      peps=hsv(11)
      aj2=sqrt(1.5*(hsv(3)**2)+(hsv(4)**2)+(hsv(5)**2)+
     &3.0*(hsv(6)**2)+(hsv(7)**2)+(hsv(8)**2))
      hsv(17)=aj2
      hsv(18)=bulktrack
      hsv(19)=fam
      hsv(20)=ofac
      if (hsv(2).gt.0) then
          call crvval(crv,external_lc_cc,esr,y_sesr,sl_cesr)
          if (hsv(2).gt.mstress_c) then
          sy0=sy0c
          sy=y_sesr*(sy0+h*peps)
          peps=peps+ofac*max(0.0,aj2-sy+3*fam*hsv(2))
          hsv(11)=peps
          synew=y_sesr*(sy0+h*peps)
          else
          sy0=sy0c-(sy0c-sy0t)*(mstress_c-hsv(2))
     &       /(mstress_c-mstress_t)
          peps=peps+ofac*max(0.0,aj2-sy+3*fam*hsv(2))
          hsv(11)=peps
          synew=y_sesr*(sy0+h*peps)
          end if
      else if (hsv(2).lt.mstress_t) then
          sy0=sy0t
          sy=sy0+h*peps
          peps=peps+ofac*max(0.0,aj2-sy+3*fam*hsv(2))
          hsv(11)=peps
          synew=sy0+h*peps
      else
          sy0=sy0c-(sy0c-sy0t)*(mstress_c-hsv(2))
     &       /(mstress_c-mstress_t)
          sy=sy0+h*peps
          peps=peps+ofac*max(0.0,aj2-sy+3*fam*hsv(2))
          hsv(11)=peps
          synew=sy0+h*peps
      end if
      scale=synew/max(synew,aj2)
      hsv(16) = synew
      hsv(15) = aj2-sy+3*fam*hsv(2)
```

```
    hsv(14) = g2
        hsv(3)=scale*hsv(3)
        hsv(4)=scale*hsv(4)
        hsv(5)=scale*hsv(5)
        hsv(6)=scale*hsv(6)
        hsv(7)=scale*hsv(7)
        hsv(8)=scale*hsv(8)
        sig(1)=hsv(3)-hsv(2)
        sig(2)=hsv(4)-hsv(2)
        sig(3)=hsv(5)-hsv(2)
        sig(4)=hsv(6)
        sig(5)=hsv(7)
        sig(6)=hsv(8)
    end if
    if (cm(1).lt.0.) then
      if (sig(1).gt.cm(5)) failel=.true.
    endif
    endif
else
  cerdat(1)=etype
  call lsmsg(3,MSG_SOL+1150,ioall,ierdat,rerdat,cerdat,0)
endif
return
end
```

Appendix B Pressure recording test

B.1 Basic idea

The object of the tests is to investigate ice mechanical behaviour under high strain rate impact condition. Based on the successful experience from the papers the test was based on those three critical parts which are shown in figure B1: stress-time history, kinematic behaviour of ice and observing the crack generation and expansion of the ice during the impact event. So the test facility must have basic equipment that can acquire those three aspects of information. We scheduled the below facilities to run the tests: transmitting device, speed measuring device, dynamic stress measuring device, and high-speed camera.

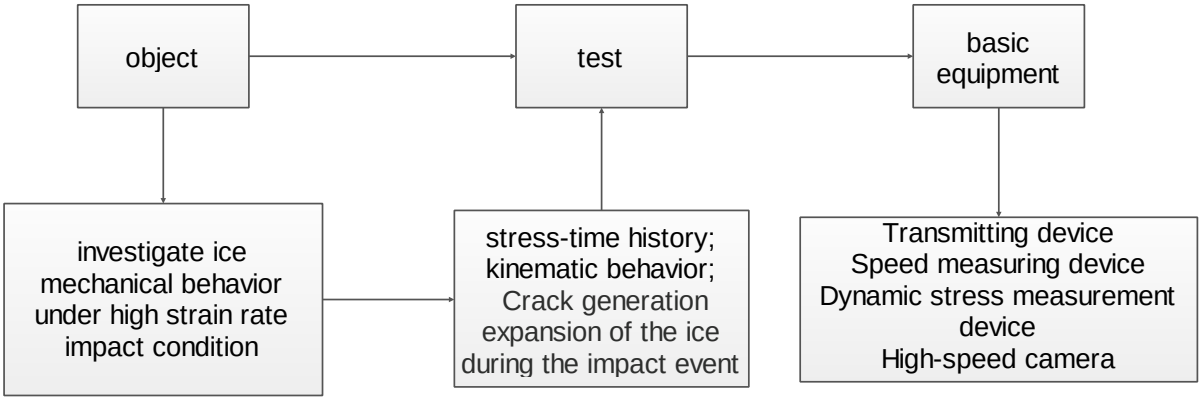

Figure B1 Basic idea

B.2 Test assumption and simplification

Test assumption and simplification should be taken into consideration. There are 3 aspects that need to be noticed.

1. The most important one is impact speed. The impact speed will decide which experimental speed should be performed. According to the reference, the hail freefall speed is 25m/s, and the maximum intake flow rate is 280m/s, so the test speed should be located within this range.
2. The following one is test environment, especially the temperature. Hail always formed in the Cumulonibus, this kind of cloud is always shown in 600 to 1200km above the sea level. And the temperature range from 0 to

50 degree centigrade which is very hard for us to reach when doing the test.

3. The third one is the structure of the hail stone. The structure of the hail is polycrystalline which consisted of alternate layers of clear and opaque ice, as many as 20-25 layers. Sometimes the centre of the hail contains air bubbles. It is quite difficult to produce such kind of ice sample in the lab.

To sum up those three issues, three aspects of simplification could be proposed.

1. Impact speed, since damage is always caused when the speed is above 50 meters per second, so we can range our test speed a little higher than 50m/s. There is a limitation in the equipment – when the speed reaches 230m/s, the transducer will broke. So finally we chose the below 3 speeds: 60m/s, 90m/s, 160m/s.

2. Since the environment is difficult to reach in the lab, so we have to ignore it. Our test temperature is 5 degree centigrade.

3. Then comes to the ice sample, the sample that obtained in the lab is ice sphere with polycrystalline structure. There is no layer, no macroscopic cracks in it. The centre of the ice sample contains some small air bubbles that can be considered as the air bubbles in the centre of the real hail stone.

B.3 Test instrumentations

The instrumentations that need to be used in this test are listed below Figure B2. The air gun is needed to accelerate the ice sample, then the ice sample will pass through a laser speedometer meanwhile its velocity would be recorded. At last the ice sample will impact target where there is a stress measuring device installed on it. Through this device the stress-time history could be obtained. Also a high-speed camera focuses on the target, observing the kinematic behaviour and crack generation and expansion.

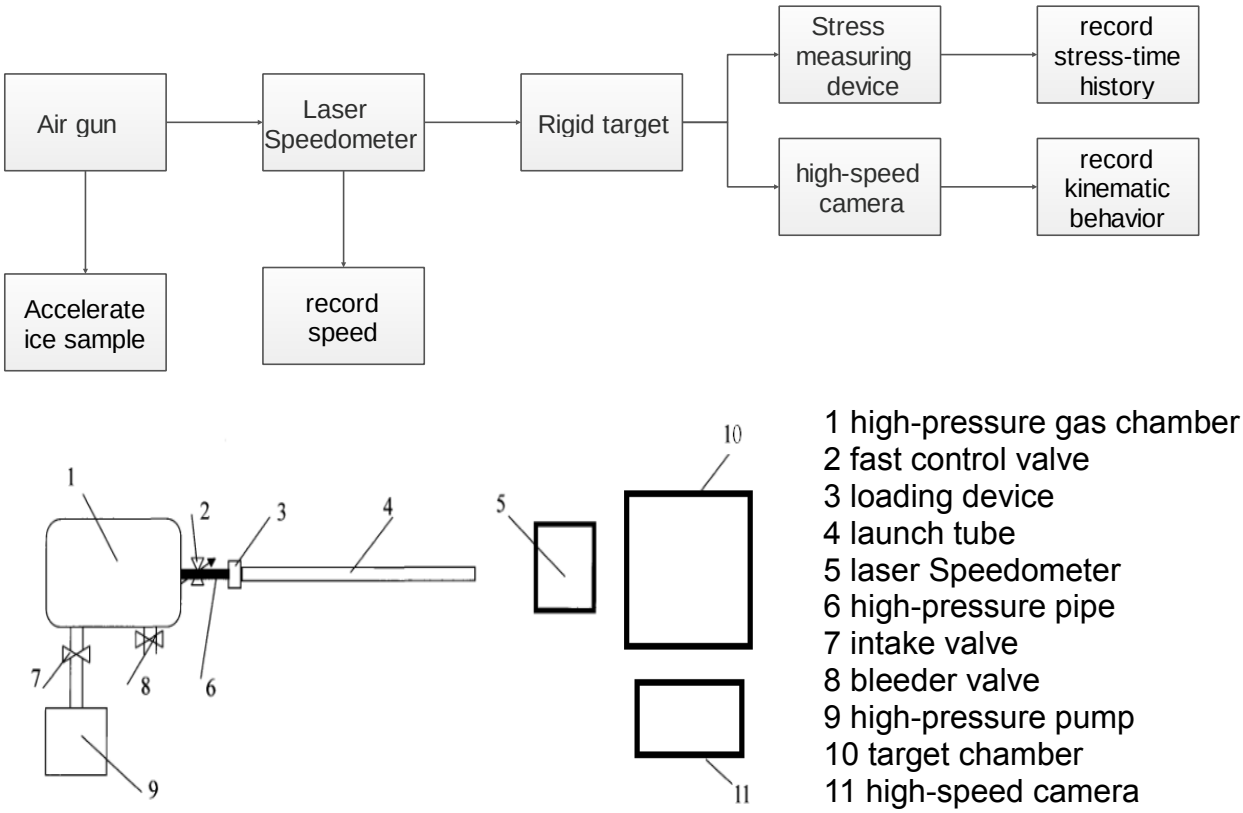

Figure B2 Test instruments

- The first step is to install the ice sample into the loading device, then open NO. 7 intake valve. High-pressure gas start to go into no.1 high-pressure gas chamber. After the pressure in high-pressure gas chamber reach the target pressure, we can open NO.2 fast control valve through software, the ice sample would be lunched immediately. The launch tube is 2 meters long.

- Then come to the laser speedometer, ice sample pass through the device from left to the right, the front-end signal processing would starts to count time when the laser which irradiating to the first receiving end was cut down by the sample, and reradiating when the laser which irradiating to the second receiving end was cut down. This picture is time measurement display.

1 laser source
2 photoelectric converter
3 front-end signal processing
4 time measurement display

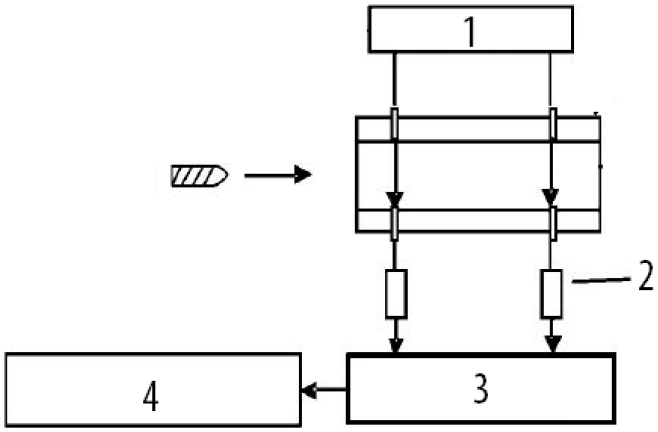

Figure B2 Speed recording instrument

- Rigid target is shown in Figure B4. The diameter of the target is 20cm. There are 5 transducers installed on the rigid target – one is located in the centre and the others are surrounding. the material of the target is medium carbon steel (N0. 45).

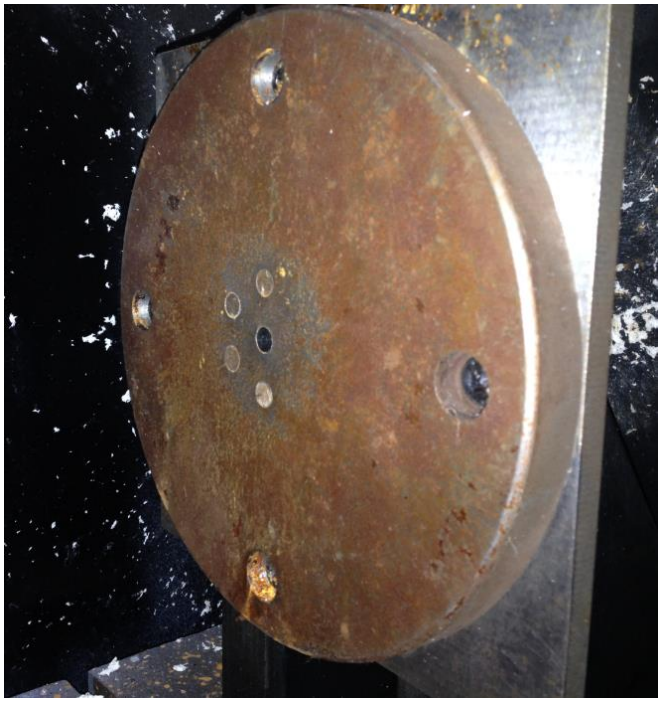

Figure B4 Rigid target

- The stress measuring module contains three devices as shown in Figure B5: The first picture is PPM-SY03 Piezoelectricity stress transducer (dynamic). Its measuring range is 250Mpa. The second picture is Charge Amplifier which can enlarge the electrical signal coming from the transducer then send it to the Capture Card installed in the computer, then through DAS view we could control the measure step and check or save the results.

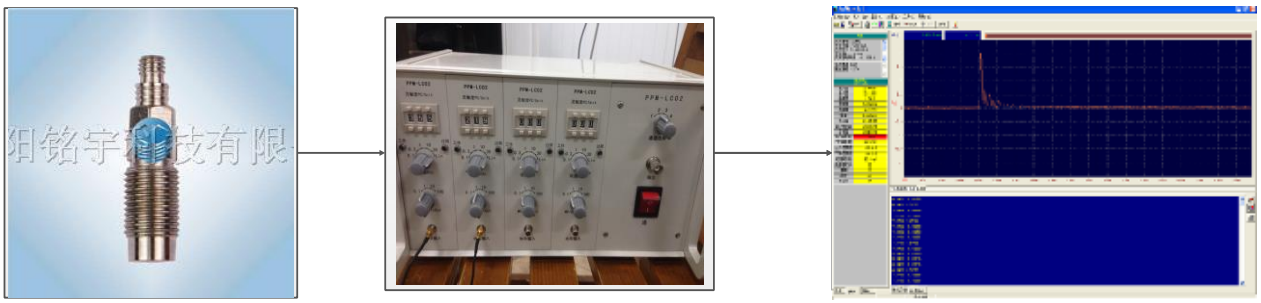

Figure B5 Pressure measuring module

B.4 Test main steps

There are three main steps in this test: ice sample preparation, choosing the sabot and test record.

- Sample preparation.

There are three things need to be taken into consideration. The first one is to choose which kind of liquid to make ice sample. The second one is design what kind of mould to product the sample. The third one is how to freeze and storage the ice sample.

Figure B6 City water, Mineral water

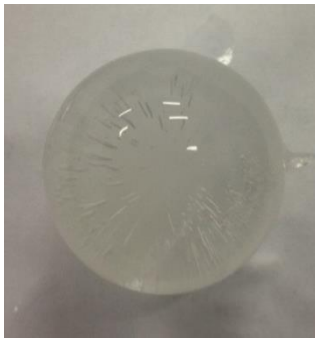

Figure B7 distilled water

Three kinds of water have been tried: Boiled City water, Mineral water and Distilled water. Figure B6 shows a sample made by boiled city water, it can be noticed that it is opaque. Figure B7 shows sample made by distilled water which is transparent that can see the bubbles in the ice clearly. Because this test needs to observe the kinematic behaviour and crack generation expansion of the ice during the impact event, so we use the distilled water to make samples.

Three kinds of moulds have been tried, they are Buber sphere mould (Figure B8), nylon block mould, aluminium mould (Figure B9). Figure B8 shows the sample produced by rubber sphere mould through which a large crack can be observed. The sample frozen through nylon block mould shows the same phenomenon. Figure B9 shows the samples produced by aluminium mould, and there are no Macroscopic cracks in it. Because through the freezing procedure the volume of the water will increase to 110%. Both Rubber and Nylon are easy to deform and cannot sustain the expansion which will make it is easy to frow cracks. Aluminium

mould is rigid, so it can sustain the expansion and the ice will grow out of the water intake hole. So we choose aluminium mould to make ice samples.

Figure B8 Rubber mould

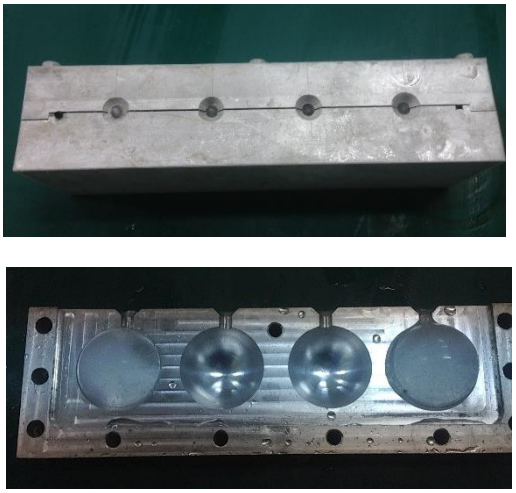

Figure B9 Aluminium mould

The volume of ice varies with changes to the temperature of the environment, so cracks are easy generated. Many combinations of freezing time and storage time have been tried. It is confirmed that when the freezing time is 6 hours with the temperature of -7°C, and the storage time is 5 hours under -7°C,the crack won't emerge easily during releasing and the acceleration.

Put the mould into -7°C for approximately 10 minutes. Use a syringe to inject distilled water to make sure there is on gas in the mould and then freeze it.

- Sabot choosing

It is very crucial to choose the material and the shape of the sabot, because of ice brittle property. Ice samples will be easily deformed due to high acceleration or the impact between the specimen and its sabot. 4 different sabots,

unfortunately, none of them are suitable for this test. Finally we choose to directly launch ice samples without sabot and the results are acceptable.

Table B1 Sabot test

Material &type of sabot	Is the ice sample broken?
Aluminum without foam pad	Broken
Nylon without foam pad	Broken
Nylon with foam pad	Some are broken but the pad would impact on the target as well
Without sabot	A few are broken

- Test record

Then set the high-speed camera and the DAS view. We need to set the high speed camera Frame rate over 10,000 frames per second.

B.5 Test results

3 series of tests were processed. Low speed, middle speed, and middle high speed.

We only keep 3 tests whose velocities are close to the average speed, and the gap is no bigger than 1.5% of the average velocity. Figure B10 is the result with an impact velocity around 66m/s.

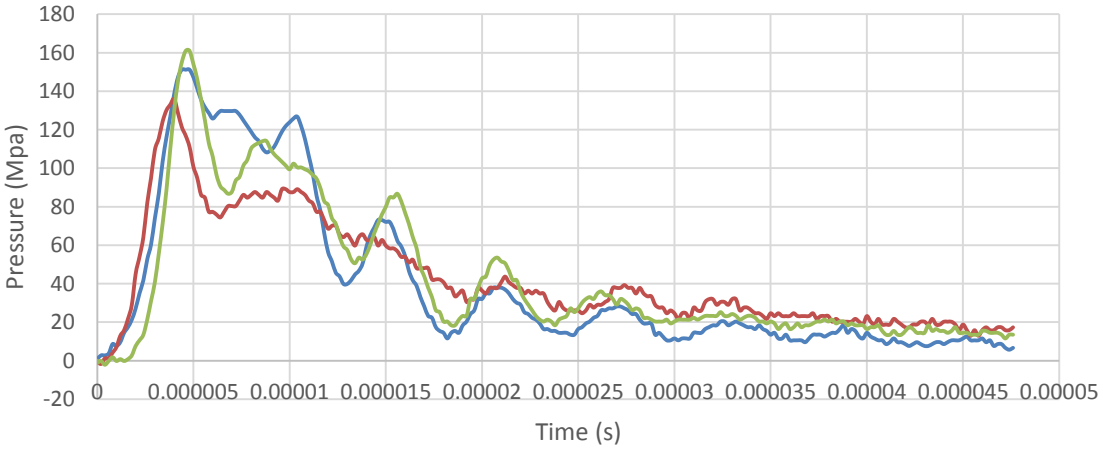

Figure B10 Test result (66m/s)

Appendix 11 shows the results from the middle speed test, and 3 test results have been chosen based on the same rule. 3 test data are chosen.

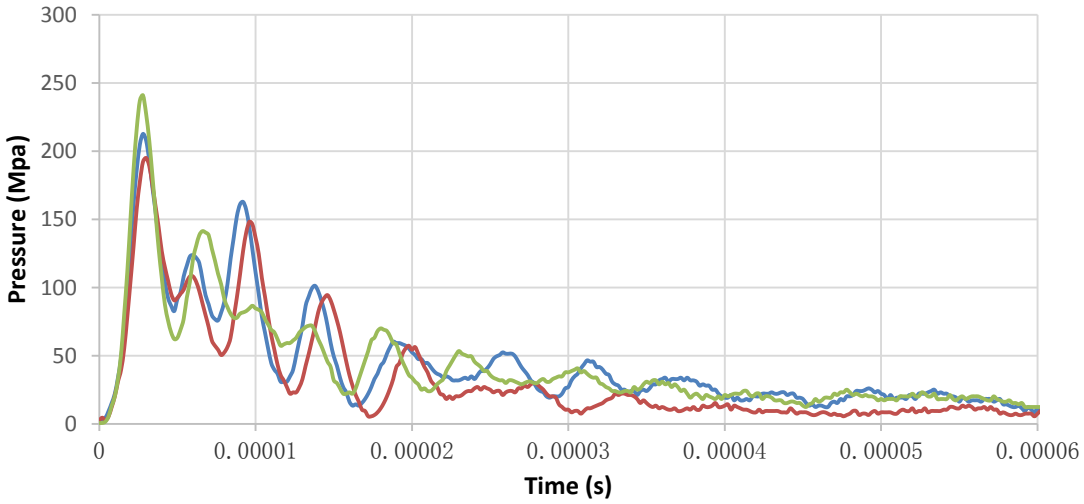

Figure B11 Test result (91m/s)

Figure B12 shows the results come from the middle high speed test, around 160m/s，but the stress of such a high velocity is highly above the measuring range of the transducer. So the results of middle high speed test currently are not acceptable.

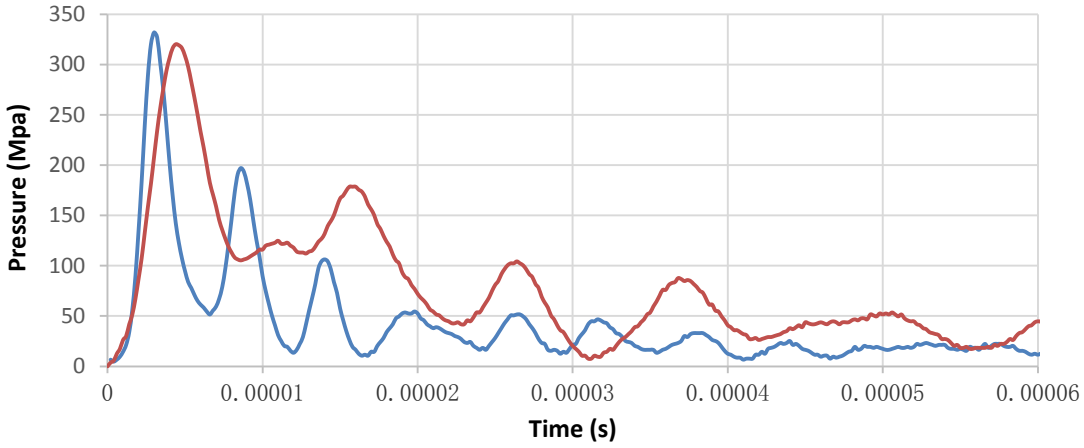

Appendix 12 Test result (165m/s)